Critical Parameters and Factors Impacting the Performance of Photovoltaic Systems

Lead Guest Editor: Daniel T. Cotfas
Guest Editors: Sergiu Spataru, Petru A. Cotfas, and Deaconu Adrian

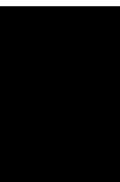# Critical Parameters and Factors Impacting the Performance of Photovoltaic Systems

Critical Parameters and Factors Impacting the Performance of Photovoltaic Systems

Lead Guest Editor: Daniel T. Cotfas
Guest Editors: Sergiu Spataru, Petru A. Cotfas, and Deaconu Adrian

Contents

Research Article

On the Reliability of Transformerless Photovoltaic DC/AC Converters Based on Mission Profile

Ignacio Villanueva [iD],[1] **Nimrod Vazquez** [iD],[1] **Joaquín Vaquero** [iD],[2] **Claudia Hernández** [iD],[1] **Héctor López** [iD],[1] **Rene Osorio** [iD],[3] **and Sergio Pinto** [iD][4]

[1]*Electronics Engineering Department, TecNM-Instituto Tecnológico de Celaya, 38010 Celaya, Mexico*
[2]*Electronics Technology Area, Rey Juan Carlos University, 28933 Mostoles, Madrid, Spain*
[3]*Computer Science and Engineering Department, University of Guadalajara, 46600 Ameca, Jalisco, Mexico*
[4]*Research Development and Innovation Department, International Maritime University of Panama and "Universidad de Panama", WCWQ+53 Panama, Panama*

Correspondence should be addressed to Nimrod Vazquez; n.vazquez@ieee.org

Photovoltaic systems are a technology for the generation of electrical energy that is constantly increasing thanks to current technological advances and that contributes to sustainable development. The main stages of photovoltaic systems are the conversion stage, using an inverter, and filtering. These systems may be considered as a mature and growing technology; however, regarding its reliability, there exists some uncertainties, and they are related to the operation, incidents, and its potential failures, due to the number of elements, the environment, and the operating nominal values. For this reason, this article presents a comparative analysis of the reliability of single-phase transformerless photovoltaic inverters used to inject active power into the grid. This evaluation is carried out under the same design specifications for all the inverters analyzed; the study is made using a mission profile considering the IEC TR 62380 standard, where the events and environmental operating conditions are defined, and numerical simulations. This work is aimed at providing suggestions to improve the quality of the photovoltaic system also considering reliability.

1. Introduction

Energy is an essential part of the technological and economic development of countries and regions worldwide. The constant increment in the demand and price of energy in industrialized countries has gradually led to the substitution of fossil fuels for the use of alternative energies. The higher use of those energies, mainly wind and solar photovoltaic, brings favorable effects on the environment, such as the reduction of greenhouse gases and other types of pollutants [1–4].

The great number of advantages that this type of energy presents is remarkable. However, the way in which energy is produced has certain technical disadvantages, such as dependent on climatic conditions, which implies a deficiency in energy production [3–5].

Nowadays, environmentally friendly energies have been developed but with some drawbacks such as high penetration, which causes certain problems within the electrical grid, such as voltage variations. The control of those systems is very complex; therefore, the useful life and reliability of photovoltaic systems are becoming important factors [5–7].

Advances in power electronics have allowed the application of transformerless inverters, used in photovoltaic systems. They have good efficiency, low volume, and lightweight. These topologies are operated to not generate a common-mode voltage in order to avoid the generation of leakage currents between the photovoltaic module and the ground. The evolution of these systems brings with it the optimization and improvement of the semiconductors that make up the system, such as higher voltages and

nominal powers, best efficiencies, higher thermal resistance, higher reliability, and lower cost [5–8].

The reliability of semiconductors and capacitors is affected by operating temperature. Therefore, the system losses could lead to a failure in the semiconductor devices, such as MOSFETs and filter capacitors. The set of operating environmental conditions of a system during its useful life is called the mission profile. It is very important to design a real field mission profile, under which the system will be operating. In this way, its reliability and service life can be guaranteed; that is, the system should be designed for an environment with conditions similar to those that would be operating normally [9, 10].

The most recent studies of reliability prediction are based on the design of the mission profile, where the phases, events, and operating environments define the mission [10, 11]. In [12], the authors calculate the converter reliability using different prototypes and semiconductors by using the IEC TR 62380 standard, taking into account an annual mission profile and the effect of extreme thermal cycles in a desert area. The authors of [13] present tools for the design of the safe operation mission profile for photovoltaic inverters connected to the grid with LCL filter, based on silicon carbide devices, including electrothermal models to predict junction temperature of the device case. In [14], it is evaluated the reliability of three transformerless inverters under an annual mission profile, taking into account the thermal load of the device, which is used for the prediction of the useful life, providing new ways for the design of photovoltaic systems.

In this paper, the reliability analysis of different single-phase transformerless photovoltaic inverters is made, including an LCL filter. In each inverter, the reliability prediction is calculated using the model of French Telecommunications standard IEC TR 62380. The study considers simulations using the PSIM software for the different transformerless LCL inverter topologies. The objective is to determine what single-phase inverter topology presents the best reliability, based on the effects of the mission profile during a period. A discussion is presented on which topology is recommended based on its longevity, and comments are provided on the factors that influence failure rates, how to improve efficiency, reliability, and useful life of the photovoltaic system.

The article is organized as follows: A background on transformerless photovoltaic inverters is presented, the IEC TR 62380 reliability standard is described, and the design and simulations are shown. Subsequently, a quantitative analysis of the reliability employing the standard is determined, the results are also analyzed, and finally, some conclusions are presented.

2. Photovoltaic Inverters and Reliability

In this section, the single-phase photovoltaic inverters, the mission profile, and the IEC TR 62380 standard are addressed to provide the basis for the employed PV converters and reliability analysis considering the mission profile.

2.1. Photovoltaic Inverters. The single-phase inverters used for active power injection may use a transformer, which allows to protect and avoid leakage currents between the photovoltaic system to the ground [15]. The advantage of connecting the inverter with a low-frequency transformer is galvanic isolation between the input and the output, but it has disadvantages such as its low efficiency and big size [5]. Another part of the system is the passive elements of the output filter. The most common configurations are L, LC, and LCL filters; the latter being the one that has the advantage of smallest size and highest efficiency.

To increase the efficiency and reduce the volume, a transformerless topology may be employed; however, a high leakage current may appear [16, 17]. There are different strategies to reduce the leakage current in transformerless photovoltaic inverters connected to the electrical grid.

One strategy is to use a modulation technique that does not generate common-mode voltage variations.

The full-bridge inverter (Figure 1) is one of the simplest inverters. Consists of four switches organized in two legs, the first formed by S_1 and S_2 and the second by S_3 and S_4. This configuration has four switching states and three different output voltage levels. Two PWM modulation schemes may be employed: bipolar and unipolar modulations [6, 15, 16, 18] and [19]. The unipolar modulation is not good to avoid common-mode voltage, and the bipolar modulation should be preferred. However, in this case, a disdvantage is the incresed size of the output filter.

The dual buck inverter (Figure 2), based on the full-bridge topology, combines two unidirectional buck converters during the positive half cycle, S_1 switching at high frequency, while S_4 is always on. During the negative half-cycle, S_2 switches at high frequency, while S_3 is always on. This produces a unipolar modulation. According to the literature, one of the advantages is the high reliability; due to the diodes connected in series to the inductor, there are no tripping problems and reverse recovery issues [4, 15], and [20].

Another technique used to reduce the leakage current is the disconnection of the photovoltaic module but keeping the unipolar modulation. In this case, switches are added on the DC or AC side of the inverter to disconnect the photovoltaic module from the grid and to create new routes to reduce the leakage current.

H5 topology (Figure 3) is based on the full-bridge topology; a switch is added on the DC side. The operation is similar to that of the full-bridge inverter, but adding switch S_5, its main function is to decouple the DC side from the AC side. Switches S_1 and S_3 commute at grid frequency, switch S_2 switches only in the negative half cycle, and switch S_4 only switches in the positive half cycle. Unipolar modulation is obtained and allows to reduce the leakage current [15, 18], and [19].

The HERIC topology (Figure 4) is derived from the full-bridge converter; however, a branch is added on the AC side in parallel to the bridge output, to isolate the PV panel from the grid. The switches S_1, S_2, S_3, and S_4 switch at high frequency; normally MOSFETs are used and S_5 and S_6 at grid frequency; regularly IGBT's are used. It integrates the
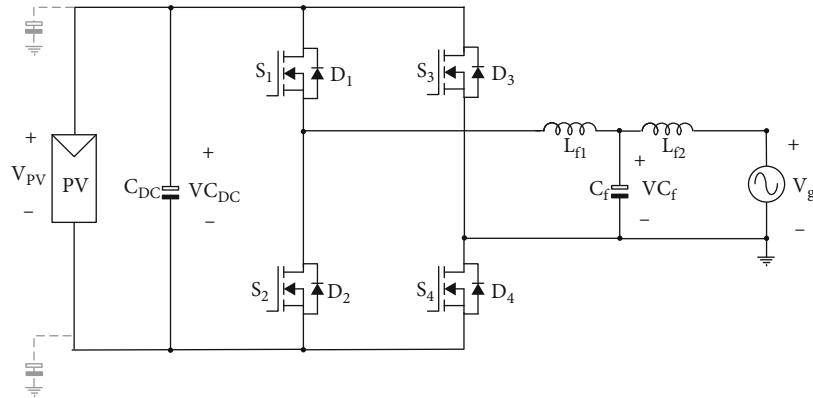
FIGURE 1: Full-bridge inverter.
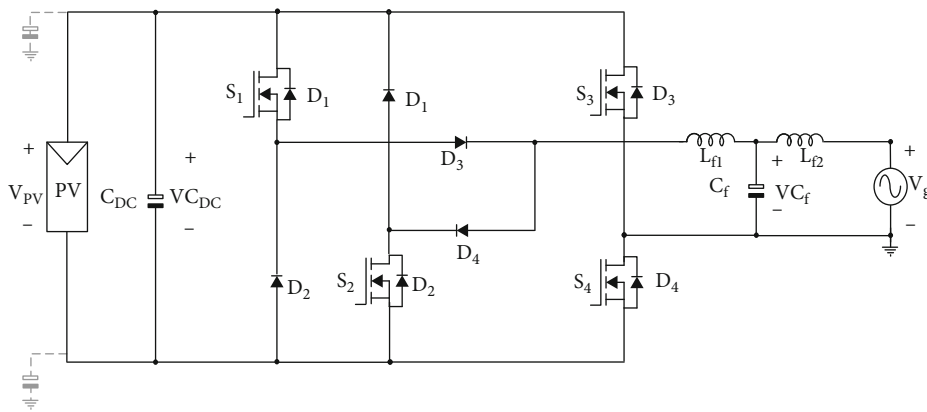
FIGURE 2: Dual buck inverter.
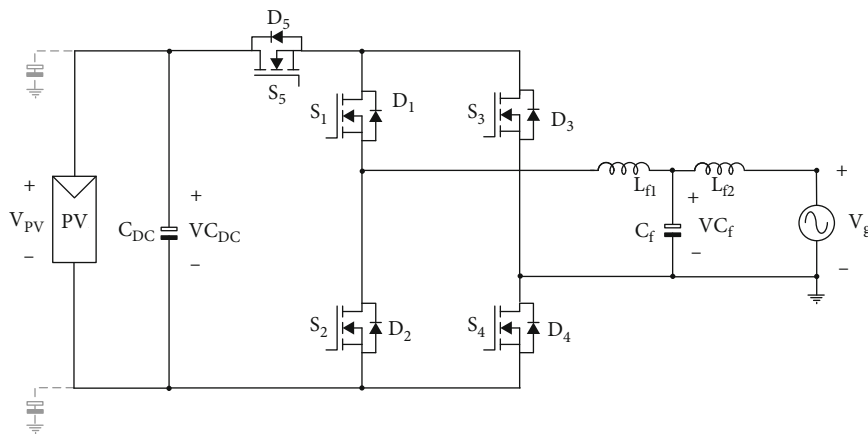
FIGURE 3: H5 inverter.

advantages of unipolar PWM modulation and reduces the leakage current of the solar panel [15, 18], and [19].

The H6 configuration (Figure 5) is based on the traditional full bridge as well, adding two switches and two diodes. For the operation, a unipolar modulation is considered, where the switches S_1, S_2, S_5, and S_6 are switched at high frequency and MOSFETS are regularly used. Switches S_3 and S_4 switch at grid frequency; IGBTs are generally used

and provide a current path with diodes D_1 and D_2. During the free conduction time, during the positive half cycle, the current flows through S_4 and the diode D_1 allowing the disconnection between the photovoltaic module and the grid [4, 15], and [18].

Another alternative to reduce the leakage current is connecting the grid neutral point to the average input voltage, which eliminates variations in high frequency. The
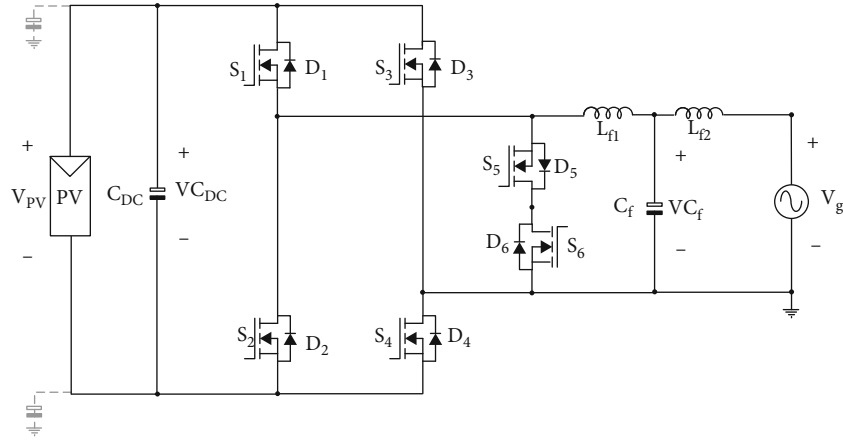
FIGURE 4: HERIC inverter.
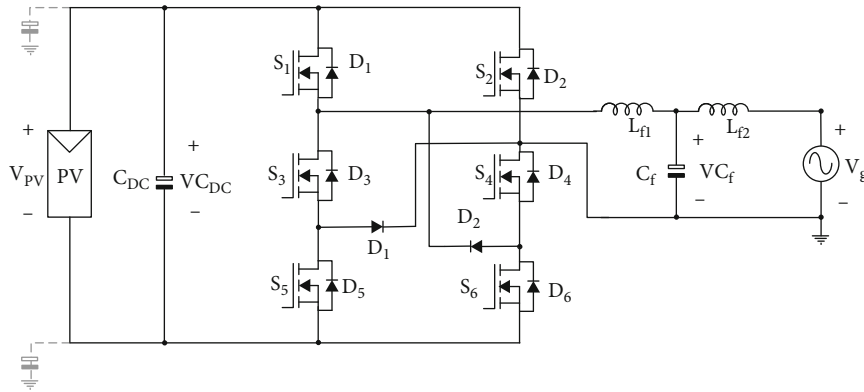
FIGURE 5: H6 inverter.
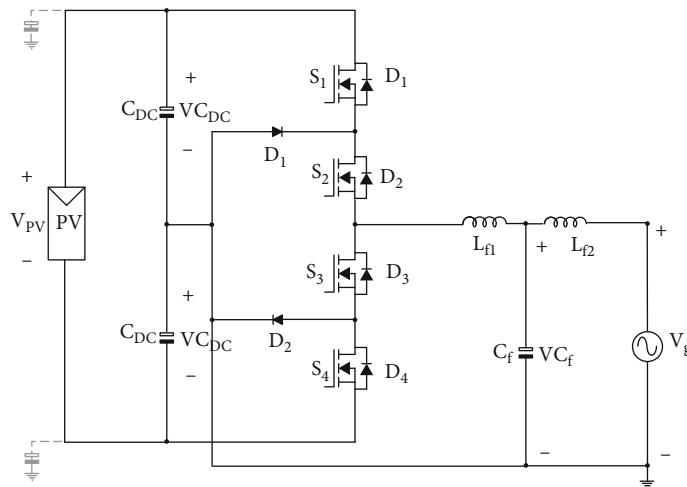
FIGURE 6: NPC inverter.

Neutral-Point Clamped (NPC) inverter fits in this category (Figure 6). It is composed of four switches; since two switches are added to the half-bridge inverter, the DC terminals are connected to two capacitors in series, which divide the panel voltage, providing a common or neutral point. The topology has two diodes connected to the neutral point.

A unipolar modulation is used, and the output voltage has three levels [4, 6, 18], and [19].

Instead of connecting the grid neutral point to the average input voltage, the connection to the negative terminal of the PV panel can be made. The virtual DC bus topology considers this strategy (Figure 7); it is derived from the full-
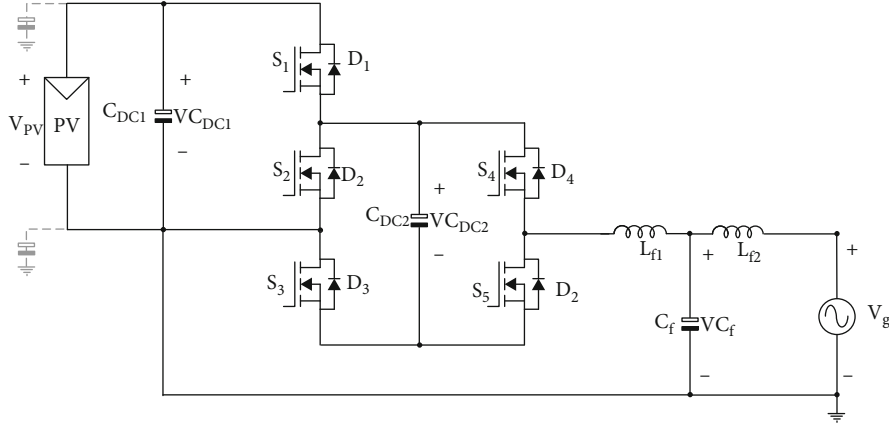
FIGURE 7: Virtual DC bus inverter.

bridge topology and consists of five switches S_1-S_5. The photovoltaic panel and capacitor C_{DC1} form a real DC bus; the virtual DC bus is generated by C_{DC2}. Capacitor C_{DC2} is charged through S_1 and S_3 to maintain a constant DC voltage. It can be controlled with a unipolar modulation [4, 15], and [21].

2.2. Mission Profile.

A mission profile refers to define or represent certain characteristics or conditions of an operating environment. The mission profile is defined to reproduce the operating conditions of an electronic component set that represents the system to evaluate. That is, the environment, events, or phases of operation are defined (solar irradiance, temperature, operating time, among others), to which the components are subject during their life cycle and allows to evaluate reliability [9, 10].

Reliability is the probability that a component will function properly during the period for which it was designed, under the specific operating conditions. The mission profile must be clearly defined, to avoid inaccuracies in the reliability calculation, which will cause errors in the final development of the system [15].

The cases that are commonly used to define a mission profile based on a one-year cycle use component normal operation, like:

(a) On/off working phases with average outside temperatures

(b) Storage mode or inactive phases

(c) Permanent working phases with fluctuations in the average outside temperature

The mission profile parameters are defined as follows. The total annual relationship of times must be defined, in the printed circuit board (PCB) which will be in permanent operation mode (energized). This is represented by τ_{on} as:

$$\tau_{on} = \sum_{i=1}^{y} \tau_i, \tag{1}$$

where τ_i is the total annual relation of times for the PCB, in permanent operation mode, with supply and at the external ambient temperature (t_{ac}) that surrounds the equipment during the ith phase of the mission profile $(t_{ac})_i$.

It is also important to define the total annual relationship of times for the PCB in storage or inactive mode of operation. This is represented by τ_{off}:

$$\tau_{off} = 1 - \tau_{on}. \tag{2}$$

Adding τ_{on} in both terms of (2) is obtained:

$$\tau_{on} + \tau_{off} = 1. \tag{3}$$

The other parameter of the mission profile that is defined is the internal temperature increase in the components of the PCB compared to (t_{ac}) during the τ_{on} phase, and it is represented by $\Delta \tau_i$:

$$\Delta \tau_i = \left[\frac{\Delta T_j}{3} + (t_{ac})_i \right] - (t_{ae})_i, \tag{4}$$

where $(t_{ac})_i$ is the average ambient temperature of the PCB, close to the components (it is considered the most critical temperature), n_i represents the annual number of thermal cycles seen by the components of the PCB in phase ith of the mission profile with a temperature variation, and $\Delta \tau_i$ is defined as the average oscillations of the variation seen by the components of the PCB in the phase of the mission profile ith [11–14, 21].

2.3. Standard IEC TR 62380 and Reliability Design.

There are different standards used for reliability prediction based on the mission profile. One of the best used is the IEC TR 62380 standard, which is a French standard (Union Technique de L'Électricité, UTEC C 80-810), which is used for the prediction of the reliability of electronic components, PCBs, and equipment.

In this standard, environmental factors are defined in the mission profile; the data contained in the standard is obtained from field data in different operating environments.

The reliability model used by the IEC TR 62380 standard is based on a failure rate model to be adjusted for each component defined as $\lambda_{\text{component}}$:

$$\lambda_{\text{component}} = \lambda_{\text{die}} + \lambda_{\text{package}}, \tag{5}$$

$$\lambda_{\text{die}} = \lambda_{\text{thermal effects}} + \lambda_{\text{EOS effects}}, \tag{6}$$

where λ_{die} is the failure rate related to the effects in operation, $\lambda_{\text{thermal effects}}$ is the failure rate related to thermal effects, $\lambda_{\text{EOS ffects}}$ is the failure rate related to the effects of electrical overstress, and λ_{package} is the failure rate related to thermo-mechanical effects.

Then, the model of the IEC TR 62380 standard is centered on the elements. In photovoltaic inverters, the main devices are the diode, the MOSFET, the capacitor, and the inductor.

The general mathematical model for the fit failure rate obtained by combining (5) and (6) is

$$\lambda_{\text{component}} = \lambda_{\text{thermal effects}} + \lambda_{\text{EOS effects}} + \lambda_{\text{package}}. \tag{7}$$

The general model (7) is used to adjust the failure rate of the components. Table 1 shows the factors and failure rates of adjustments from the general model, corresponding to the diode. The adjustment of the failure rate and factors of the MOSFET are shown in Table 2. The inductor failure rates are shown in Table 3. Finally, the failure rates of thermal and mechanical adjustments for the capacitor are shown in Table 4.

The parameters of Tables 1–4 are defined as follows:

λ_0 is the base failure rate given in the standard

λ_B is the base failure rate of the component packaging

λ_{EOS} is the failure rate related to electrical overstress in the application considered

π_U is the use factor for the diode (permanent or not); in switching conditions, it is considered permanent work

$(\pi_t)_i = i$th is the temperature factor related to the junction temperature T_j

$\tau_i = i$th is the component working time ratio to the junction temperature ith of the mission profile

$(\pi_n)_i = i$th is the influence factor related to the number of annual cycles of thermal variations observed in the packaging with amplitude $\Delta\tau_i$

$(\Delta\tau_i) = i$th is the variation of the temperature amplitude of the mission profile

π_1 is the influence factor related to the use of the component (protection interface or not)

π_S is the load factor for transistors related to the influence of the applied voltage

The π_S load factor described previously is used in the standard for power transistors (FET, MOS, and IGBT), which is given by:

$$\pi_S = \pi_{S1} + \pi_{S2}, \tag{8}$$

where $\pi_{S1} = 0.22e^{1.7S1}$ and $\pi_{S2} = 0.22e^{3S2}$.

TABLE 1: Adjustment failure rates for the diode.

λ_{diode}	
$\lambda_{\text{thermal effects}}$	$\{\pi_U.\lambda_0\}.\left\{\sum_{i=1}^{y}(\pi_t)_i.\tau_i/(\tau_{\text{on}}+\tau_{\text{off}})\right\}$
$\lambda_{\text{EOS effects}}$	$\left\{\left(2.75E^{-3}.\sum_{i=1}^{z}(\pi_n)_i.(\Delta T_i)^{0.68}\right).\lambda_B\right\}$
λ_{package}	$\{\pi_1.\lambda_B\}$

TABLE 2: Adjustment failure rates for the MOSFET.

λ_{MOSFET}	
$\lambda_{\text{thermal effects}}$	$\{\pi_S.\lambda_0\}.\left\{\sum_{i=1}^{y}(\pi_t)_i.\tau_i/(\tau_{\text{on}}+\tau_{\text{off}})\right\}$
$\lambda_{\text{EOS effects}}$	$\left\{\left(2.75E^{-3}.\sum_{i=1}^{z}(\pi_n)_i.(\Delta T_i)^{0.68}\right).\lambda_B\right\}$
λ_{package}	$\{\pi_1.\lambda_B\}$

TABLE 3: Adjustment failure rates for the inductor.

$\lambda_{\text{inductor}}$	
$\lambda_{\text{thermal effects}}$	$\lambda_0.\left\{\sum_{i=1}^{y}(\pi_t)_i.\tau_i/(\tau_{\text{on}}+\tau_{\text{off}})\right\}$
$\lambda_{\text{EOS effects}}$	$7E^{-3}.\left[\sum_{i=1}^{j}(\pi_n)_i.(\Delta T_i)^{0.68}\right]$

TABLE 4: Adjustment failure rates for the capacitor.

$\lambda_{\text{capacitor}}$	
$\lambda_{\text{thermal effects}}$	$0.1.\left\{\sum_{i=1}^{y}(\pi_t)_i.\tau_i/(\tau_{\text{on}}+\tau_{\text{off}})\right\}$
$\lambda_{\text{EOS effects}}$	$1.4E^{-3}.\left[\sum_{i=1}^{j}(\pi_n)_i.(\Delta T_i)^{0.68}\right]$

S_1 represents the quotient between the maximum applied repetitive voltage value and the specific nominal voltage in V_{DS}. S_2 is the quotient between the maximum applied repetitive voltage value and the specific nominal voltage in V_{GS}. They are determined by:

$$S_{1,2} = \frac{\text{Maximun repetitive voltage } V_{\text{DS}}, V_{\text{GS}}}{\text{Specific nominal voltage } V_{\text{DS}}, V_{\text{GS}}}. \tag{9}$$

The influence factor π_n depends on the number of annual cycles of thermal variations to which the component is subjected. There are two important relationships to define this parameter, which are shown below.

(a) If the component is subjected to $n \leq 8760$ thermal cycles/year, then $(\pi_n)_i = n_i^{0.76}$

(b) If the component is subjected to $n \geq 8760$ thermal cycles/year, then $(\pi_n)_i = 1.7\,n_i^{0.60}$

The temperature acceleration factor is given by the Arrhenius equation, which shows that the rate of change

π_t is a function of the increase in temperature. Each component depends on a specific adjustment value; Table 5 shows the models for each given component.

The reliability standard based on the mission profile is very sensitive to the temperature parameter; this can be seen in Table 5 in the Arrhenius models. Therefore, it is very convenient to define the models to determine the amplitude of the thermal variation for an on/off phase; in the following Table 6, this parameter is defined for each component of the inverter [11, 12, 22].

In the case of low current in the inductor in the on/off phase, $\Delta\tau_i$ is calculated in the same form as in the capacitor. As it has been observed, the thermal effects play a fundamental role in the reliability evaluation. It can be realized that the mission profile is based on the effect of temperature π_t during the performance of photovoltaic systems, as shown by the Arrhenius equation shown in Table 5. It is dependent on the junction temperature in each one of the components that make up the system and the effects $\Delta\tau_i$ of the rate of temperature change during the phases.

The junction temperature T_j for switches and diodes is calculated by (10):

$$T_j = T_C + \left(\theta_{jc}.p_{\text{loss}}\right), \tag{10}$$

where θ_{jc} is the junction-encapsulated thermal resistance, P_{loss} is the losses on the switch, and T_C is the temperature of the package.

The losses in the MOSFET are the sum of static and dynamic losses and are represented by [7, 12, 16, 22]:

$$P_{\text{loss(static)}} = R_{\text{DSon}}.I_{\text{rms}}^2, \tag{11}$$

$$P_{\text{loss(dynamic)}} = V_{\text{avg}}.I_{\text{avg}}.(t_{\text{on}} + t_{\text{off}}).f_{\text{SW}}, \tag{12}$$

$$P_{\text{loss}} = P_{\text{loss(static)}} + P_{\text{loss(dynamic)}}, \tag{13}$$

where P_{loss} is the total power losses, R_{DSon} is the internal resistance, I_{rms} is the effective current, I_{avg} and V_{avg} are the average values, $t_{\text{on}} + t_{\text{off}}$ represent the on and off time, and f_{sw} is the switching frequency.

The power loss of an inductor is defined by:

$$P_{\text{loss\_inductor}} = P_{\text{core}} + P_{\text{dcr}} + P_{\text{acr}}, \tag{14}$$

where P_{core} is the core loss that can be calculated or provided by the manufacturer, P_{dcr} represents the cable loss caused by the DC resistance, and P_{acr} is defined as the cable loss caused by AC resistance.

For this calculation is used [17, 23]:

$$P_{\text{core(mW)}} = K_1 f^x B^y x V_e, \tag{15}$$

where K_1 is the constant for core material, f^x is the frequency in kHz, B^y represents the maximum flux density, x is the frequency exponential function, y is an exponential function of flux density, and V_e is the effective core volume.

TABLE 5: Arrhenius model.

Component	π_t
Diode	$\pi_t = \exp\left\{4640\left[1/313 - 1/\left(T_j + 273\right)\right]\right\}$
Transistor	$\pi_t = \exp\left\{3480\left[1/373 - 1/\left(T_j + 273\right)\right]\right\}$
Inductor	$\pi_t = \exp\left\{1740\left[1/303 - 1/\left(T_j + 273\right)\right]\right\}$
Capacitor	$\pi_t = \exp\left\{2900\left[1/303 - 1/\left(T_j + 273\right)\right]\right\}$

TABLE 6: Amplitude of thermal variation in on/off phases.

Component	$\Delta\tau_i$
Diode	$\left[(\Delta T_j/3) + (t_{\text{ac}})_i\right] - (t_{\text{ae}})_i$
Transistor	$\left[(\Delta T_j/3) + (t_{\text{ac}})_i\right] - (t_{\text{ae}})_i$
Inductor	$\left[(\Delta T_R/3) + (t_{\text{ac}})_i\right] - (t_{\text{ae}})_i$
Capacitor	$(t_{\text{ac}})_i - (t_{\text{ae}})_i$

$$P_{\text{dcr(W)}} = I_{\text{rms}}^2\text{DCR}, \tag{16}$$

where I_{rms} is the effective value of the peak current applied to the inductor and DCR is the DC resistance of the inductor.

$$P_{\text{acr(W)}} = I_{\text{rms}}^2\text{ACR}, \tag{17}$$

where I_{rms} represents the effective value of the peak-to-peak ripple current applied to the inductor and ACR is the AC resistance of the inductor.

3. Power Stage and Converter Design

The photovoltaic system is comprised of a photovoltaic panel, a conversion stage, that is the inverter, and the filtering stage.

The stage responsible to inject active power into the grid is the inverter. Main transformerless inverter topologies were described in Section 2, which are full-bridge, double buck, H5, HERIC, H6, NPC, and virtual DC bus.

3.1. Power Stage Design. The inverters were designed for a power of 1 kW, and an LCL filter was used in each of the inverters, since it is intended that all the inverters are under the same operating and design conditions to determine the reliability of each one using the IEC TR 62380 standard for the mission profile.

The selection of the LCL filter was based on its advantages such as smaller size, higher efficiency, lower THD percentage, and better reliability than the L and LC filters [16].

The LCL filter design considers the following aspects. In a photovoltaic system, we have the following relationship:

$$V_g = V_{pv}m, \tag{18}$$

where V_g is the voltage of the electrical grid, V_{pv} is the voltage of the photovoltaic panel, and m is the modulation index.

The resonant frequency must be in a range of values between the network frequency and the switching frequency, satisfying:

$$10f_o \leq f_{res} \leq f_{sw}, \tag{19}$$

where f_0 is the frequency of the electrical grid, f_{res} is the resonant frequency, and f_{sw} is the switching frequency.

The LCL filter is the combination of a capacitor C_f in parallel with two coils L_{f1} and L_{f2}; the calculation of L_{f1} is obtained with:

$$L_{f1} = \frac{V_{pv}(1-m)m}{\Delta_{iLf1}f_{sw}}, \tag{20}$$

where Δ_{iLf1} is the inductor current ripple.

The inductor ratio is determined by α. The relation should be between $\alpha \, \epsilon \, [3, 7]$. The relationship of the individual inductances is

$$L_{f1} = \alpha L_{f2}. \tag{21}$$

The filter capacitor is selected according to (22), and it is a function of ω_{res} the resonant frequency (19) [4, 5, 16], [17]:

$$C_f = \frac{L_{f1} + L_{f2}}{L_{f1}L_{f2}\omega_{res}}. \tag{22}$$

The design parameters of the inverter and the LCL filter were calculated using equations (18)–(22). The results are shown in Table 7.

3.2. Reliability Design. It is important to define the concept of reliability and the average time between failures, used to evaluate the useful life of the inverters. Reliability was defined previously and is represented as $R(t)$:

$$R(t) = 1 - F(t) = \int_0^t f(t)dt, \tag{23}$$

where $f(t)$ is a function of failure density, t is the time when the component will fail, and $F(t)$ is the cumulative distribution function.

In electronic systems, the exponential distribution is used, giving that represents the useful life of electronic systems with a constant failure rate $\lambda(t)$ assuming that they have survived the initial time. The exponential distribution function is represented by:

$$f(t) = \lambda e^{-\lambda t}. \tag{24}$$

Substituting (24) in (23) and integrating, the exponential reliability function is obtained:

TABLE 7: Design parameters.

LCL filter
$P_0 = 1$ kW
$V_g = 127$ Vrms
$V_{pv} = 200$ V
$L_{f1} = 425 \, \mu$H
$L_{f2} = 141 \, \mu$H
$C_f = 6.6 \, \mu$F

$$R(t) = e^{-\lambda t}. \tag{25}$$

The average value of the useful life cycle before a failure occurs in the same equipment or component is known as the Mean Time Between Failures (MTBF) and is represented by:

$$\text{MTBF} = \int_0^\infty tf(t)dt = \int_0^\infty \lambda e^{-\lambda t} = \frac{1}{\lambda} = \frac{1}{n\lambda_i}. \tag{26}$$

It is worth mentioning that the reliability with this standard is evaluated in terms of MTBF or FIT (Failures in Time). One FIT equals a one failure in $10E^{9 \text{ hours}}$ [12, 16, 24].

A high number for the MTBF represent good reliability. Once these two concepts have been defined, a reliability analysis is made for each inverter using a serial model. It is known that a system is a grouping of interconnected components. In this way, the reliability of the system will depend on the individual reliability of the components. The serial model is used since in this model if there is a failure in any of the elements or components, the failure of the entire system would be assumed. The serial system is defined as the product of all the individual reliabilities that make up the system. The analysis of $\lambda(t)$ and the MTBF allows determining which component is the weakest. Thus, improving the reliability of this component, the complete system reliability improves.

As an example of calculation, the dual buck inverter (Figure 8) is analyzed using the serial system to determine its reliability.

The following considerations are taken into account for this analysis: the reliability of the switches is equal $R_{S1}(t) = R_{S2}(t) = R_{S3}(t) = R_{S4}(t) = R_1(t)$ and that they present a constant failure rate $\lambda_{S1} = \lambda_{S2} = \lambda_{S3} = \lambda_{S4} = \lambda_1$.

For the diodes, the reliability is considered in a similar manner since they have the same characteristics. Therefore, diodes have a reliability $R_{D1}(t) = R_{D2}(t) = R_{D3}(t) = R_{D4}(t) = R_2(t)$ and a constant failure rate $\lambda_{D1} = \lambda_{D2} = \lambda_{D3} = \lambda_{D4} = \lambda_2$.

In the case of the inductors and the filter capacitor, the reliability is as follows. For the inductor L_{f1}, there is a reliability $R_{Lf1}(t) = R_3(t)$ and a failure rate $\lambda_{Lf1} = \lambda_3$. The capacitor C_f has a reliability $R_{Cf}(t) = R_4(t)$ and a failure rate $\lambda_{Cf} = \lambda_4$. Finally, the inductor L_{f2} presents a reliability $R_{Lf2}(t) = R_5(t)$ and a failure rate $\lambda_{Lf2} = \lambda_5$.
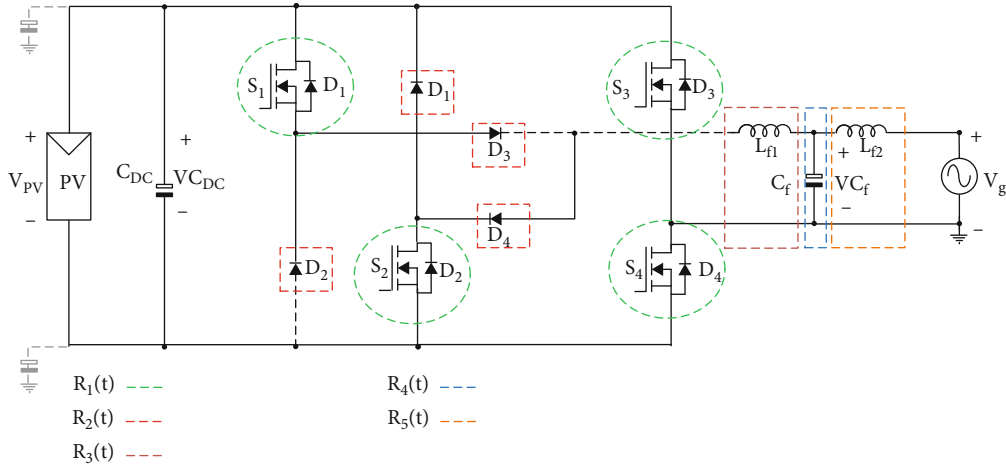
FIGURE 8: Serial analysis of the double buck inverter.
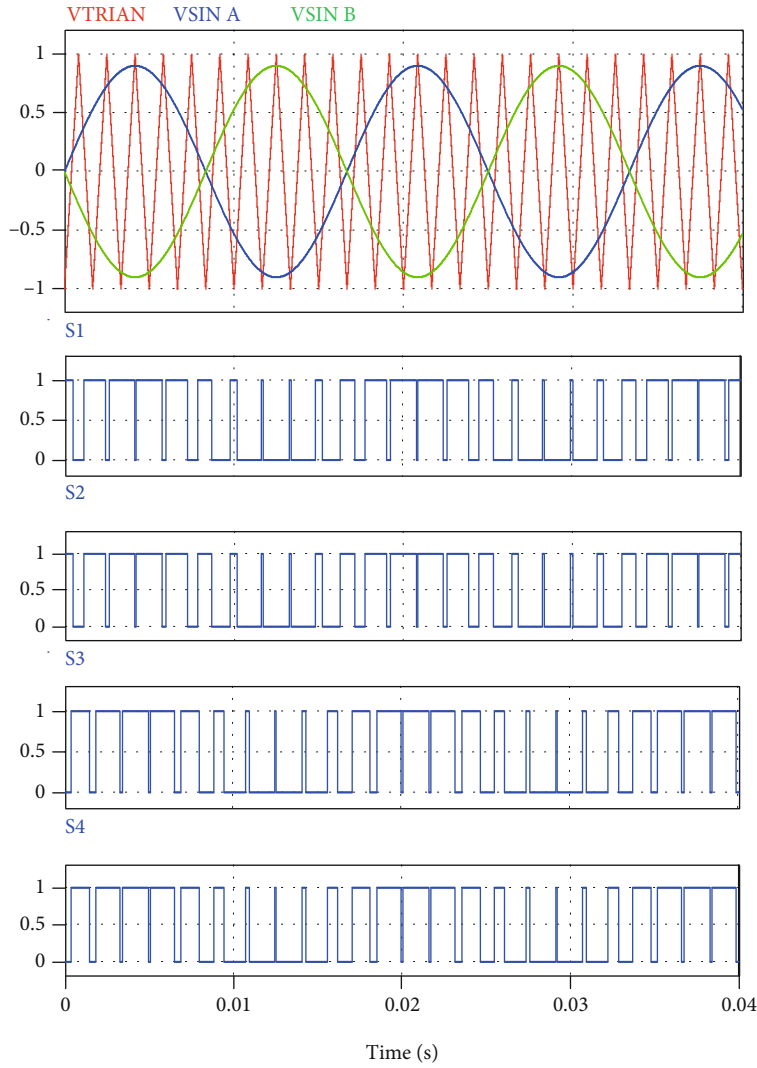
FIGURE 9: Unipolar modulation and control signals. (a–e) Modulation signals (0.5 V/div) and control signals (1 V/div).
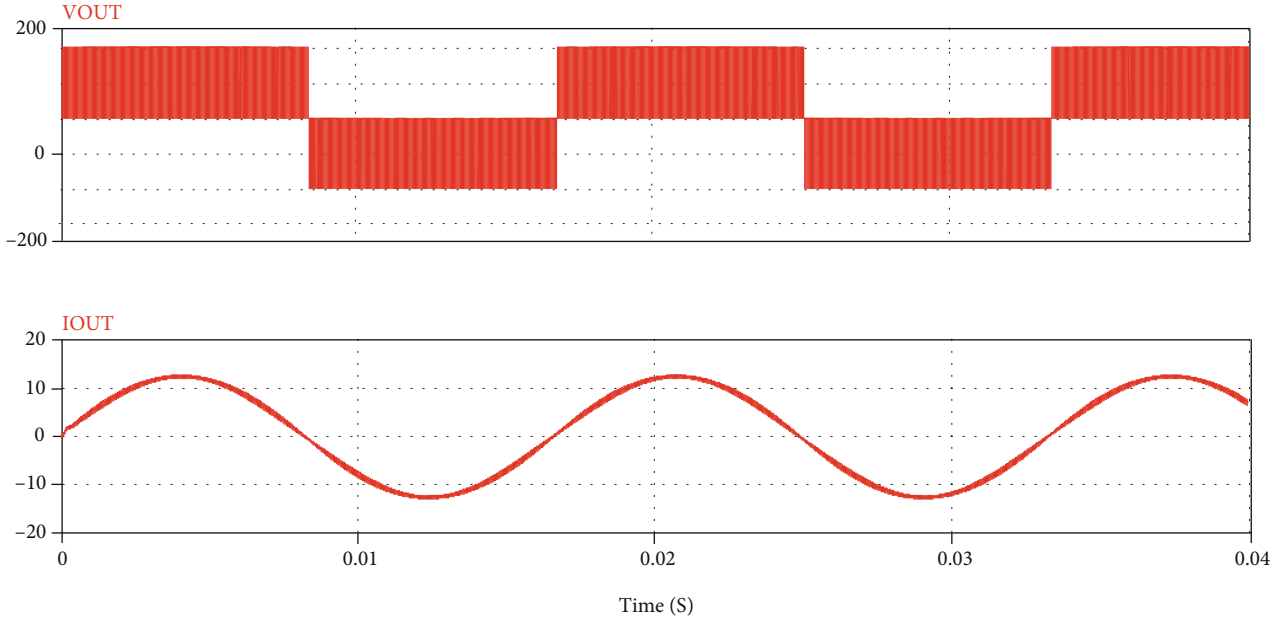
FIGURE 10: Inverter output voltage before filter. (a, b) Output voltage (100 V/div) and output current (10 A/div).
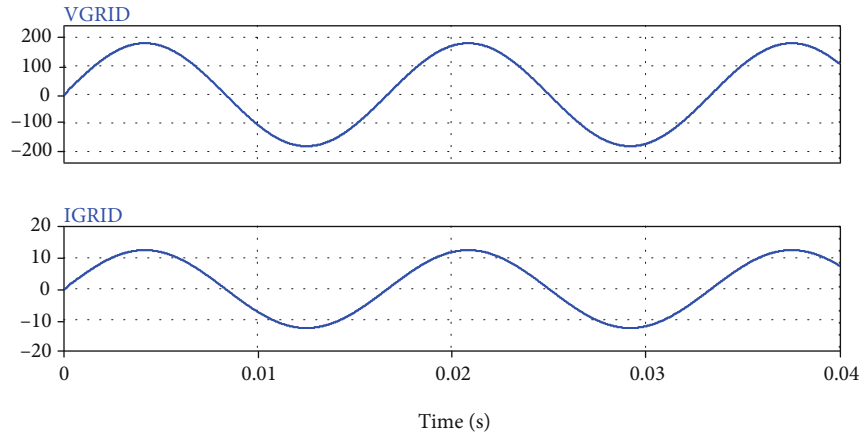
FIGURE 11: Active power injection to the grid. (a, b) Filter output voltage (100 V/div) and filter output current (10 A/div).

Solving the serial system would be as follows:

$$R_S(t) = R_1(t).R_2(t).R_3(t).R_4(t).R_5(t). \tag{27}$$

Substituting the exponential reliability function (25) in (27), the reliability of the series system is

$$R_S(t) = e^{-(4\lambda_1 + 4\lambda_2 + \lambda_3 + \lambda_4 + \lambda_5)t}. \tag{28}$$

The MTBF is calculated by substituting (28) in (26), where the following relationship is obtained:

$$\text{MTBF} = \frac{1}{4\lambda_1 + 4\lambda_2 + \lambda_3 + \lambda_4 + \lambda_5}. \tag{29}$$

The process described above is made for each of the inverters described.

4. Simulation and Reliability Results

The simulation of the inverters was carried out using the PSIM® software, as it is a very versatile software that allows fast simulation, thanks to the wide variety of device models it handles.

The simulation of each of the inverters was carried out using a unipolar open-loop modulation, since it is the type of modulation that the branches switch at high frequency, allowing the output filter to be small and having high efficiency, in addition to generating three voltage levels at the output.

In the filtering and coupling stage, the LCL filter will be used for all cases. SiC MOSFETs are used in the simulation, C3M0065090D (CREE Manufacturer). Considering the parameters according to the manufacturer's data sheet and a behavior similar to the real environment as required by

the standard, the simulations were made. For this analysis, a test ambient temperature provided by the mission profile was used, which is at which the device operates during the mission profile [16].

The simulation is performed to obtain operating parameters required for the calculation of reliability, such as voltages and currents. The failure rate adjustment models require nominal, average, or effective values for each device. In the case of the load factor, it requires maximum operating values. In the case of the temperature factor, it depends on the junction temperature of the device; therefore, average and effective values are used.

4.1. Simulation Results. The simulation results in PSIM® are shown in Figures 9–11. The control signals obtained are consistent for a unipolar modulation; for illustrating purposes in Figure 9, a switching frequency lower than the used was graphed to make it visible. Unipolar modulation signals can be observed from top to bottom on a 0.5 V/div scale and the control signals S_1, S_2, S_3, and S_4 on a 0.5 V/div scale.

In Figure 10, it can be seen from top to bottom the output voltage of the inverter before the output filter on a scale of 100 V/div and the current of 8.3 A at a scale of 10 A/div.

In Figure 11, it is observed from top to bottom the output voltage of the inverter after the filter, where a power of 1 kW would be injected into the grid. A voltage of 180 V is observed on a scale of 100 V/div and a current of 8.3 A at a scale of 10 A/div.

In Table 8, an inverter comparative analysis of the semiconductor elements is shown, as well as their efficiency, which is a parameter on which reliability depends. The efficiency of the inverters was obtained based on the simulation with a unipolar modulation for each case.

Another important parameter by which reliability is also measured is THD percentage. These parameters are directly related since they are attributes that allow evaluating the quality of the system. THD directly affects inverter reliability; it is related to the quality and safety of the system. The term quality refers mainly to the quality of the signal wave and safety; it is related to the system complying with the THD limits allowed by regulations. Table 9 shows the THD percentage of the analyzed inverters, as well as the switches that switch at high or low frequency.

Tables 8 and 9 show that comparing single-phase inverters, the one with the best characteristics in both efficiency and THD is the full-bridge inverter, with an efficiency of 99.05% and a THD of 0.08200899%, followed by the virtual DC bus with 99.00% efficiency and a THD of 0.01021878%, and double buck with 98.93% efficiency and THD of 0.08270188%.

4.2. Reliability Calculation Results. The numerical reliability calculation is performed using the IEC TR 62380 standard. Table 10 shows the base factors taken from the standard for each of the components that make up the inverters. The λ_B corresponds to the TO-220 package. The λ_{EOS} factor corresponds to the type of telecommunication mission profile.

Table 11 shows the mission profile, which complies with the total annual relationship of times given in equation (3).

TABLE 8: Comparison of number of elements and inverter efficiency.

Topology	Switches	Diodes	Capacitors	Efficiency
Full bridge	4	X	X	99.05%
Double buck	4	4	X	98.93%
H5	5	X	X	98.67%
HERIC	6	X	X	98.53%
H6	6	2	X	98.55%
NPC	4	2	X	98.86%
Virtual DC bus	5	X	1	99.00%

X indicates that it is not applied for the system.

TABLE 9: Inverter THD comparison.

Topology	High frequency	Low frequency	%THD
Full bridge	S_1, S_2, S_3, S_4	X	0.08200899
Double buck	S_1, S_2, S_3, S_4	X	0.08270188
H5	S_2, S_4, S_5	S_1, S_3	0.22131262
HERIC	S_1, S_2, S_3, S_2	S_5, S_6	0.22176104
H6	S_1, S_2, S_5, S_6	S_3, S_4	0.22176183
NPC	S_1, S_4	S_2, S_3	0.17539819
Virtual DC bus	S_1, S_2, S_3, S_4, S_5	X	0.01021878

X indicates that it is not applied for the system.

TABLE 10: Adjustment factors for power components.

Component	λ_0	λ_B	λ_{EOS}	π_U	π_1
Diode	0.7 FIT	5.7	40	1	1
Transistor	2 FIT	5.7	40		1
Inductor	0.6 FIT				

There is only one annual working phase to consider for a permanent working.

The mission profile of Table 11 is given for a permanent working; inverters operate with conditions, and values for "ground; stationary; non weather protected"(ground; fixed for Mil-HDBK-217F) can be calculated for various climates.

The mission profile is related to the failure rate adjustment equations shown in Tables 1–4. The time parameters and operating cycles shown in Table 11 are applied to the adjustment equations. The temperature factor is determined by the temperature of Table 11, and the junction temperature is obtained with values from simulation, using the Arrhenius model.

Table 12 shows the results of the reliability calculations for each of the single-phase inverters analyzed in this study. It can be observed that the full-bridge inverter and virtual DC bus present better reliability compared to the other inverters, with a lower failure rate and a higher MTBF.

The full-bridge being the best of these, with a 193.415FIT failure rate and an MTBF of 0.005171FIT, followed by the virtual DC bus with a 240.671FIT failure rate and

TABLE 11: Mission profile.

Application type	Environment type	Equipment type	$(t_{ae})i$ °C	$(t_{ac})_i$ °C	τ_1	τ_{on}	T_{off}	n_1 cycles/year	ΔT_1 °C/cycle
Telecom	Ground fixed (GF)	Transmitting and access	11	31	0.5	0.25	0.25	365	8

TABLE 12: Total reliability of inverters.

Topology	$\lambda_{System(FIT)}$	MTBF (FIT)
Full bridge	193.415	0.005171
Double buck	377.555	0.002649
H5	332.691	0.003006
HERIC	379.937	0.002632
H6	379.997	0.002632
NPC	285.485	0.003503
Virtual DC bus	240.671	0.004155
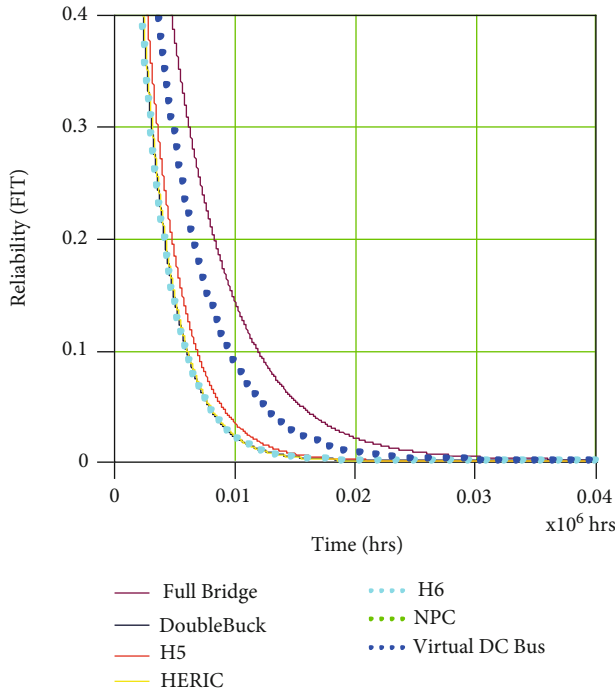
FIGURE 12: Comparative graph of the reliability of single-phase inverters.

FIGURE 13: Representation of the probability of failure of the full-bridge inverter.

0.004155FIT MTBF. The virtual DC bus inverter and the HERIC present a very similar failure rate and MTBF, only differentiated by the contribution of some element's failure rate in the NPC inverter. The inverters with the worst reliability are the HERIC with a failure rate of 379.937FIT and a 0.002632FIT MTBF and the H6 with a 379.997FIT failure rate and a 0.002632FIT MTBF.

In Figure 12, a comparative graph of the reliability of the different single-phase inverters analyzed is observed, represented in FIT. Analyzing the best case of the full-bridge inverter, it has an MTBF of 0.005171FIT, equivalent to an annual failure probability of 0.16% and reliability of

98.40%. Now the worst case, the H6 inverter has an MTBF of 0.002632FIT, equivalent to an annual failure probability of 0.33% and reliability of 96.70%. The number of years also indicates that the inverter that would present a probability of failure in the first instance is the H6. It can be seen that the curve of the complete bridge has a longer lifetime compared to the other inverters. The full-bridge turned out to be the most reliable inverter; it is convenient to represent the reliability cumulative distribution function (24). The cumulative distribution function can be interpreted as the probability of failure presented by the system in FIT. In Figure 13, a relationship between the reliability function and the failure probability function of the full-bridge inverter is observed, through an equilibrium point at the intersection of the curves.

It is important to highlight, although the full-bridge inverter has better reliability and efficiency, its use is not recommended; since it presents a leakage current between the PV and ground, and it is higher than that allowed by the European standard VDE 0126-1-1 [25], which should not be higher than 300 mA.

Table 13 shows the percentage of contribution of each component to the total failure rate of the system, concerning the number of components in Table 8. It is observed that the failure rate depends directly on the number of components that make up the system. Therefore, the reliability is directly related to the number of elements that the system has. In

TABLE 13: Percentage of contribution to the failure rate of the photovoltaic system.

| Topology | Inverter failure rate | | | | LCL filter failure rate | |
	MOSFET	Switches Parasitic diode	Diodes	Capacitors	Inductors	Capacitors
Full bridge	97.73%	X	X	X	2.21%	0.06%
Double buck	50.06%	X	48.77%	X	1.13%	0.04%
H5	71.00%	27.67%	X	X	1.30%	0.03%
HERIC	74.61%	24.23%	X	X	1.13%	0.03%
H6	74.61%	X	24.22%	X	1.13%	0.04%
NPC	66.21%	X	32.25%	X	1.51%	0.03%
Virtual DC bus	98.14%	X	X	0.04%	1.78%	0.04%

X indicates that it is not applied for the system.

addition, it is visible that in each one of the inverters that were analyzed, which are the components that have the most contribution to the failure rate of the system, that is, the components that may have the most failures and that may have a shorter lifetime. To reduce the power losses and increase reliability, the C3M0065090D SiC MOSFET (CREE Manufacturer) is used. Since the turn-on resistance is too low, a synchronous rectification occurs when the current becomes negative in the device; therefore, the free-wheeling diode does not conduct during this time, as traditionally occurs in the inverters. Since the MOSFET's voltage drop is smaller than the diode forward voltage, the MOSFET conducts for positive and negative currents, Certainly, there are some topologies where diodes conduct and synchronous rectification does not occur.

In general, in inverters, the highest percentage of failure contribution is made by the switches, followed by the diodes, then the inductors, and with the lowest percentage the capacitors. The characteristics of an MKP capacitor were used; it has advantages such as thermal and electrical stability, reliability, and a long useful life.

It is also observed that the switching frequency is a parameter that greatly affects the reliability. If the switching frequency is reduced, the reduction of losses is considerable. When determining reliability, the parameter that is related to the standard, through the Arrhenius model, is the junction temperature and thermal resistance of the component encapsulation. Therefore, the failure rate depends on the bonding temperature and the temperature in the casing; this is on the mission temperature profile. Reducing the switching frequency reduces the component failure rate by 0.10%. Then, it is obtained a $\lambda_{system} = 193.214$ FIT and an increment of the MTBF to 0.005176FIT.

Other simulations were carried out to verify the impact of the device on the reliability; a 3rd Generation SiC MOSFET (C3M0025065D) was used since the internal resistance is smaller, as mentioned previously. Then, better results were obtained; the losses were reduced, and there is a positive, but small, effect on reliability.

Following the analysis that has been made is recommended to the designer to increase the MTBF of the systems, since it is the parameter that measures the useful life of the system. This may be achieved by using component heat dissipation and cooling systems to reduce thermal stress and at the same time reduce the component failure rate as well as using devices made of better materials such as silicon carbide, which have lower (better) thermal resistance.

Also, from the analysis, the converter with fewer components will be the best option for reliability but not forgetting the leakage current of the PV system. Then, of all the inverters studied, the best alternative is the virtual DC bus inverter with SiC devices. This is because it offers a low THD, high efficiency, best reliability, and useful life while satisfying the leakage currents for PV system standards. The following alternative is the NPC inverter. Certainly, the final selection of the inverter is left to the designer, since the difference is relatively small between them.

5. Conclusion

This article presents the prediction of the reliability of different single-phase inverters using an LCL filter in the filtering stage. For the calculation and approximation of the prediction of the reliability, the standard IEC TR 62380 is used.

In this study, they were compared the full-bridge, double buck, H5, HERIC, H6, NPC, and virtual DC bus converters. The full-bridge inverter presents better reliability and better useful life. In addition, it features a higher THD percentage, at better efficiency. The virtual DC bus and NPC inverters have the following best realiability, there is a small difference in reliability and efficiency. The use of a virtual DC bus inverter with SiC devices is recommended since the full-bridge presents higher leakage current than allowed by the standards.

The study shows that the devices present a failure rate percentage in the following order: switches, diodes, inductors, and to a lesser extent, capacitors. It was observed that the switching frequency affects the reliability of the component to a lesser extent.

The parameter that directly affects reliability is the number of elements that make up the system. The reliability and average useful life of the systems can be increased, using cooling systems to reduce thermal stress, which is the parameter that directly relates to the failure rate and therefore the reliability of the system. It is also recommended to use silicon carbide devices, which are components with smaller internal resistance and thermal resistance that allows to have few losses, high efficiency, and reliability.

Data Availability

All the data used is in the paper.

Conflicts of Interest

The authors declare that there is no conflict of interest regarding the publication of this paper.

References

[1] N. L. Panwar, S. C. Kaushik, and S. Kothari, "Role of renewable energy sources in environmental protection: a review," *Renewable and Sustainable Energy Reviews*, vol. 15, no. 3, pp. 1513–1524, 2011.

[2] M. D. Leonard, E. E. Michaelides, and D. N. Michaelides, "Energy storage needs for the substitution of fossil fuel power plants with renewables," *Renewable Energy*, vol. 145, pp. 951–962, 2020.

[3] M. A. Basit, S. Dilshad, R. Badar, and S. M. Sami ur Rehman, "Limitations, challenges, and solution approaches in grid-connected renewable energy systems," *International Journal of Energy Research*, vol. 44, no. 6, pp. 4132–4162, 2020.

[4] W. Li, Y. Gu, H. Luo, W. Cui, X. He, and C. Xia, "Topology review and derivation methodology of single-phase transformerless photovoltaic inverters for leakage current suppression," *IEEE Transactions on Industrial Electronics*, vol. 62, no. 7, pp. 4537–4551, 2015.

[5] L. S. Xavier, A. F. Cupertino, H. A. Pereira, and V. F. Mendes, "Partial harmonic current compensation for multifunctional photovoltaic inverters," *IEEE Transactions on Power Electronics*, vol. 34, no. 12, pp. 11868–11879, 2019.

[6] K. Zeb, W. Uddin, M. A. Khan et al., "A comprehensive review on inverter topologies and control strategies for grid connected photovoltaic system," *Renewable and Sustainable Energy Reviews*, vol. 94, pp. 1120–1141, 2018.

[7] M. H. Ahmed, M. Wang, M. A. S. Hassan, and I. Ullah, "Power loss model and efficiency analysis of three-phase inverter based on SiC MOSFETs for PV applications," *IEEE Access*, vol. 7, pp. 75768–75781, 2019.

[8] M. C. Cavalcanti, A. M. Farias, K. C. Oliveira, F. A. S. Neves, and J. L. Afonso, "Eliminating leakage currents in neutral point clamped inverters for photovoltaic systems," *IEEE Transactions on Industrial Electronics*, vol. 59, no. 1, pp. 435–443, 2012.

[9] Y. Yang, K. Ma, H. Wang, and F. Blaabjerg, "Mission profile translation to capacitor stresses in grid-connected photovoltaic systems," in *2014 IEEE Energy Conversion Congress and Exposition (ECCE)*, pp. 5479–5486, Pittsburgh, PA, USA, 2014.

[10] A. Sangwongwanich, Y. Yang, D. Sera, and F. Blaabjerg, "Mission profile-oriented control for reliability and lifetime of photovoltaic inverters," *IEEE Transactions on Industry Applications*, vol. 56, no. 1, pp. 601–610, 2020.

[11] "A Universal Model for Reliability Prediction of Electronics Components, PCBs and Equipment," in *Reliability Data Handbook*, Union Technique de L'Electricite, UTE C 80-810, 1st ed edition, 2000.

[12] S. E. De León-Aldaco, H. Calleja, F. Chan, and H. R. Jiménez-Grajales, "Effect of the mission profile on the reliability of a power converter aimed at photovoltaic applications-a case study," *IEEE Transactions on Power Electronics*, vol. 28, no. 6, pp. 2998–3007, 2013.

[13] N. Sintamarean, F. Blaabjerg, H. Wang, and Y. Yang, "Real field mission profile oriented design of a SiC-based PV-inverter application," *IEEE Transactions on Industry Applications*, vol. 50, no. 6, pp. 4082–4089, 2014.

[14] Y. Yang, H. Wang, and F. Blaabjerg, "Reliability assessment of transformerless PV inverters considering mission profiles," *International Journal of Photoenergy*, vol. 2015, Article ID 968269, 10 pages, 2015.

[15] M. Shayestegan, M. Shakeri, H. Abunima et al., "An overview on prospects of new generation single-phase transformerless inverters for grid-connected photovoltaic (PV) systems," *Renewable and Sustainable Energy Reviews*, vol. 82, pp. 515–530, 2018.

[16] I. Villanueva, N. Vázquez, J. Vaquero, C. Hernández, H. López, and R. Osorio, "L vs. LCL filter for photovoltaic grid-connected inverter: a reliability study," *International Journal of Photoenergy*, vol. 2020, Article ID 7872916, 10 pages, 2020.

[17] P. Channegowda and V. John, "Filter optimization for grid interactive voltage source inverters," *IEEE Transactions on Industrial Electronics*, vol. 57, no. 12, pp. 4106–4114, 2010.

[18] N. Vázquez, M. Rosas, C. Hernández, E. Vázquez, and F. J. Perez-Pinal, "A new common-mode transformerless photovoltaic inverter," *IEEE Transactions on Industrial Electronics*, vol. 62, no. 10, pp. 6381–6391, 2015.

[19] S. V. Araujo, P. Zacharias, and R. Mallwitz, "Highly efficient single-phase transformerless inverters for grid-connected photovoltaic systems," *IEEE Transactions on Industrial Electronics*, vol. 57, no. 9, pp. 3118–3128, 2010.

[20] L. Zhou and F. Gao, "Dual buck inverter with series connected diodes and single inductor," in *2016 IEEE Applied Power Electronics Conference and Exposition (APEC)*, pp. 2259–2263, Beach, CA, USA, 2016.

[21] "Reliability Methodology for Electronic Systems," in *FIDES guide 2009 Edition A*, FIDES group, 2010.

[22] "Universal Model for Reliability Prediction of Electronic Components, PCBs and Equipment," in *Reliability Data Handbook*, Technical Report IEC TR 62380, 1st ed edition, 2004.

[23] Y. Zhou, W. Huang, F. Hong, and C. Wang, "Modelling analysis and power loss of coupled-inductor single-stage boost inverter based grid-connected photovoltaic power system," *IET Power Electronics*, vol. 9, no. 8, pp. 1664–1674, 2016.

[24] F. Richardeau and T. T. L. Pham, "Reliability calculation of multilevel converters: theory and applications," *IEEE Transactions on Industrial Electronics*, vol. 60, no. 10, pp. 4225–4233, 2013.

[25] X. Guo, N. Wang, J. Zhang, B. Wang, and M. K. Nguyen, "A novel transformerless current source inverter for leakage current reduction," *IEEE Access*, vol. 7, pp. 50681–50690, 2019.

Review Article

Analytical versus Metaheuristic Methods to Extract the Photovoltaic Cells and Panel Parameters

Daniel T. Cotfas [ID], **Petru A. Cotfas** [ID], **Mihai P. Oproiu** [ID], **and Paul A. Ostafe**

Department of Electronics and Computers, Faculty of Electrical Engineering and Computer Science, Transilvania University of Brasov, 500036, Romania

Correspondence should be addressed to Daniel T. Cotfas; dtcotfas@unitbv.ro

The parameters of the photovoltaic cells and panels are very important to forecast the power generated. There are a lot of methods to extract the parameters using analytical, metaheuristic, and hybrid algorithms. The comparison between the widely used analytical method and some of the best metaheuristic algorithms from the algorithm families is made for datasets from the specialized literature, using the following statistical tests: absolute error, root mean square error, and the coefficient of determination. The equivalent circuit and mathematical model considered is the single diode model. The result comparison shows that the metaheuristic algorithms have the best performance in almost all cases, and only for the genetic algorithm, there are poorer results for one chosen photovoltaic cell. The parameters of the photovoltaic cells and panels and also the current-voltage characteristic for real outdoor weather conditions are forecasted using the parameters calculated with the best method: one for analytical—the five-parameter analytical method—and one for the metaheuristic algorithms—hybrid successive discretization algorithm. Additionally, the genetic algorithm is used. The forecast current-voltage characteristic is compared with the one measured in real sunlight conditions, and the best results are obtained in the case of a hybrid successive discretization algorithm. The maximum power forecast using the calculated parameters with the five-parameter method is the best, and the error in comparison with the measured ones is 0.48%.

1. Introduction

Nowadays, the power forecasting for the photovoltaic panels and systems plays a very important role for the investors to increase the investments having a realistic scenario. One of the steps to achieve this goal is to accurately and quickly determine the parameters of the photovoltaic cells and panels.

The extraction of the photovoltaic cell parameters is a widely studied issue [1, 2], but it remains current due to its importance and the new possibilities created by the metaheuristic algorithms and artificial intelligence [3].

The parameter extraction is possible if there is a dataset which consists of voltage-current pairs (V, I) for the photovoltaic panel, or if the current-voltage characteristic $(I\text{-}V)$ is measured. The parameters and dataset can be obtained using the photovoltaic panel datasheet given by the producer [4].

The most commonly used mathematical model to characterize the photovoltaic cells and panels is the single diode model (SD) [1], followed by the double diode model (DD) [5] and rarely three diode model (TD) [6]. The number of the parameters which have to be extracted varies, being five for SD, seven for DD, and nine for TD. There are a lot of methods to extract these parameters, their complexity growing with the increasing number of parameters.

The methods used to extract the parameters of the photovoltaic cells or panels can be classified into analytical, metaheuristic, and hybrid methods [7]. Each of these methods has both advantages and disadvantages.

The contributions and novelty of this paper are as follows:

(i) The main analytical methods and metaheuristic algorithms grouped on families are briefly presented

(ii) The performance of the methods is analyzed in function of the accuracy with which the parameters are extracted analyzing the absolute error, the root mean square error, and the coefficient of determination

(iii) Choosing the best analytical method considering the following: simplicity of application, the execution time, and the accuracy

(iv) Choosing the metaheuristic algorithm with the smallest root mean square error (RMSE) for different photovoltaic cells and panels from all algorithms considered

(v) Comparing for the first time the analytical method (modified five parameters) and metaheuristic algorithm (hybrid successive discretization algorithm) to forecast the I-V characteristic and the maximum power generated by the commercial monocrystalline photovoltaic panel, giving the manufacturers a tool to choose the best option to characterize the PV for their applications. Additionally, the genetic algorithm is considered in the comparison

The rest of the paper is organized as follows: the equivalent circuits and diode models, statistical tests used for comparison, and the mathematical formulas for calculating the photovoltaic cells and panel parameters at different temperatures and irradiances in the function of their values at the standard test conditions (STC-irradiance $1000\,\mathrm{W/m^2}$, temperature $25°\mathrm{C}$, and air mass 1.5) are described in Section 2. A brief presentation of the used methods is made in Section 3. The results and discussions are presented in Section 4, and the last section is dedicated to conclusions and future works.

2. Methods

2.1. Photovoltaic Cells and Panel Diode Models.
The mathematical model which describes the dependence between the current and the voltage generated by the photovoltaic cells and panels depends on the mechanisms which are taken into account and consequently on the equivalent circuits, Figure 1. The simplest model is the ideal one. The most commonly used model is single diode, Figure 1(a), due to its simplicity but also because it manages to describe the behaviour of most types of photovoltaic cells and panels very well. Equation (1) is the mathematical relation for one diode model:

$$I = I_{\mathrm{ph}} - I_{\mathrm{o}}\left(e^{(V+IR_{\mathrm{s}})/nV_{\mathrm{T}}} - 1\right) - \frac{V + IR_{\mathrm{s}}}{R_{\mathrm{sh}}}, \qquad (1)$$

where I_{ph} is the photogenerated current, I_{o} is the reverse saturation current, R_{s} is the series resistance, R_{sh} is the shunt resistance, n is the ideality factor of diode, and V_{T} is the thermal voltage, $V_{\mathrm{T}} = kT/q$. k is the Boltzmann constant, T is the temperature, and q is the elementary electrical charge.

The double diode model is described by

$$I = I_{\mathrm{ph}} - I_{\mathrm{o1}}\left(e^{(V+IR_{\mathrm{s}})/n_1 V_{\mathrm{T}}} - 1\right) - I_{\mathrm{o2}}\left(e^{(V+IR_{\mathrm{s}})/n_2 V_{\mathrm{T}}} - 1\right) - \frac{V + IR_{\mathrm{s}}}{R_{\mathrm{sh}}}, \qquad (2)$$

where index 1 relates to the diffusion mechanism and 2 the generation-recombination mechanism. The accuracy to determine the parameters of the photovoltaic cell increases especially at low solar radiation when the two diode model is used [8].

The mathematical model for the photovoltaic panel is described by

$$I = N_{\mathrm{p}}I_{\mathrm{ph}} - N_{\mathrm{p}}I_{\mathrm{o}}\left(e^{(N_{\mathrm{p}}V + N_{\mathrm{s}}IR_{\mathrm{s}})/nN_{\mathrm{p}}N_{\mathrm{s}}V_{\mathrm{T}}} - 1\right) - \frac{N_{\mathrm{p}}V + N_{\mathrm{s}}IR_{\mathrm{s}}}{N_{\mathrm{s}}R_{\mathrm{sh}}}, \qquad (3)$$

where N_{s} represents the number of the photovoltaic cells connected in series and N_{p} represents the number of the photovoltaic cells connected in parallel.

2.2. Statistical Test.
The comparison between analytical and metaheuristic algorithms is achieved using different statistical error tests, such as absolute error (AE) Equation (4), the root mean square error Equation (5), and the coefficient of determination R^2 Equation (6).

$$\mathrm{AE} = \sum_{i=1}^{n} |I_{ic} - I_{im}|, \qquad (4)$$

$$\mathrm{RMSE} = \sqrt{\frac{\sum_{i=1}^{n}(I_{ic} - I_{im})^2}{n}}, \qquad (5)$$

$$R^2 = 1 - \frac{\sum_{i=1}^{n}(I_{ic} - I_{im})^2}{\sum_{i=1}^{n}(I_{im} - \bar{I}_{im})^2}, \qquad (6)$$

where I_{ic} and I_{im} represent the calculated and the measured current, respectively, and n is the total number of measurements.

2.3. Irradiance and Temperature Dependence of the PV Parameters.
The irradiance and temperature influence more or less the parameters of the photovoltaic cells and panels. The power generated is also dependent on these two factors. So, the relation for photogenerated current, function of the irradiance, and temperature is the following [9]:

$$I_{\mathrm{ph}} = \frac{G}{G_{\mathrm{ref}}}\left[I_{\mathrm{ph,ref}} + \alpha_{\mathrm{sc}}(T, T_{\mathrm{ref}})\right], \qquad (7)$$

where G is irradiance, T represent the temperature, and α_{sc} is the temperature coefficient of the current. The index ref
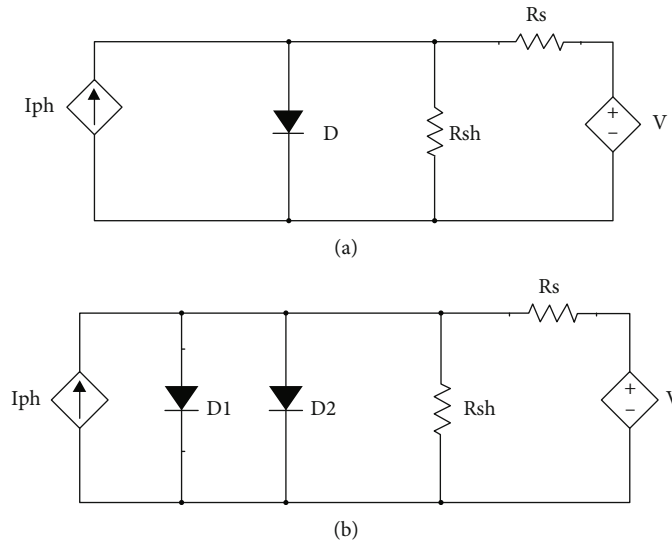
Figure 1: The equivalent circuit of photovoltaic cell: (a) one diode model; (b) two diode model.

is for the parameters at STC. The reverse saturation current can be calculated with Equation (8) [9, 10]:

$$I_o = I_{o,ref} \left(\frac{T}{T_{ref}} \right)^3 e^{q/Kn\left(\left(E_{g,ref}/T_{ref} \right) - \left(E_g/T_r \right) \right)}, \qquad (8)$$

where E_g is the energy bandgap. This value depends slightly on temperature [11, 12]:

$$E_g = E_{g,ref} \lfloor 1 - 0.0002677(T - T_{ref}) \rfloor. \qquad (9)$$

The ideality factor of diode depends slightly on the irradiance [13]. The temperature dependence can be written as Equation (10) [9]:

$$n = n_{ref} \frac{T}{T_{ref}}. \qquad (10)$$

The behaviour of the shunt resistance is inversely proportional to that of irradiance, the irradiance increasing as the shunt resistance decreases:

$$R_{sh} = R_{sh,ref} \frac{G_{ref}}{G}. \qquad (11)$$

The dependence of the series resistance on temperature and irradiance is described by Equation (12). It decreases linearly with the increase in temperature and increases with the increase of irradiance; β is constant and is considered equal to 0.217 [11, 14].

$$R_{sh} = R_{sh,ref} \frac{T}{T_{ref}} \left(1 - \beta \ln \frac{G}{G_{ref}} \right). \qquad (12)$$

3. Analytical and Metaheuristic Methods

Pillai and Rajasekar classified the methods to extract the parameters of the photovoltaic cells and panels in analytical, metaheuristic, and hybrid (consisting of those mentioned before) methods [8]. The analytical methods are based on formulas obtained using approximation and/or particular points on the *I-V* characteristic and some parts of the *I-V* characteristics. Multiobjective optimization problems were tough issues, but the development and use of metaheuristic algorithms in the last years led to solutions with a very good accuracy [15]. These metaheuristic algorithms were quickly adapted and used to solve the multimodal problem of the current-voltage dependence of the photovoltaic devices.

3.1. Analytical Methods. These methods were used to calculate the parameters of the photovoltaic cells since the 60s [13]. A lot of methods have been developed, especially for the SD model, but in the last years, they were developed for DD and even TD models. They can calculate one, more than one, or all parameters of the photovoltaic cells and panels. The several analytical methods are presented in Table 1.

The complexity of usage and the accuracy of the method to extract the parameters of the photovoltaic cells or panels are two key indicators. Three-level ratings are used for each of them: low, medium, and high. For the complexity of usage, they mean as follows: low: simple formulas are used; medium: complex formulas, fitting and iterative procedure are necessary; high: the analytical method needs dedicated computational software [29]. For the accuracy, the level rating is the function of the statistical test [29, 30]. The rating for each method is shown in Table 1. Their results can be used by the manufacturers to choose the optimum method to characterize the photovoltaic cells.

The analytical five-parameter method, 5P, is the most widely used of the analytical ones to extract the parameters of the photovoltaic cells. The first step is to calculate the

TABLE 1: The analytical methods.

Methods	Parameters	Models	Remarks	Complexity of usage	Accuracy	Ref.
Analytical five-parameter method	$I_{ph}, I_o, n, R_s, R_{sh}$	SD	Using part of I-V characteristic to determine the R_s and R_{sh}	Medium	High	[16]
Tivanov	$I_{ph}, I_o, n, R_s, R_{sh}$	SD	Using part of I-V characteristic to determine the R_s and R_{sh} and $I_{ph} \sim I_{sc}$	Medium	Medium	[17]
Ortiz-Conde	$I_{ph}, I_o, n, R_s, R_{sh}$	SD	Using the CC function to calculate the equation coefficients C_{V1}, C_{I1}, C_{V2} and C_{I2}	Low	Medium	[18]
Garrido-Alzar	$I_{ph}, I_{od}, I_{or}, n_r, R_s, R_{sh}$	DD	n_r is considered 1, and four points (V, I) are using	Medium	Low	[19]
Generalized area	n, R_s, R_{sh}	SD	Using $I_{ph} \sim I_{sc}$, and the subgraphic area for three I-V characteristics	High	Low	[20]
Area	R_s	SD	Using subgraphic area for I-V characteristic and $n = 1$	Low	Low	[21]
Kaminski	$I_{od}, I_{or}, n_r, R_s, R_{sh}$	DD	The parameters are determined in dark conditions	Low	Low	[22]
R_s model	$I_{od}, I_{or}, n_r, R_s,$	SD	R_{sh} is considered ∞	Medium	Low	[23]
L function	R_s, R_{sh}	SD	Using Lambert W function	High	Medium	[24]
Explicit method for the five parameters	$I_{ph}, I_o, n, R_s, R_{sh}$	SD	Using two points for I_{sc} zone and V_{oc} zone to calculate the slopes	Medium	Medium	[9]
Cotfas	R_s and s	SD	Using I-V characteristic measured and the ideal one	Medium	Medium	[1]
Modified five parameters	$I_{ph}, I_o, n, R_s, R_{sh}$	SD	Using two empirically equations to calculate R_s and R_{sh}	Low	High	[25]
Elkholy	$I_{ph}, I_o, n, R_s, R_{sh}$	SD	Using a method based on the nonlinear least-squares algorithm; the parameters are calculated at different environmental conditions	Medium	Medium	[7]
Ndegwa	$I_{ph}, I_o, n, R_s, R_{sh}$	SD	n and I_o are calculated firstly using I_{sc}, I_m, V_m, V_{oc}, and $R_s = 0, R_{sh} \approx \infty$; R_s and R_{sh} are then evaluated for different values of n_s in the neighborhood of n_o $(1 \le n \le n_o)$	Medium	Medium	[26]
TRDLA	$I_{ph}, I_o, n, R_s, R_{sh}$	SD	n is calculated firstly using the data provided by the manufacturer's datasheet; the other four parameters are calculated using the trust-region-dogleg algorithm	Medium	Medium	[27]
Brano	$I_{ph}, I_o, n, R_s, R_{sh}$	SD	Using five equations derived from Equation (1)	Medium	Medium	[28]

slope around the open-circuit voltage to calculate R_{so}, Equation (12), and the short circuit current to calculate R_{sho}, Equation (13). The slope calculation requires having many points on the I-V characteristic in the two regions. In case this is not possible and to reduce the complexity of the method, R_{so} and R_{sho} can be calculated using Equations (15) and (16), empirically obtained in modified five parameters 5Pm [25].

$$R_{so} = -\left(\frac{dV}{dI}\right)_{V=V_{oc}}, \qquad (13)$$

$$R_{sh} = R_{sho} = -\left(\frac{dV}{dI}\right)_{I=I_{sc}}, \qquad (14)$$

$$R_{so} = 0.002102 + 0.318070 R_{sm}, R_{sm} = \frac{V_{oc} - V_m}{I_m}, \qquad (15)$$

$$R_{sho} = -0.051914 + 2.505219 R_{sm}, R_{shm} = \frac{V_m}{I_{sc} - I_m}, \qquad (16)$$

where I_m and V_m represent the maximum power point coordinates.

$$n = \frac{V_m + R_{so}I_m - V_{oc}}{V_t(\ln(I_{sc} - (V_m/R_{sh}) - I_m) - \ln(I_{sc} - (V_{oc}/R_{sh})) + I_m/(I_{sc} - (V_{oc}/R_{sh})))},$$
$$I_o = \left(I_{sc} - \frac{V_{oc}}{R_{sh}}\right) \exp\left(-\frac{V_{oc}}{nV_T}\right),$$
$$R_s = R_{so} - \frac{nV_t}{I_o} \exp\left(-\frac{V_{oc}}{nV_T}\right),$$
$$I_{ph} = I_{sc}\left(1 + \frac{R_s}{R_{sh}}\right) + I_o\left(\exp\left(\frac{I_{sc}R_s}{nV_T}\right) - 1\right).$$
$$(17)$$

3.2. Metaheuristic Methods.

The metaheuristic algorithms have been used to extract the parameters of the PV since the 2000s, when Jervase et al. used the genetic algorithms

Table 2: The metaheuristic algorithms.

Family algorithms	Type	Models	PV	Range set	Computational time/iterations	Reference
Genetic	Simple	SD	50 W panel	Partially	-/50	[31]
Genetic	Simple	SD	57 mm RTC France solar cell	Yes	-/-	[32]
GA-R	Simple	SD	57 mm RTC France solar cell, mSi commercial photovoltaic cell	Partially	56 s/5000	[33]
Genetic GA-LS	Hybrid	SD	57 mm RTC France solar cell	Yes	-/-	[34]
Differential evolution DE	Simple	SD, DD	57 mm RTC France solar cell, PWP201 photovoltaic panel	Yes	12 s and 16 s/ 10000 and 20000	[35]
Differential evolution R_{cr}-IJADE	Simple	SD, DD	57 mm RTC France solar cell	Yes	33 s and 58 s/ 10000 and 20000	[36]
Penalty differential evolution P-DE	Simple	DD	pSi-S75 and S115 mSi-SM55 and SQ150PC tin film-ST36 and ST40	Partially	42 s/500	[37]
Differential evolution with an individual-dependent mechanism IDE	Simple	SD, DD	57 mm RTC France solar cell, PWP201 photovoltaic panel	Yes	-/10000 and 20000	[35]
Linear population success-history-based adaptive DE L-SHADE	Simple	SD, DD	57 mm RTC France solar cell, PWP201 photovoltaic panel	Yes	35.4 and 62.66 s/10000 and 20000	[35]
Differential evolution DEIM	Hybrid	SD, DD	KC120 PV module	Yes	32 s/10000 and 20000	[38]
Particle swarm optimization CPSO	Simple	SD	57 mm RTC France solar cell	Yes	-/4500	[39]
Particle swarm optimization VCPSO	Simple	DD	—	No	-/-	[40]
Particle swarm optimization NM-MPSO	Hybrid	SD, DD	57 mm RTC France solar cell	Yes	-/350000	[41]
Fractional chaotic ensemble particle swarm optimizer FC-EPSO	Hybrid	SD, DD	57 mm RTC France solar cell	Yes	11.5 s and 12 s/ 200	[42]
Chaotic heterogeneous comprehensive learning PSO C-HCLPSO	Hybrid	SD, DD	57 mm RTC France solar cell	Yes	204 s and 225 s/ 2000	[43]
Hybrid successive discretization algorithm HSDA	Hybrid	SD, DD	57 mm RTC France solar cell, 3 × 3 cm monocrystalline silicon photovoltaic cell, PWP201 photovoltaic panel, STP6-120/36, STM6-40/36, etc.	Yes	28 s and 46 s/4	[44]
Discretization SDA	Simple	SD	57 mm RTC France solar cell, 3 × 3 cm monocrystalline silicon photovoltaic cell, PWP201 photovoltaic panel	Yes	142 s and 266 s/ 4	[3]
Discretization PSDA	Simple	SD, DD	57 mm RTC France solar cell, PWP201 photovoltaic panel, Kyocera KC200GT photovoltaic panel	Yes	28 s and 46 s/4	[45]
Artificial bee colony optimization ABCO	Simple	SD, DD	57 mm RTC France solar cell, PWP201 photovoltaic panel, STM6-40/36	Yes	-/10000	[46]
Artificial bee colony optimization ABC-NMS	Hybrid	SD	57 mm RTC France solar cell, PWP201 photovoltaic panel	Yes	-/5000	[47]
Shuffled complex evolution ISCE	Simple	SD, DD	57 mm RTC France solar cell, PWP201 photovoltaic panel	Yes	-/5000 and 10000	[48]
Shuffled complex evolution-opposition-based learning ESCE-OBL	Hybrid	SD, DD	57 mm RTC France solar cell, PWP201 photovoltaic panel	—	-/5000 and 10000	[49]
Simulated annealing SA	Simple	SD, DD	57 mm R.T.C France solar cell, Photowatt-PWP201	—	-/-	[64]

TABLE 2: Continued.

Family algorithms	Type	Models	PV	Range set	Computational time/iterations	Reference
Simulated annealing LM-SA	Hybrid	SD	57 mm RTC France solar cell	—	-/2050	[50]
Flower pollination FPA	Simple	SD, DD	57 mm RTC France solar cell, Photowatt-PWP201	Yes	-/25000	[51]
Flower pollination BPFPA	Hybrid	SD, DD	57 mm RTC France solar cell	Partially	-/20000	[52]
Harmony search HS	Simple	SD, DD	57 mm RTC France solar cell	—	-/5000	[53]
Innovative global harmony search IGHS	Simple	SD, DD	57 mm RTC France solar cell	—	-/5000	[53]
Pattern search PS	Simple	SD, DD	57 mm RTC France solar cell, PWP201 photovoltaic panel	—	-/-	[54]
JAYA algorithm IJAYA	Simple	SD, DD	57 mm RTC France solar cell, PWP201 photovoltaic panel	Yes	-/50000	[55]
Performance-guided JAYA algorithm PGJAYA	Simple	SD, DD	57 mm R.T.C France solar cell, Photowatt-PWP201 KC200GT, SM55, thin-film Shell ST40	Yes	-/50000	[56]
Comprehensive learning JAYA algorithm CJAYA	Simple	SD, DD	57 mm RTC France solar cell, PWP201 photovoltaic panel	—	-/20000 and 48000	[57]
Teaching–learning-based optimization TLBO	Simple	SD, DD	57 mm RTC France solar cell, PWP201 photovoltaic panel	—	-/20000	[58]
Improved TLBO ITLBO	Simple	SD, DD	57 mm R.T.C France solar cell, PWP201 photovoltaic panel, STP6-120/36, STM6-40/36	—	5.95 s (30) and 6.60s (30)/ 50000	[59]
Whale optimization algorithm WOA	Simple	SD, DD	KC200GT	Yes	-/45000	[60]
Improved version of WOA IWOA	Simple	SD, DD	57 mm RTC France solar cell, PWP201 photovoltaic panel, JAM6-60-295W-4BB, CS6U-320P	Yes	-/100000	[61]
Multiple learning backtracking search algorithm MLBSA	Simple	SD, DD	57 mm RTC France solar cell, PWP201 photovoltaic panel	Yes	39 and 44 s/ 50000	[62]
BSA-Lévy flight (LFBSA)	Simple	SD, DD	57 mm RTC France solar cell, PWP201 photovoltaic panel	Yes	-/50000	[63]

and the DD model to extract the seven parameters of the photovoltaic cell [31]. By using metaheuristic algorithms, all parameters of the photovoltaic cells and panels can be calculated. There are a lot of metaheuristic algorithms applied to extract the parameters of the photovoltaic cells and panels. The lower and upper values for the photovoltaic cells or panel parameters are necessary to be considered for the limitation of the global optimum search. Table 2 presents some of them, classified on family and on whether they are simple or hybrid [8]. The families of the algorithms presented are genetic algorithms (GA) [31–34], differential evolution (DE) [35–38], particle swarm optimization (PSO) [39–43], discretization [3, 44, 45], artificial bee colony (ABC) [46, 47], shuffled complex evolution [48, 49], simulated annealing (SA) [50, 51], flower pollination algorithm (FPA) [52, 53], harmony search (HS) [54], JAYA algorithm [55–57], teaching–learning-based optimization algorithm [58, 59], whale optimization algorithm [60, 61], and backtracking search algorithm [62, 63]. Additionally, the diode model is shown, computational time and the iteration number when these are given.

One of the new and the best algorithms, HSDA [44], is used against the modified analytical method to forecast the I-V characteristic and maximum power generated. The HSDA algorithm is an improved version of the SDA algorithm [3]. It is a hybrid one. The first algorithm used is one of the existent algorithms and gives a solution for SDA. A vicinity is considered around it, and the parameters can be extracted with very good accuracy using SDA for this vicinity. The flow chart of the HSDA algorithm is presented in Figure 2.

4. Results and Discussion

4.1. Analytical vs. Metaheuristic. The representative analytical method—modified five parameters—which has low difficulty to use and high accuracy, for SD model, it is compared with the best metaheuristic algorithms for each family, for several photovoltaic cells and panels when the results for the parameters are available. The parameter values for the SD model given in the references are used to calculate the statistical tests AE, RMSE, and R^2 used for comparison.
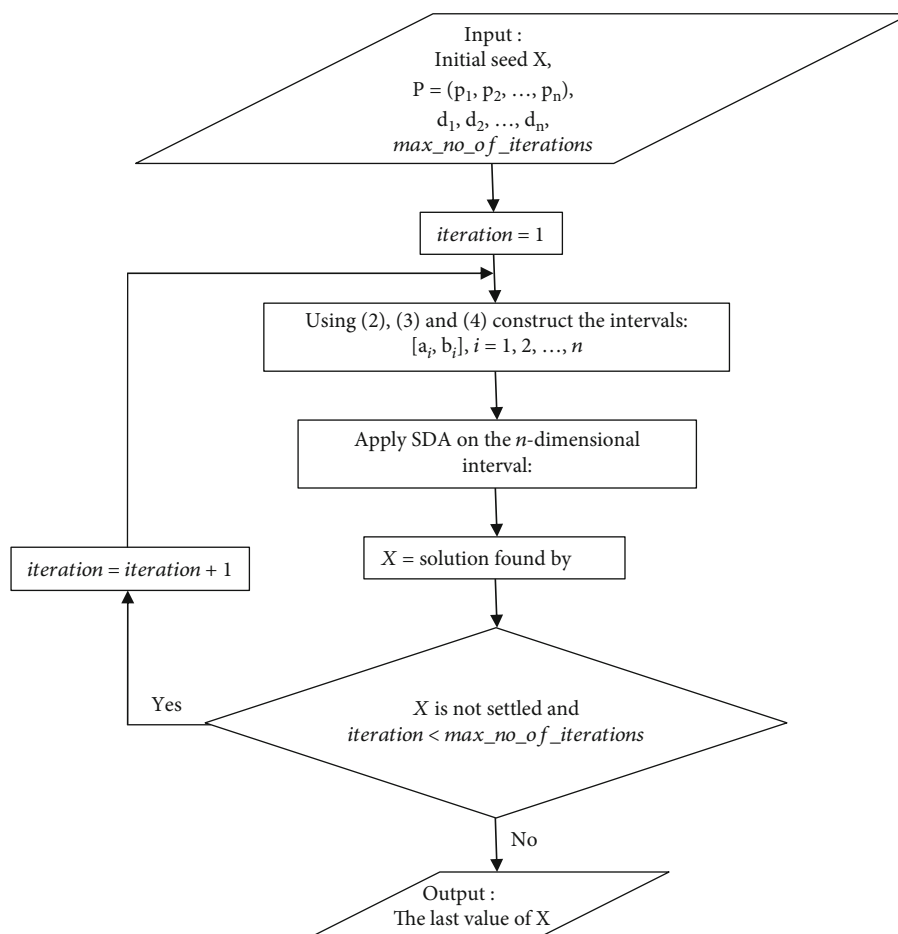
Figure 2: HSDA algorithm flow chart [44].

Table 3: The parameters and statistical tests for RTC cell.

Algorithm	I_{ph} (A)	I_o (μA)	n	$R_s(\Omega)$	$R_{sh}(\Omega)$	RMSE	AE	R^2
HSDA [44]	0.7607758	0.323016532	1.48118232	0.03637708	53.714520885	$9.8602E-04$	0.0215277	0.9999893
R_{cr}-IJADE [36]	0.76077553	0.3230208	1.4811836	0.03637709	53.718525	$9.86021E-4$	0.0215271	0.9999893
C-HCLPSO [43]	0.76079	0.31062	1.4771	0.036548	52.885	$1.1201E-03$	0.0209115	0.999986
ABC–NMS [47]	0.760776	0.323021	1.481184	0.036377	53.718521	$9.86023E-04$	0,021533	0.9999893
ESCE-OBL [49]	0.76078	0.32302	1.48118	0.03638	53.7185	$9.8602E-04$	0.0215269	0.9999893
LM-SA [50]	0.76078	0.31849	1.47976	0.03643	53.32644	$9.8646E-04$	0.0215104	0.9999892
FPA [51]	0.76079	0.31062	1.47707	0.03655	52.8771	$1.214E-03$	0.0216788	0.9999837
IGHS [53]	0.76077	0.34351	1.48740	0.03613	53.2845	$1.033E-03$	0.0212025	0.9999882
CLJAYA [57]	0.76078	0.3230208	1.481184	0.0363771	53.718521	$9.8603E-04$	0.0215415	0.9999892
ITLBO [59]	0.7608	0.3230	1.4812	0.0364	53.7185	$9.9161E-04$	0.021809	0.9999891
IWOA [61]	0.7608	0.3232	1.4812	0.0364	53.7317	$9.9486E-04$	0.021131	0.9999891
MLBSA [62]	0.7608	0.32302	1.4812	0.0364	53.7185	$9.8969E-04$	0.0217216	0.9999892
5Pm [3]	0.7612	0.1966	1.43	0.042	95.28	$8.674E-03$	0.159698	0.999086
GA [33]	0.7619	0.8087	1.5751	0.0299	42.3729	0.01908	0.277673	0.995997
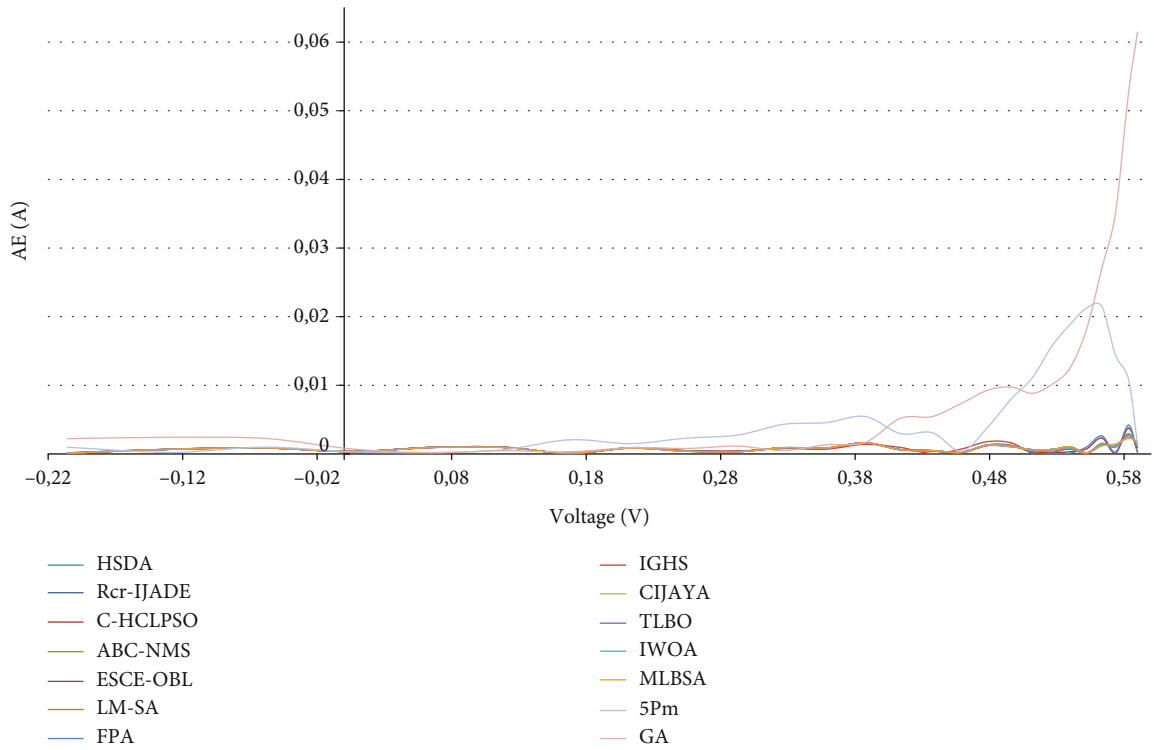
(a)
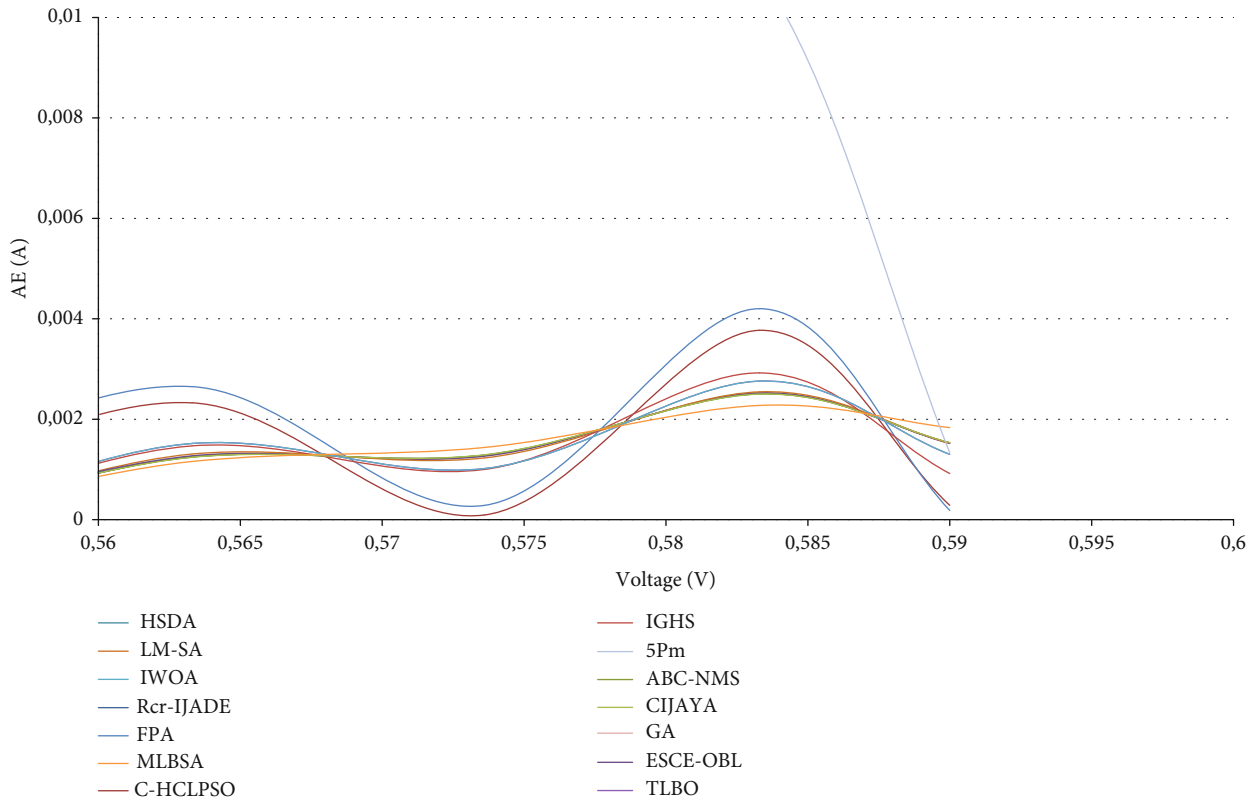
(b)

Figure 3: (a) The absolute current error (AE) for RTC France solar cell; (b) AE in open-circuit voltage region.

TABLE 4: The parameters and statistical tests for mSi commercial photovoltaic cell.

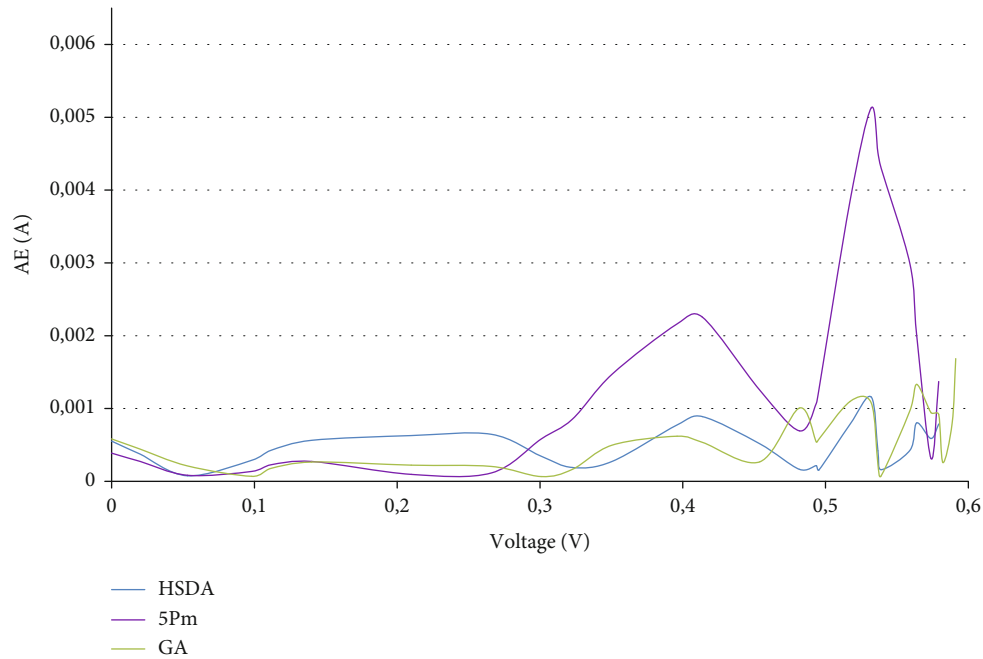| Algorithm	I_{ph} (A)	I_o (μA)	n	$R_s(\Omega)$	$R_{sh}(\Omega)$	RMSE	AE	R^2
HSDA [44]	0.42575316	0.516241613	1.67933406	0.09132898	99.075980176	$5.63098E-04$	0.0142648	0.9999853
5Pm [3]	0.4255	0.30645567	1.618311	0.10352224	145.222	$2.25639E-03$	0.047492	0.99976
GA [33]	0.4256882	0.8383311	1.73926	0.0859435	123.3659	$6.9741E-04$	0.0163354	0.99997

FIGURE 4: The absolute current error for mSi commercial photovoltaic cell.

TABLE 5: The parameters and statistical tests for PWP201 photovoltaic panel.

Algorithm	I_{ph} (A)	I_o (μA)	n	$R_s(\Omega)$	$R_{sh}(\Omega)$	RMSE	AE	R^2
HSDA [44]	1.0305143	0.348226304	48.642835	1.201271	981.201271	$2.42507E-03$	0.0489237	0.99997
R_{cr}-IJADE [36]	1.0305143	3.4822629	48.642835	1.201271	981.98216	$2.42507E-03$	0.0489237	0.99997
ABC–NMS [47]	1.03051	3.48226	48.643	1.20127	981.982	$2.42518E-03$	0.0489454	0.99997
FPA [51]	1.032091	3.047538	48.13128	1.217583	811.3721	$2.57361E-03$	0.0533746	0.99996
CLJAYA [57]	1.030514	3.4822628	48.64283	1.201271	981.982279	$2.42507E-03$	0.0489227	0.99997
ITLBO [59]	1.0305	3.4823	48.6428	1.2013	981.9823	$2.42519E-03$	0.0488878	0.99997
IWOA [61]	1.0305	3.4717	48.6313	1.2016	978.6771	$2.42523E-03$	0.0488933	0.99997
MLBSA [62]	1.0305	3.4823	48.6428	1.20163	981.9823	$2.42561E-03$	0.04878	0.99997
5Pm [3]	1.034	3.571	48.71	1.206	1123.00	$4.019E-03$	0.0833522	0.99991

Additionally, the GA which will be used for forecast is considered.

4.1.1. RTC France Solar Cell. The first comparison is made for the RTC France solar cell, one of the widely used by researchers to prove the performance of the developed algorithms to extract the parameters of the photovoltaic cells and panels. The result of the parameters and the statistical tests, RMSE, AE, and R^2, are presented in Table 3.

In the case of the RTC France solar cell, the 5Pm method has the RMSE, which is widely used to measure the performance of the methods, higher than the ones obtained for the metaheuristic algorithms with the exception of the GA. Also, for the AE and R^2, the values are higher.

To have a complete image of the results obtained using different methods, Figure 3(a) presents the absolute current error. The 5Pm method and GA algorithm overestimate or underestimate the current around the open-circuit voltage
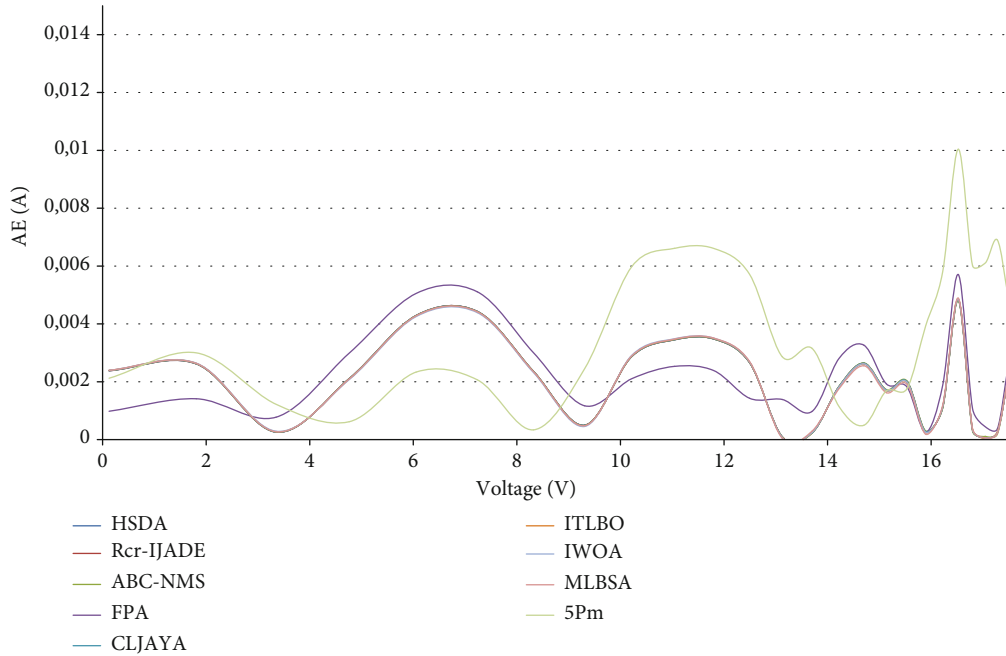
(a)
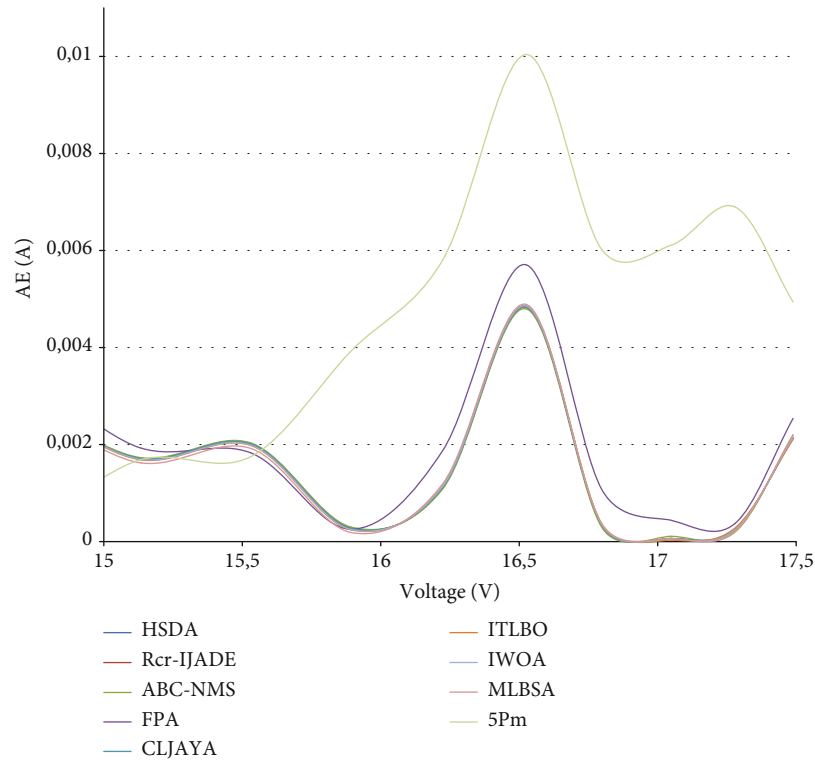
(b)

FIGURE 5: (a) The absolute current error (AE) for PWP201 photovoltaic panel; (b) AE in open-circuit voltage region.

point, where the other algorithms calculate the current better. The reverse saturation current extracted with the GA algorithm is more than two times higher than that calculated with HSDA. The parasitic resistances, the series resistance, and the shunt resistance present also a high variation. Figure 3(b) shows the behaviour of the AE around the open-circuit voltage region. The AE values for the C-

HCLPSO and FPA algorithms alternate around the AE average of the other algorithms considered, having high values for some regions and very small for other regions.

4.1.2. Commercial Monocrystalline Silicon Photovoltaic Cell. There are three methods to extract parameters of mSi commercial photovoltaic cell. The 5Pm analytical method gives

TABLE 6: The parameters and statistical tests for the STM6-40 photovoltaic panel.

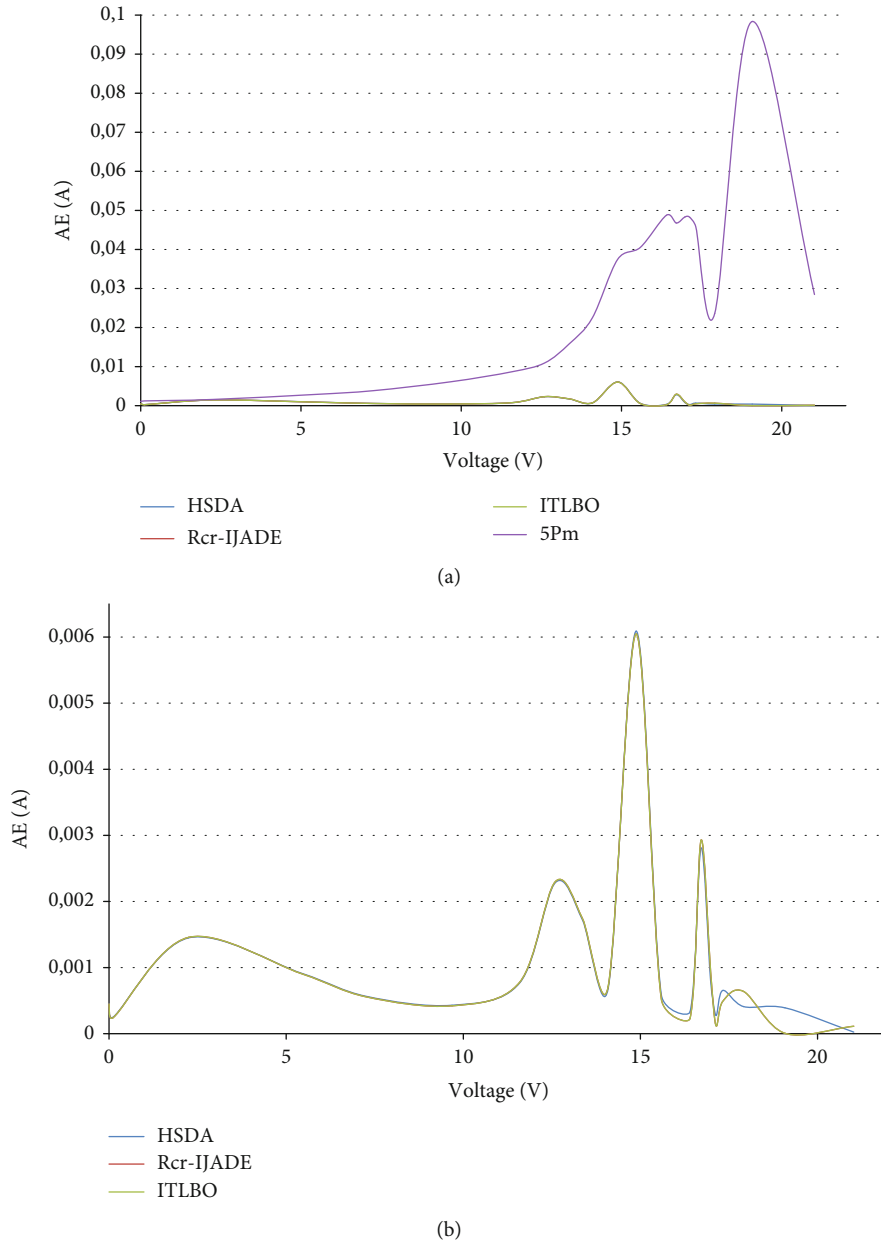| Algorithm	I_{ph} (A)	I_o (μA)	n	R_s (Ω)	R_{sh} (Ω)	RMSE	AE	R^2
HSDA [44]	1.6639047799	1.7386543978	54.730899	0.153855932	543.41834985	$1.72981E-03$	0.0219035	0.99997731
R_{cr}-IJADE [36]	1.6639	1.7387	54.7308	0.1548	573.4188	$1.73428E-03$	0.0216148	0.99997719
ITLBO [59]	1.6639	1.7387	54.7308	0.1548	573.4188	$1.73428E-03$	0.0216148	0.99997719
5Pm [3]	1.6636	$2.6541E-4$	33.3534	0.9121	898.16	$3.53507E-02$	0.540948	0.98999793

FIGURE 6: (a) The absolute current error (AE) for STM6-40 photovoltaic panel; (b) AE in open-circuit voltage region.

the weakest results for all statistical tests, Table 4. If in the case of the RTC photovoltaic cell, the RMSE obtained using the 5Pm method is almost ten times higher; for the mSi photovoltaic cell, the RMSE is 4.5 times higher, but the GA algorithm significantly improves its performance.

These changes in the performance of the methods can be easily observed in Figure 4. The performance of the GA algorithm is substantially improved for the region around the open circuit point, while the 5Pm method shows weakness in this region.

TABLE 7: The parameters and statistical tests for mSi photovoltaic panel.

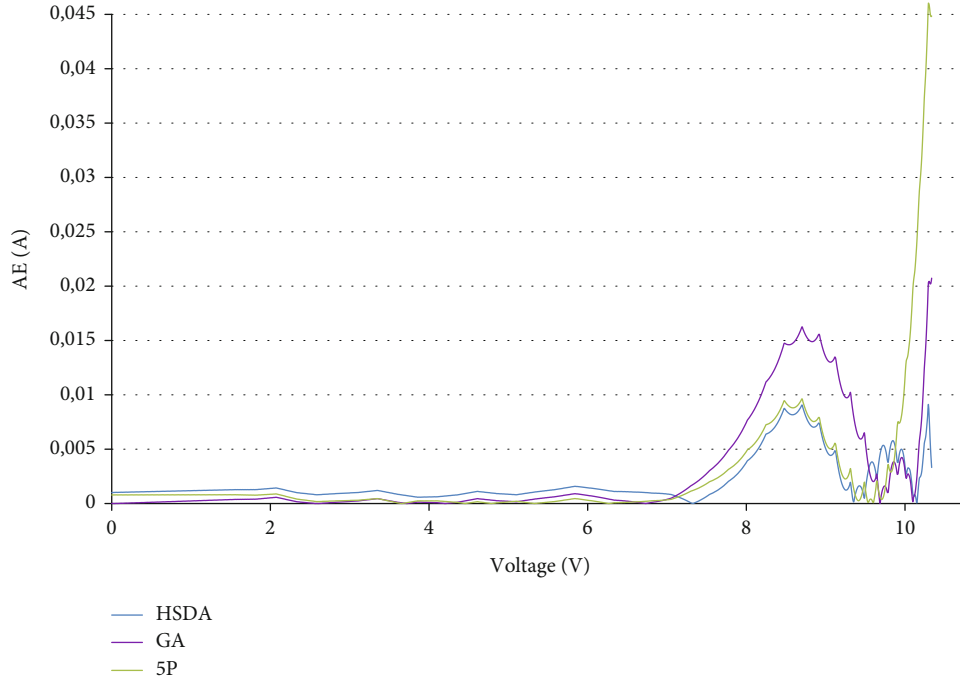| Algorithm	I_{ph} (A)	I_o (μA)	n	R_s (Ω)	R_{sh} (Ω)	RMSE	AE	R^2
HSDA [44]	1.224206	$4.677E-4$	18.364994	0.14407	1544.361724	$2.77734E-03$	1.93926	0.99956777
GA [33]	1.223082	$4.988143E-3$	20.5289	0.02147292	1765.388	$4.96271E-03$	2.61456	0.9984
5Pm [3]	1.224	$0.334E-3$	18.02	0.134	1242.91	$6.21773E-03$	2.42416	0.9978

FIGURE 7: The absolute current error for mSi photovoltaic panel.

4.1.3. PWP201 Photovoltaic Panel.

Analyzing the results obtained for RMSE in the case of the PWP201 photovoltaic panel, RMSE and AE obtained with the 5Pm method are 1.65 times higher than the ones obtained with the HSDA algorithm. There are three algorithms with the best values for all three statistical tests, HSDA, R_{cr}-IJADE, and CLJAYA, Table 5.

The absolute current errors for PWP201 photovoltaic panel are under 0.01 (A), having a uniform distribution, but keeping the high values in the open-circuit voltage region, Figure 5(a). Although, in this case, the methods estimate the current without high difference for certain voltages in comparison with the ones measured, the RMSE and AE have high values. The AE for the PWP201 photovoltaic panel around the open-circuit voltage is higher for the FPA and 5Pm methods. The other algorithms considered have the same behaviour, Figure 5(b).

4.1.4. STM6-40 Photovoltaic Panel.

The 5Pm method has the statistical test high values, Table 6. The (V, I) pairs of the STM6-40 photovoltaic panel are not uniformly distributed. There are very few points in the open-circuit voltage region [46], which leads to poorer results in this case. The value of the coefficient of determination confirms this issue.

TABLE 8: The statistical tests for the forecast I-V characteristic.

| Algorithm	RMSE f	RMSE m
HSDA [44]	$5.30433E-03$	$3.234E-03$
GA [33]	$1.63618E-02$	$6.707E-03$
5Pm [3]	$6.23956E-03$	$2.86E-02$

The best results are obtained for the HSDA algorithm for RSME and R^2. The plot of the absolute current errors, Figure 6(a), shows the weakness of the 5Pm method in the region around the open-circuit voltage. For some points, the current calculated with the 5Pm method is twenty times higher than the ones calculated with the HSDA algorithm.

The behaviour of the AE around the open-circuit voltage is similar for the ITLBO and the R_{cr}-IJADE algorithms, Figure 6(b). The AE for the HSDA algorithm has some small variations.
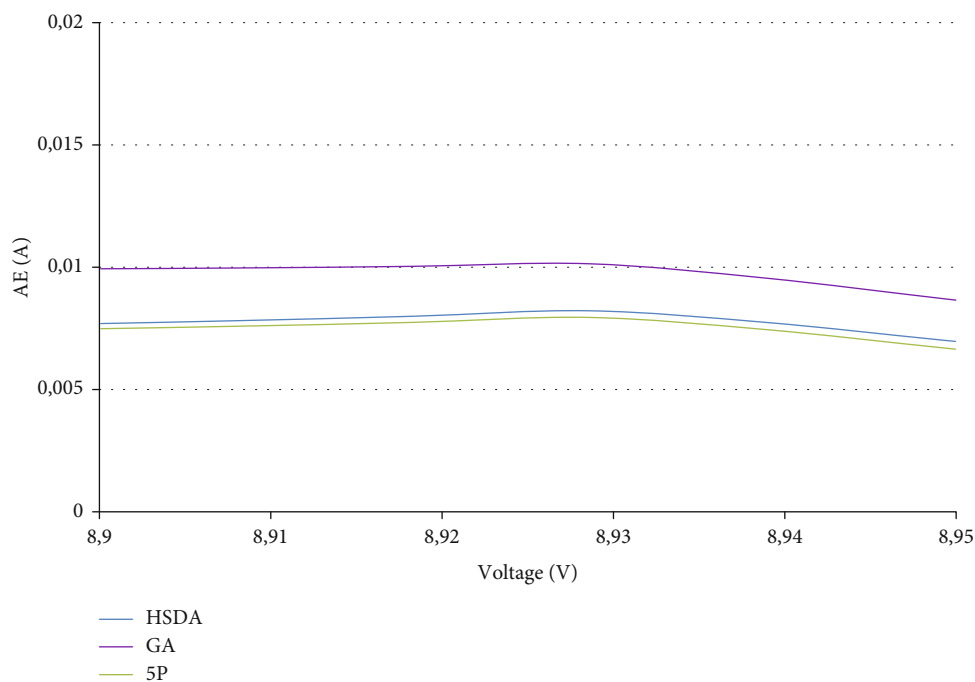
4.1.5. Commercial Monocrystalline Silicon Photovoltaic Panel.

The statistical tests for commercial mSi photovoltaic panel are presented in Table 7.

The shape of the absolute current error curves is the same in the case of the mSi photovoltaic panel. The highest
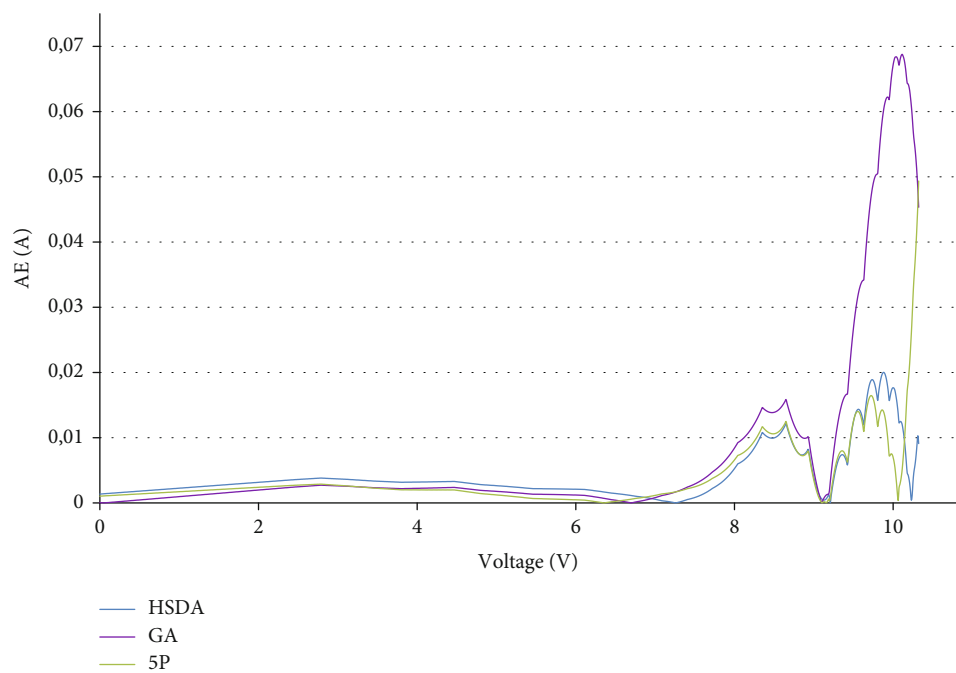
(a)

(b)

FIGURE 8: (a) The absolute current error (AE) for the forecasted I-V characteristic for photovoltaic panel; (b) AE in the voltage which corresponds to maximum power region.

value for the AE is again in the region of the open-circuit voltage, Figure 7.

The coefficient of determination for all photovoltaic cells and panels is very good, less for the GA algorithm in case of RTC photovoltaic cell and STM6-40 photovoltaic panel.

4.2. Forecast Comparison. Two I-V characteristics are measured for the commercial monocrystalline photovoltaic

TABLE 9: The P_{max} forecasted and measured.

Algorithm	HSDA [44]	GA [33]	5Pm [3]	Measured
P_{max} (W)	13.807	13.795	13.809	13.875
$P_{max,f}/P_{max,m}$ (%)	99.509	98.45	99.52	

TABLE 10: Advantages and disadvantages.

Method	Advantages	Disadvantages
Analytical	(i) Using the 5Pm method is very easy, the R_{so} and R_{sh} are calculated with the empirical equations [25] (ii) Very easy to implement on the computer for all software which allows calculation (iii) The necessary time to extract the parameters is very short for the 5Pm method (duration is under ms) (iv) Does not require a powerful or dedicated PC, which leads to the small cost of the PC, and the used software can be a common one	(i) The accuracy of the parameters extracted decreases due to approximations used [8] (ii) If some points of the I-V characteristic are used, the equation system obtained is nonlinear and it is necessary to use software that allows solving this (this can be costly) (iii) The complexity increases when the two diode model is used (seven equations are needed)
Metaheuristic	(i) The accuracy is higher than that of the analytical methods (ii) The number of iterations can be reduced (for example, for the ISCE algorithm, the iteration number is 5000) (iii) The algorithms can be easily adapted for the two diode model, but the computational time will increase (iv) Using algorithms as grey wolf, prey predator, and fire fly optimization, the performance of the parameters extraction can be improved [8] (v) GA algorithm family can easy be part of the hybrid algorithm [65] (vi) DE algorithm family has a high convergence (vii) PSO can be improved if it is used together with Nelder-Mead methods, this hybridisation can reduce the computational resources [65] (viii) SDA family has very good performance, and it can be easily used with other algorithms in hybrid structure (ix) Improved version of SCE has performance comparable with HSDA	(i) The computational time can be high, it depends on the PC power and the metaheuristic algorithm (the number of the iterations and the complexity), there are algorithms with over 100000 iterations or even 350000-NM-MPSO algorithm [41] (ii) The cost of the PC can be high and the dedicated software must be used (iii) The performance of the most metaheuristic algorithms depend by the initial parameter range (iv) Requires very good knowledge for implementation (v) GA, SCE, TLBO, WOA, and BSA algorithms have a slow convergence (vi) DE and PSO algorithms can converge prematurely (vii) The computational time is high in case of the PSO algorithms (viii) The computational time is relatively high, but using parallelization, it can be reduced; in the case presented, the time was reduced 6 times

panel for the irradiance of 700 W/m² and 983 W/m². The measurements were made on the roof of the university building [3].

The I-V characteristic measured at 700 W/m² was used to extract the parameters of the mSi photovoltaic panel with three methods HSDA algorithm, GA algorithm, and 5Pm analytical method. These parameters are considered as $I_{\mathrm{ph,ref}}$, $I_{\mathrm{o,ref}}$, n_{ref}, $R_{\mathrm{s,ref}}$, and $R_{\mathrm{sh,ref}}$. The parameters of the mSi photovoltaic panel are calculated for 983 W/m² irradiance, using Equations (7)–(11). These values are used to compare the measured I-V characteristic for 983 W/m² in real conditions with the ones forecasted with the five parameters calculated with Equations (7)–(11). The temperature coefficient of the current was determined, and it is 15.76 mA/°C.

The root mean square error for the forecasted I-V characteristic of the mSi photovoltaic panel is presented in Table 8 in comparison with one for the I-V characteristic measured. The RMSE f obtained when the parameters are calculated with Equations (7)–(11) is worse in the case of the HSDA and GA algorithms than the RMSE m obtained using the extracted parameters with those algorithms for the measured characteristic. In case of the 5Pm methods, the results are improved.

The absolute current error calculated for the forecast I-V characteristic in comparison with the ones measured is presented in Figure 8(a). The highest values for AE are in the region of the open-circuit voltage. The behaviour of the

curves obtained with parameters calculated with Equations (7)–(11) for HSDA and 5Pm methods is very similar, while the ones obtained with GA algorithms have an accentuated increase in the open-circuit voltage region.

Figure 8(b) shows the behaviour of the absolute current error around the maximum voltage, V_m, which is the voltage coordinate for the maximum power point. The best results are obtained for the 5Pm method for all regions considered.

The comparison between maximum power generated, $P_{\mathrm{max},m}$, the mSi panel calculated from real measurements and ones forecasted, $P_{\mathrm{max},f}$, using the extracted parameters with the three methods, Table 9, shows that the best estimation is for the maximum power estimated with parameters extracted with the 5Pm method.

By analyzing the results obtained through comparison between the analytic method and metaheuristic algorithms, it can be concluded that the 5Pm method can be used to extract the parameters of the photovoltaic cells and panels. Additionally, the analytical method can be used to estimate the I-V characteristics and the power generated using the parameters given by the producers. It can be used due to the advantages which are presented in Table 10.

5. Conclusions

The paper briefly reviews the analytical methods and metaheuristic algorithms used to extract the five or seven parameters for the photovoltaic cells and panels. The 5Pm

analytical method and ones of the best metaheuristic algorithms from different families are compared for five datasets, two for photovoltaic cells, and three for photovoltaic panels.

By analyzing the results obtained, the supremacy of the metaheuristic algorithms for accuracy is shown. In all cases studied, the algorithms have better results for all statistical tests used. The analytical method has a better performance than the GA algorithm for the RTC photovoltaic cell. The performance of the HSDA algorithm is one of the best for all photovoltaic cells and panels analyzed, and it was chosen to be compared in the forecast process.

Two I-V characteristics, measured for the commercial mSi photovoltaic panel, are used to compare the influence of the extract parameter methods on the forecast of the maximum power and I-V characteristic at different values of the irradiance and temperature. Using the parameters calculated with the HSDA algorithm, the forecast of the I-V characteristic was better than for GA and 5Pm methods. However, the 5Pm method forecasted better the maximum power, only 0.48% less than the real one. These are preliminary results, which will further be developed in future research by analysis for various cases. This analysis will be made on different panels, under various irradiance and illumination conditions.

The 5Pm methods are based on several relations which are easy to implement, for the measured I-V characteristic, datasets, or the datasheet parameters, the latter offered by the producer, and the parameters can be quickly calculated with very good accuracy. The necessary time to calculate the parameters is very small, and it does not require a powerful PC, as for the metaheuristic algorithms. These prove that the 5Pm method is a valuable candidate for photovoltaic cells and panel manufacturers. They can use the 5Pm method to characterize the photovoltaic devices and to obtain the optimum photovoltaic panels using cells with the same values of the parameters. The production time and the costs can be optimized.

Conflicts of Interest

The authors declare that there is no conflict of interest regarding the publication of this paper.

Acknowledgments

References

[1] D. T. Cotfas, P. A. Cotfas, and S. Kaplanis, "Methods to determine the dc parameters of solar cells: a critical review," *Renewable and Sustainable Energy Reviews*, vol. 28, pp. 588–596, 2013.

[2] A. M. Humada, M. Hojabri, S. Mekhilef, and H. M. Hamada, "Solar cell parameters extraction based on single and double-diode models: a review," *Renewable and Sustainable Energy Reviews*, vol. 56, pp. 494–509, 2016.

[3] D. T. Cotfas, A. M. Deaconu, and P. A. Cotfas, "Application of successive discretization algorithm for determining photovoltaic cells parameters," *Energy Conversion and Management*, vol. 196, pp. 545–556, 2019.

[4] D. Sera, R. Teodorescu, and P. Rodriguez, "PV panel model based on datasheet values," in *2007 IEEE International Symposium on Industrial Electronics*, pp. 2392–2396, Vigo, Spain, 2007.

[5] J. P. Ram, H. Manghani, D. S. Pillai, T. S. Babu, M. Miyatake, and N. Rajasekar, "Analysis on solar PV emulators: a review," *Renewable and Sustainable Energy Reviews*, vol. 81, pp. 149–160, 2018.

[6] G. Huang, Y. Liang, X. Sun, C. Xu, and F. Yu, "Analyzing S-Shaped _I_ - _V_ characteristics of solar cells by solving three-diode lumped-parameter equivalent circuit model explicitly," *Energy*, vol. 212, p. 118702, 2020.

[7] A. Elkholy and A. A. Abou El-Ela, "Optimal parameters estimation and modelling of photovoltaic modules using analytical method," *Heliyon*, vol. 5, no. 7, article e02137, 2019.

[8] D. S. Pillai and N. Rajasekar, "Metaheuristic algorithms for PV parameter identification: a comprehensive review with an application to threshold setting for fault detection in PV systems," *Renewable and Sustainable Energy Reviews*, vol. 82, no. 3, pp. 3503–3525, 2018.

[9] J. Bai, S. Liu, Y. Hao, Z. Zhang, M. Jiang, and Y. Zhang, "Development of a new compound method to extract the five parameters of PV modules," *Energy Conversion and Management*, vol. 79, pp. 294–79303, 2014.

[10] M. Kumar and A. Kumar, "An efficient parameters extraction technique of photovoltaic models for performance assessment," *Solar Energy*, vol. 158, pp. 192–206, 2017.

[11] D. T. Cotfas, P. A. Cotfas, and O. M. Machidon, "Study of temperature coefficients for parameters of photovoltaic cells," vol. 2018, 2018International Journal of Photoenergy, 2018.

[12] B. Van Zeghbroeck, *Principles of Semiconductor Devices and Heterojunctions*, Prentice Hall, Englewood Cliffs, New Jersey, 1st edition, 2008.

[13] M. Wolf and H. Rauschenbach, "Series resistance effects on solar cell measurements," *Advanced Energy Conversion*, vol. 3, no. 2, pp. 455–479, 1963.

[14] A. Virtuani, E. Lotter, and M. Powalla, "Performance of Cu(In,Ga)Se$_2$ solar cells under low irradiance," *Thin Solid Films*, vol. 431-432, pp. 443–447, 2003.

[15] S. Nesmachnow, "An overview of metaheuristics: accurate and efficient methods for optimisation," *International J. Metaheuristics*, vol. 3, no. 4, pp. 320–347, 2014.

[16] D. S. H. Chan, J. R. Phillips, and J. C. H. Phang, "A comparative study of extraction methods for solar cell model parameters," *Solid-State Electronics*, vol. 29, no. 3, pp. 329–337, 1986.

[17] M. Tivanov, A. Patryn, N. Drozdov, A. Fedotov, and A. Mazanik, "Determination of solar cell parameters from its current-voltage and spectral characteristics," *Solar Energy Materials and Solar Cells*, vol. 87, no. 1-4, pp. 457–465, 2005.

[18] A. Ortiz-Conde, F. J. G. Sánchez, and J. Muci, "New method to extract the model parameters of solar cells from the explicit analytic solutions of their illuminated _I -V_ characteristics," *Solar Energy Materials and Solar Cells*, vol. 90, no. 3, pp. 352–361, 2006.

[19] C. L. Garrido-Alzar, "Algorithm for extraction of solar cell parameters from I-V curve using double exponential model," *Renewable Energy*, vol. 10, no. 2-3, pp. 125–128, 1997.

[20] B. Arcipiani, "Generalization of the area method for the determination of the parameters of a non-ideal solar cell," *Revue de Physique Appliquée*, vol. 20, no. 5, pp. 269–272, 1985.

[21] G. L. Araujo and E. Sanchez, "A new method for experimental determination of the series resistance of a solar cell," *IEEE Transactions on Electron Devices*, vol. 29, no. 10, pp. 1511–1513, 1982.

[22] A. Kaminski, J. J. Marchand, A. Fave, and A. Laugier, "New method of parameters extraction from dark I–V curve," in *Conference Record of the Twenty Sixth IEEE Photovoltaic Specialists Conference - 1997*, pp. 203–206, Anaheim, CA, USA, 1997.

[23] N. N. Ulapane, C. H. Dhanapala, S. M. Wickramasinghe, S. G. Abeyratne, N. Rathnayake, and P. J. Binduhewa, "Extraction of parameters for simulating photovoltaic panels," in *2011 6th International Conference on Industrial and Information Systems*, pp. 539–544, Kandy, Sri Lanka, 2011, IEEE.

[24] F. Ghani and M. Duke, "Numerical determination of parasitic resistances of a solar cell using the Lambert W-function," *Solar Energy*, vol. 85, no. 9, pp. 2386–2394, 2011.

[25] O. Mares, M. Paulescu, and V. Badescu, "A simple but accurate procedure for solving the five-parameter model," *Energy Conversion and Management*, vol. 105, pp. 139–148, 2015.

[26] R. Ndegwa, J. Simiyu, E. Ayieta, and N. Odero, "A Fast and accurate analytical method for parameter determination of a photovoltaic system based on manufacturer's data," *Journal of Renewable Energy*, vol. 2020, 7580218 pages, 2020.

[27] A. Hali and Y. Khlifi, "Photovoltaic panel parameters determination using two numerical methods," *Materials Today: Proceedings*, vol. 45, pp. 7377–7382, 2021.

[28] V. Lo Brano and G. Ciulla, "An efficient analytical approach for obtaining a five parameters model of photovoltaic modules using only reference data," *Applied Energy*, vol. 111, pp. 894–903, 2013.

[29] A. Orioli and A. Di Gangi, "A criterion for rating the usability and accuracy of the one-diode models for photovoltaic modules," *Energies*, vol. 9, no. 6, p. 427, 2016.

[30] A. M. Humada, S. Y. Darweesh, K. G. Mohammed et al., "Modeling of PV system and parameter extraction based on experimental data: review and investigation," *Solar Energy*, vol. 199, pp. 742–760, 2020.

[31] J. A. Jervase, H. Bourdoucen, and A. Al-Lawati, "Solar cell parameter extraction using genetic algorithms," *Measurement Science and Technology*, vol. 12, no. 11, pp. 1922–1925, 2001.

[32] M. Zagrouba, A. Sellami, M. Bouaicha, and M. Ksouri, "Identification of PV solar cells and modules parameters using the genetic algorithms: application to maximum power extraction," *Solar Energy*, vol. 84, no. 5, pp. 860–866, 2010.

[33] D. T. Cotfas, P. A. Cotfas, and A. Cataron, "Using the genetic algorithm to determine the parameters of photovoltaic cells and panels," in *2018 International Symposium on Electronics and Telecommunications (ISETC)*, pp. 1–4, Timisoara, Romania, November 2018.

[34] X. Lingyun, S. Lefei, H. Wei, and J. Cong, "Solar cells parameter extraction using a hybrid genetic algorithm," in *2011 Third International Conference on Measuring Technology and Mechatronics Automation*, pp. 306–309, Shanghai, China, 2011.

[35] X. Yang, W. Gong, and L. Wang, "Comparative study on parameter extraction of photovoltaic models via differential evolution," *Energy Conversion and Management*, vol. 201, p. 112113, 2019.

[36] W. Gong and Z. Cai, "Parameter extraction of solar cell models using repaired adaptive differential evolution," *Solar Energy*, vol. 94, pp. 209–220, 2013.

[37] K. Ishaque, Z. Salam, S. Mekhilef, and A. Shamsudin, "Parameter extraction of solar photovoltaic modules using penalty-based differential evolution," *Applied Energy*, vol. 99, pp. 297–308, 2012.

[38] D. H. Muhsen, A. B. Ghazali, T. Khatib, and I. A. Abed, "Parameters extraction of double diode photovoltaic module's model based on hybrid evolutionary algorithm," *Energy Conversion and Management*, vol. 105, pp. 552–561, 2015.

[39] H. Wei, J. Cong, X. Lingyun, and S. Deyun, "Extracting solar cell model parameters based on chaos particle swarm algorithm," in *2011 International Conference on Electric Information and Control Engineering*, pp. 398–402, Wuhan, China, 2011.

[40] V. Khanna, B. K. Das, D. Bisht, Vandana, and P. K. Singh, "A three diode model for industrial solar cells and estimation of solar cell parameters using PSO algorithm," *Renewable Energy*, vol. 78, pp. 105–113, 2015.

[41] N. F. A. Hamid, N. A. Rahim, and J. Selvaraj, "Solar cell parameters identification using hybrid Nelder-Mead and modified particle swarm optimization," *Journal of Renewable and Sustainable Energy*, vol. 8, no. 1, 2016.

[42] D. Yousri, S. B. Thanikanti, D. Allam, V. K. Ramachandaramurthy, and M. Eteiba, "Fractional chaotic ensemble particle swarm optimizer for identifying the single, double, and three diode photovoltaic models' parameters," *Energy*, vol. 195, p. 116979, 2020.

[43] D. Yousri, D. Allam, M. Eteiba, and P. N. Suganthan, "Static and dynamic photovoltaic models' parameters identification using Chaotic Heterogeneous Comprehensive Learning Particle Swarm Optimizer variants," *Energy Conversion and Management*, vol. 182, pp. 546–563, 2019.

[44] D. T. Cotfas, A. M. Deaconu, and P. A. Cotfas, "Hybrid successive discretisation algorithm used to calculate parameters of the photovoltaic cells and panels for existing datasets," *IET Renewable Power Generation*, pp. 1–27, 2021.

[45] A. M. Deaconu, D. T. Cotfas, and P. A. Cotfas, "Calculation of seven photovoltaic cells parameters using parallelized successive discretization algorithm," *International Journal of Photoenergy*, vol. 2020, Article ID 6669579, 13 pages, 2020.

[46] D. Oliva, E. Cuevas, and G. Pajares, "Parameter identification of solar cells using artificial bee colony optimization," *Energy*, vol. 72, pp. 93–102, 2014.

[47] Z. Chen, L. Wu, P. Lin, Y. Wu, and S. Cheng, "Parameters identification of photovoltaic models using hybrid adaptive Nelder- Mead simplex algorithm based on eagle strategy," *Applied Energy*, vol. 182, pp. 47–57, 2016.

[48] X. Gao, Y. Cui, J. Hu et al., "Parameter extraction of solar cell models using improved shuffled complex evolution algorithm," *Energy Conversion and Management*, vol. 157, pp. 460–479, 2018.

[49] Y. Chen, Z. Chen, L. Wu, C. Long, P. Lin, and S. Cheng, "Parameter extraction of PV models using an enhanced shuffled complex evolution algorithm improved by opposition-based learning," *Energy Procedia*, vol. 158, pp. 991–997, 2019.

[50] F. Dkhichi, B. Oukarfi, A. Fakkar, and N. Belbounaguia, "Parameter identification of solar cell model using Levenberg-Marquardt algorithm combined with simulated annealing," *Solar Energy*, vol. 110, pp. 781–788, 2014.

[51] D. F. Alam, D. A. Yousri, and M. B. Eteiba, "Flower pollination algorithm based solar PV parameter estimation," *Energy Conversion and Management*, vol. 101, pp. 410–422, 2015.

[52] J. P. Ram, T. S. Babu, T. Dragicevic, and N. Rajasekar, "A new hybrid bee pollinator flower pollination algorithm for solar PV parameter estimation," *Energy Conversion and Management*, vol. 135, pp. 463–476, 2017.

[53] A. Askarzadeh and A. Rezazadeh, "Parameter identification for solar cell models using harmony search-based algorithms," *Solar Energy*, vol. 86, no. 11, pp. 3241–3249, 2012.

[54] M. F. AlHajri, K. M. el-Naggar, M. R. AlRashidi, and A. K. al-Othman, "Optimal extraction of solar cell parameters using pattern search," *Renewable Energy*, vol. 44, pp. 238–245, 2012.

[55] K. Yu, J. Liang, B. Qu, X. Chen, and H. Wang, "Parameters identification of photovoltaic models using an improved JAYA optimization algorithm," *Energy Conversion and Management*, vol. 150, pp. 742–753, 2017.

[56] K. Yu, B. Qu, C. Yue, S. Ge, X. Chen, and J. Liang, "A performance-guided JAYA algorithm for parameters identification of photovoltaic cell and module," *Applied Energy*, vol. 237, pp. 241–257, 2019.

[57] Y. Zhang, M. Ma, and Z. Jin, "Comprehensive learning Jaya algorithm for parameter extraction of photovoltaic models," *Energy*, vol. 211, p. 118644, 2020.

[58] S. J. Patel, A. K. Panchal, and V. Kheraj, "Extraction of solar cell parameters from a single current-voltage characteristic using teaching learning based optimization algorithm," *Applied Energy*, vol. 119, pp. 384–393, 2014.

[59] S. Li, W. Gong, X. Yan et al., "Parameter extraction of photovoltaic models using an improved teaching- learning-based optimization," *Energy Conversion and Management*, vol. 186, pp. 293–305, 2019.

[60] O. S. Elazab, H. M. Hasanien, M. A. Elgendy, and A. M. Abdeen, "Parameters estimation of single- and multiple-diode photovoltaic model using whale optimisation algorithm," *IET Renewable Power Generation*, vol. 12, no. 15, pp. 1755–1761, 2018.

[61] G. Xiong, J. Zhang, D. Shi, and Y. He, "Parameter extraction of solar photovoltaic models using an improved whale optimization algorithm," *Energy Conversion and Management*, vol. 174, pp. 388–405, 2018.

[62] K. Yu, J. Liang, B. Qu, Z. Cheng, and H. Wang, "Multiple learning backtracking search algorithm for estimating parameters of photovoltaic models," *Applied Energy*, vol. 226, pp. 408–422, 2018.

[63] Y. Zhang, Z. Jin, X. Zhao, and Q. Yang, "Backtracking search algorithm with Levy flight for estimating parameters of photovoltaic models," *Energy Conversion and Management*, vol. 208, p. 112615, 2020.

[64] K. M. el-Naggar, M. R. AlRashidi, M. F. AlHajri, and A. K. al-Othman, "Simulated annealing algorithm for photovoltaic parameters identification," *Solar Energy*, vol. 86, no. 1, pp. 266–274, 2012.

[65] S. Li, W. Gong, and Q. Gu, "A comprehensive survey on meta-heuristic algorithms for parameter extraction of photovoltaic models," *Renewable and Sustainable Energy Reviews*, vol. 141, p. 110828, 2021.

Research Article

Solar Hybrid System Component Study in Low Concentrated Sunlight

Petru A. Cotfas and **Daniel T. Cotfas**

Department of Electronics and Computers, Faculty of Electrical Engineering and Computer Science, Transilvania University of Brasov, 500036, Romania

Correspondence should be addressed to Petru A. Cotfas; pcotfas@unitbv.ro

The solar energy is increasingly used as a renewable energy source. Raising the efficiency of energy conversion from solar to useful energy (electric and thermal) represents an important research direction in the renewable energy domain. Using hybrid systems for electric and thermal energy cogeneration can be a solution. In this study, a hybrid system (HS) is designed, manufactured, implemented, and experimentally tested under concentrated sunlight with a concentration ratio of 25 suns, obtained using a Fresnel lens as a sunlight concentrator. The HS comprises of four concentrated photovoltaic cells (CPVs), four thermoelectric generators (TEGs), and a solar thermal collector (STC). The HS is studied in three configurations of the exposed surface: only the CPV active area, the CPV active area with ceramic support, and the CPV active area with ceramic support covered with graphite sheet. Results reveal that the efficiency of each system component is affected by the exposed surface. If the efficiencies of the CPVs decrease from 32.3% to 30.8% from the first configuration to the last one, the efficiencies of TEGs and STC increase from 0.12% to 0.44 and from 26.3% to 52.0%, respectively. Increasing the concentration ratio from 25 to 33 suns, the power of the CPVs increases with almost 31%, but the efficiency decreases slightly, instead the efficiencies of the TEGs and STC increase.

1. Introduction

Nowadays, renewable energy sources provide an important part of the total energy used worldwide. In order to increase the usability of renewable energy sources however, their efficiency needs to be improved. Such a method of increasing efficiency is the use of hybridisation, and such a hybrid system (HS) can be assembled from a photovoltaic cell (PV) with a thermoelectric generator (TEG), a PV with a solar thermal collector (STC), or PV-TEG-STC. The PV efficiency decreases with the increase of its temperature. The multi-junction cell conversion efficiency in high concentration ratio can reach over 45% [1]. The solar absorbance of a PV has a range from 80% up to 93% [2], which means that a large percent of the sunlight is converted into heat, which increases the PV temperature. There are many solutions used for cooling the PVs [3, 4], and the ones most widely used being based on water cooling systems, such as water spraying on the PV surface [5], forced water circulation through thermal collect-

ing pipes attached to the back of the PV module [6, 7] forming a PV/STC system and water immersion of the PV [8]. There are PV cooling systems based on air streams [9, 10] or based on thermoelectric coolers [11]. Recent studies based on numerical [12] and experimental [13] approaches are focused on passive cooling of PV panels. In [13], a passive air cooling was implemented based on aluminium fins leading to an increasing in the power yield with approximately 5%. The solutions mentioned in [5, 8–13] are based on removing the thermal energy from the PV and eliminating in the environment without using it. Instead of eliminating the thermal energy, another approach is to use it. Based on this approach, a solution is to use the TEG as an electrical energy cogenerator, based on the temperature differences between PV and STC and using the STC as a thermal energy source. Such a system was studied in natural conditions by Cotfas et al. [14] showing that the output power of the PV integrated in the HS increased with more than 11% due to its temperature decreases. An important conclusion that

resulted from this study is that the stabilization time for the studied HS configurations was around 7 min. The effect of integrating a TEG in a HS could be negative due to its thermal resistance that is introduced between PV and the cooling system. There are many studies about the optimization of the HS from the perspectives of the material, geometry, thermal, and electrical connection. Li et al. [15] analysed a PV/TEG HS based on the geometrical parameters of the TEG, solar irradiance, and the cold side temperature, and they reported that the overall efficiency of the HS shown a proportional dependence with the cross-sectional area of the TEG and inversely proportional dependence with the height of the TEG and with the cold side temperature.

Rezania and Rosendahl [16] showed that a TEG used between the concentrated photovoltaic cell (CPV) and a heatsink increases the thermal resistance, which conducts to a higher temperature and consequently the CPV efficiency decreases. However, the overall system efficiency is enhanced due to the electrical cogeneration of both CPV and TEG. Kil et al. [17] showed that the total efficiency of the CPV/STC systems becomes higher than of a single CPV if the concentration ratio is higher than 35 suns. Liao et al. [18] describe a theoretical study of a PV/TEG system in low concentration ratio offering some criteria for an optimal design of such a system. According to this study, the PV/TEG design should consider the concentration ratio and the current through system components. Saeedi et al. [19] show that in a PV/STC system, the water flow rate can affect the performance of the system. A change in the water flow rate from 0.001 kg/s to 0.044 kg/s increases the efficiency of the system from approximately 17% to the optimum value of 21.56%.

In concentrated sunlight, the cooling system for the PV is mandatory; therefore, using the CPV/TEG/STC system as a hybrid energy source becomes a feasible approach. A comprehensive review regarding the CPV/STC systems used in concentrated light covering the aspects as components design, heat transfer medium, applications, and economics was done by George et al. [20]. They found that the contradictory requirements of the components from electrical and thermal efficiency point of view could affect the HS efficiency without components optimization. At the same time, different parameters of the fluid used (like mass flow rate, density, viscosity, time, and desired temperature) can affect the performances of the thermal components.

The concentrated sunlight can be obtained using different techniques: there are sunlight concentrators based on parabolic reflectors, heliostats, Fresnel reflectors, or Fresnel lens with different shapes [21, 22]. For HSs, these concentrators could be with or without spectral beam splitter [23].

Yazdanifard et al. [24] studied the effect of the flow regime, the length and diameter of the used pipes, and the nanofluids used as working fluids for a parabolic trough a CPV/STC system through simulation and compared the results with a flat PV/STC system. They found that the laminar or turbulent flow regime can affect the total energy efficiency of the system. The combination of the CPV/STC and TEG was studied in [25] through simulation and validated through experiment. For light concentration, a parabolic trough concentrator was used. Riahi et al. found that the electrical efficiency of the CPV/TEG/STC was enhanced by 7.46% in comparison to the CPV/STC. Also, in this paper, it was estimated that the annual electric energy generated by the CPV/TEG/STC system could be increased by 359 kWh due to the TEG electrical cogeneration. Mahmoudinezhad et al. [26] studied the transient behaviour of a CPV-TEG system in low concentration light ratio using numerical simulation and validation through a solar simulator. In transient conditions, the response of the CPV is rapid; instead, the TEG response is slower due to the thermal capacity and thermal resistance. Due to this behaviour, the TEG as component of the HS represents a way to stabilize the overall power output of HS.

The configuration of the HS is also very important. HS studied by [25] proposed to have two systems, a CPV/STC and a TEGS/STC which are placed side by side. This configuration exploits the maximum irradiance for both CPV and TEG but double the surface of the HS. Mohammadnia et al. [27] developed a model for a HS compose of CPV, TEG, and Stirling engine using a parabolic solar dish concentrator and a beam splitter. They found that overall conversion efficiency of the HS was 21.8% at 455.8 suns. Other approach is to place all three components of the HS in sandwich structure (one over the other). Each time a TEG is used, a heat sink should be placed on the cold side of TEG in order to remove the heat. During the study of the transient behaviour of the CPV/TEG HS [26, 28], the temperature of the TEG cold side varies up 10°C even while using water cooled heat sink. Therefore, instead of dissipating the heat, it can be converted in useful thermal energy. The sandwich approach was adopted in [29], in artificial conditions, in [14], under natural light, and in [30], under concentrated light using a solar simulator.

For HS, a key factor is the thermal management of high system performance. In analysing the abovementioned studies for HS, the absorbance of the exposed surface to the sun is not studied in depth. In this paper, we focused on studying the CPV/TEG/STC HS, with sandwich structure, in real conditions, considering different surface exposure to determine the effect of heat absorption on efficiency of each HS component. This aspect should be studied due to the opposing requirements of the HS components. While the CPV requires low temperature, the other components require large temperature differences, so high temperatures are needed. We consider the cases of exposing to the irradiance only the active CPV area and the entire CPVs' area including the support, and in the third case, we use a heat absorber. As concentrator, a plan Fresnel lens is used that allows us to study the HS at low concentrated sun ratio, according to [31], where three sunlight concentrator classes are considered: low concentration class with the rage of 1-40 suns, medium concentration class with the range of 40-300 suns, and high concentration class with the range of 300-2000 suns.

The rest of this paper is structured as follows: the second section describes all aspects regarding the experimental setup that include the structure of the HS, the sun tracker used, the sun concentrator, and the developed measurement systems used to characterize the HS components, the third section is dedicated to results and discussions that cover the

measurements and analysis of all three HS components, and the fourth section is dedicated to conclusions. The results obtained through this experimental study can be used as references for HS design from the heat absorption optimization point of view.

2. Experimental Setup

2.1. Hybrid System. The hybrid system (HS) is built as a sandwich structure formed by four concentrated photovoltaic cells (CPVs), four thermoelectric generators (TEGs) placed between the CPVs, and a solar flat thermal collector (STC) (see Figure 1). The entire HS was placed into a thermal insolating box leaving opened only the top surface.

The CPVs are concentrating triple-junction photovoltaic cells (InGaP/InGaAs/Ge) which are designed for working in concentrated sunlight, manufactured by SolAero Technologies [32]. The CPV characteristic parameters are shown in Table 1. We used four CPVs with the active area of $1 \, cm^2$, placed on a $2 \, cm \times 2 \, cm \times 1 \, mm$ ceramic support (Al_2O_3) that has direct bonded copper with Au/Ni surface plating. The CPVs are connected two by two in series.

TEGs are Bi_2Te_3 type, manufactured by Stonecold, model TEC1-12710 [33], and all four are connected in series. The TEG characteristic parameters are shown in Table 1.

The STC is made from a copper block milled in an interdigitated channel shape. The size of the STC is $8 \, cm \times 8 \, cm \times 1 \, cm$.

The four CPVs are placed on a cooper plate using a thermal conductive double adhesive tape with thermal conductivity $2.5 \, W/m \bullet K$. The copper plate (2 mm thick) is used for uniform heat distribution on the TEGs' top surface and also in order to have space for placing the thermocouples on the TEGs' surface (into milled channels in the copper plate). The thermal connections between TEGs' surfaces and STC and cooper plate are assured with a thermal conductive paste with the thermal conductivity of $3.8 \, W/m \bullet K$.

2.2. Sun Tracker. In order to concentrate the sunlight, the system was designed to follow the sun's movement. Hence, a sun tracker was implemented based on a J-PT-1008D-1 device, manufactured by JEC Electronics Technology, that has two degrees of freedom. The J-PT-1008D-1 device has the horizontal rotational angle of 356° and the vertical rotational angle of ±70°. Two PD30 optical encoders with 1000PPR were added to the J-PT-1008D-1 device for implementing a closed loop control for the sun tracker. The sun tracker is controlled using a NI myRIO device in which a mathematical algorithm was implemented.

2.3. Sunlight Concentrator (SLC). The SLC is built along a Fresnel lens with the size of $33 \, cm \times 33 \, cm$ made from polymethyl-methacrylate. The optical efficiency of the used Fresnel lens, η_{FL}, is 83% [34]. The Fresnel lens is fixed on the main support using four threaded rods which allow modifying the distance between the Fresnel lens and the hybrid system (HS). The HS is placed on a secondary support that can be moved towards the Fresnel lens using a linear actuator driven by a stepper motor.

2.4. Measurement Systems. The measurement system diagram is shown in Figure 2. For measuring the important parameters of the HS, a NI cRIO 9074 platform with dedicated current, voltage, and temperature modules was used together with a self-designed electronic load, EL. The EL was developed based on the variation of a prepolarized capacitor impedance during the discharging/charging process and was used for measuring the I-V characteristics of the CPVs and TEG arrays. A simplified one channel schemata of the EL is shown in Figure 2. In the first stage, the switch connects the capacitor C to the voltage source V through the resistance R and it is negatively charged. In the second stage, the capacitor is connected through the switch S to the PV. In this stage, C is discharging on the PV and then is positively charging from the PV. In this manner, the influence of circuit resistance is eliminated assuring that the entire I-V characteristic is obtained (from *Isc* to *Voc*). The temperature measurements are done with K-type thermocouples, which are placed on the top of each CPV support, between Cu plate and TEG, between TEG and STC, and at inlet and outlet of the STC.

The I/O modules on NI cRIO used for measurements were as follows: the NI 9215 voltage input module with ±10 V input range and 16-bit resolution, NI 9225 current input module with 5 A_{RMS} input range and 24-bit resolution, and NI 2013 and NI 9211 modules dedicated for temperature measurements based on thermocouples. The two temperature measurement modules have 78.125 mV and ±80 mV input range, respectively, and 24-bit resolution. The accuracies of the used modules are as follows: for voltage module is 0.2%, for current module ±0.37%, and for the temperature measurements less than 0.07°C.

The water flow is measured with the FCH-m-POM-LC flowmeter which has an accuracy of 2%. The solar irradiance is measured using the SPN1 Delta T pyranometer that offers information about global and diffuse irradiances. Using the two irradiances, the direct irradiance can be calculated. The SPN1 has a resolution of $0.6 \, W/m^2$ and an uncertainty of 5%.

The software applications for measuring, controlling, and data analysis were developed using NI LabVIEW. The entire system is shown in Figure 3. More details about the experimental system are presented in [35]. In order to minimize the errors due to the electronic noise on the system, a rectangular smoothing algorithm was applied with a smooth width of 75 points for voltage and current measurements and a smooth width of 3 points for temperature measurements.

The flow chart of the measurements is shown in Figure 4. The measurement procedure has the following structure:

(i) At the beginning, the PC synchronizes the clocks of the NI cRIO and NI myRIO devices with the PC clock. Then, the sun tracker is moved to the reference position (azimuth and altitude angles equal to zero)

(ii) It is verified if the time is in the day interval. In the true case, the sun tracker is moved to the sun position. The system waits for a predefined time t_W. Then, NI cRIO controls the three channels of EL for measuring the I-V characteristics of the two CPV arrays (two channels)
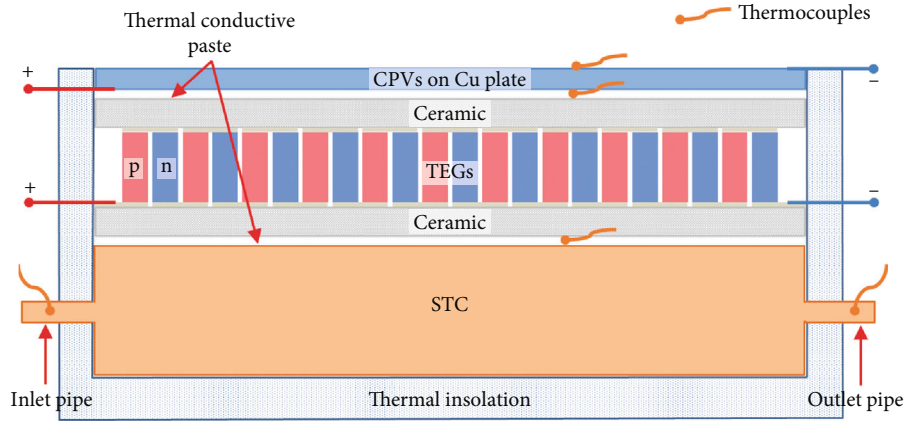
FIGURE 1: HS structure.

TABLE 1: The CPV and TEG parameters according to their datasheet.

HS components	Dimensions per device	Efficiency (%)	Short circuit current–Isc (A)	Open circuit voltage–Voc (V)	Maximum current–Imp (A)	Maximum voltage–Vmp (V)
CPV at 500 suns and 25°C	1 cm × 1 cm	39.6	6.48	3.19	6.34	2.76
		No. of couples	Internal resistance (Ω)	Resistivity at 25°C (Ωm)	Seebeck coefficient of a thermoelectric element (µV/K)	
TEGs	4 cm × 4 cm × 3.3 mm	127	1.08	1.67×10^{-5}	116	
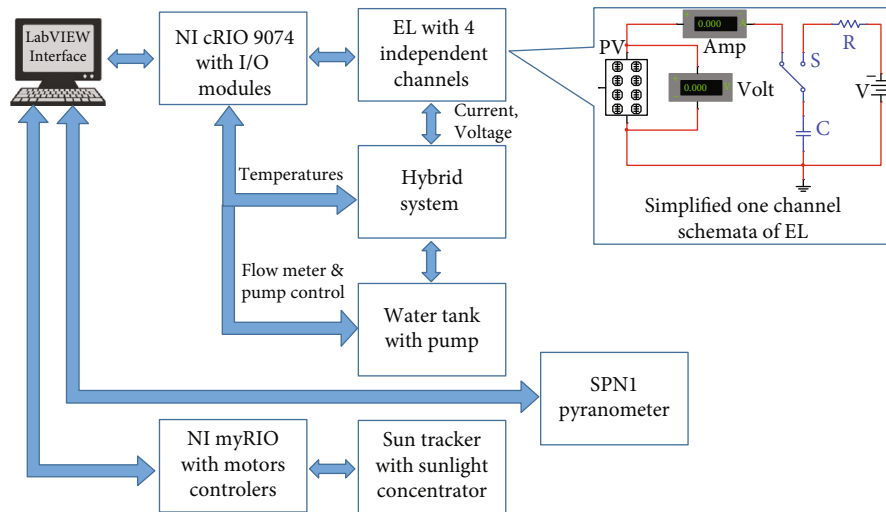
FIGURE 2: The system diagram.

and the TEG array (one channel). At the same time, all temperatures and the water flow are measured. The data for irradiance is obtained through the serial communication between PC and SPN1

(iii) All data are saved on the NI cRIO and PC HDDs, respectively

(iv) The system waits for a predefined measuring time, and then, the procedure is repeated, without initialization stage

All saved data are transferred to the PC and using a NI LabVIEW application are postprocessed and analysed.

3. Results and Discussions

The system was tested in natural conditions in the mountain city Brasov, Romania (lat: 45.648° and long: 25.606°), having 500 m altitude. The system was placed on the roof of our university building for assuring the free shadow and reflection area. During the tests, sunny and partial sunny climate
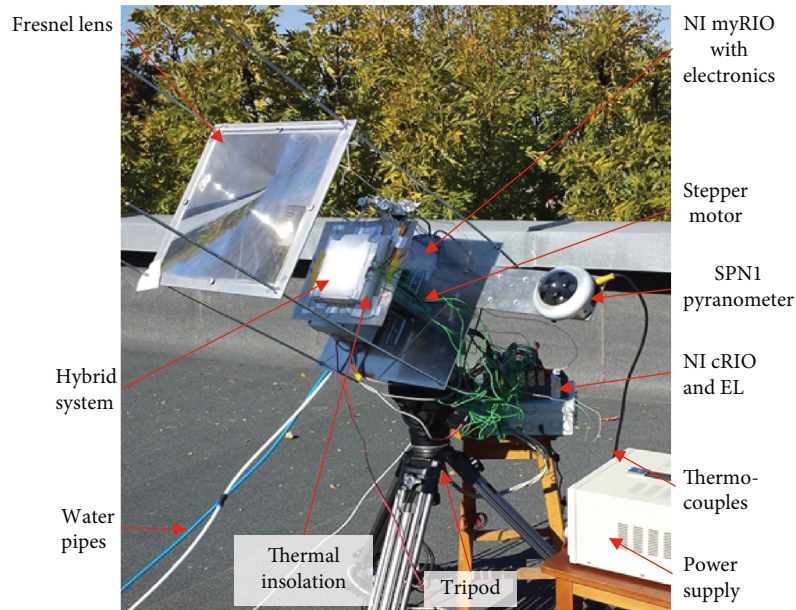
FIGURE 3: Experimental system.

conditions were present. The range of the irradiance level obtained with the developed system ranges from 5 to 56 suns on a $4\,cm \times 4\,cm$ area. The size of the illumination spot used for testing the system was $6\,cm \times 6\,cm$ for which the concentration ratio becomes 25 suns including the Fresnel lens optical efficiency. With this configuration, the uniformity of the CPV illumination is ensured.

The HS was covered with an alumina sheet for thermal protection, having three configurations:

(1) Only the active area of CPVs was kept uncovered (with alumina cross, WAC, Figure 5(a)). The exposed area is $4\,cm^2$. In this case, the thermal energy that can be used by TEG and STC is the difference between the total energy absorbed by the CPVs and the energy converted in electricity

(2) The CPV support area was exposed, which is $16\,cm^2$ (without alumina cross, WoAC, Figure 5(b)). In this case the usable thermal energy is increased by the support absorption

(3) The ceramic support of the CPVs was covered with a graphite sheet for better thermal absorption (with graphite sheet, WGS, Figure 5(c)). In this case, using the graphite sheet leads to the increasing of the thermal energy absorption by the system

The three configurations were selected in order to analyse the effect of the heat absorption on efficiency of each HS component. In the three surfaces having different heat absorption coefficients, the heat absorption is different so the working temperature of each component of HS will be modified. Due to the fact that thermal management of the system represents a very important factor in the overall efficiency of HS (CPV requires small temperature, while the TEG and STC require high temperature), using these three

cases, it was possible to study how the heat absorption affects the HS efficiency.

The water flow rate for tests through the STC was set at 0.4 L/min. The electric power and the efficiency of the CPVs and TEGs were determined based on the I-V characteristics. The efficiency of the STC was calculated based on the inlet and outlet water temperatures and the incident irradiance.

3.1. CPV Analysis. The CPV I-V characteristics in concentrated and nonconcentrated sunlight were measured using the NI cRIO platform and the self-designed EL. Figure 6 illustrates the I-V and P-V characteristics for one array of CPVs in concentrated (25 suns) and nonconcentrated sunlight (the current and power of the CPVs are multiply by 20 in Figure 6). In nonconcentrated sunlight (without Fresnel lens), the maximum power generated by one CPV array was 51 mW obtained at an irradiance of $1000\,W/m^2$.

The CPV efficiency is calculated according to the following equation:

$$\eta_{\mathrm{CPV}} = \frac{P_{\mathrm{CPV}}}{A_{\mathrm{CPV}} \cdot G} 100\%, \qquad (1)$$

where η_{CPV} is the CPV electrical efficiency, P_{CPV} is the electric power of the CPVs (W), A_{CPV} is the active area of CPVs (m^2), and G is the irradiance (W/m^2). Based on Equation (1), the CPV efficiency obtained was 25.5%, with $P_{\mathrm{CPV}} = 51\,mW$, $A_{\mathrm{CPV}} = 2\,cm^2$ (the area of one CPV array), and $G = 1000$ W/m^2.

Figure 7 shows the CPV electric power generated in concentrated sunlight of 25 suns. The average power of all four CPVs was around 3.1 W. The average temperature variation of all CPVs and the direct sun irradiance measured in the plan of HS are presented in Figures 8 and 9. One can observe that the maximum temperature of the CPVs was obtained using the WGS configuration, and it was around 52°C,
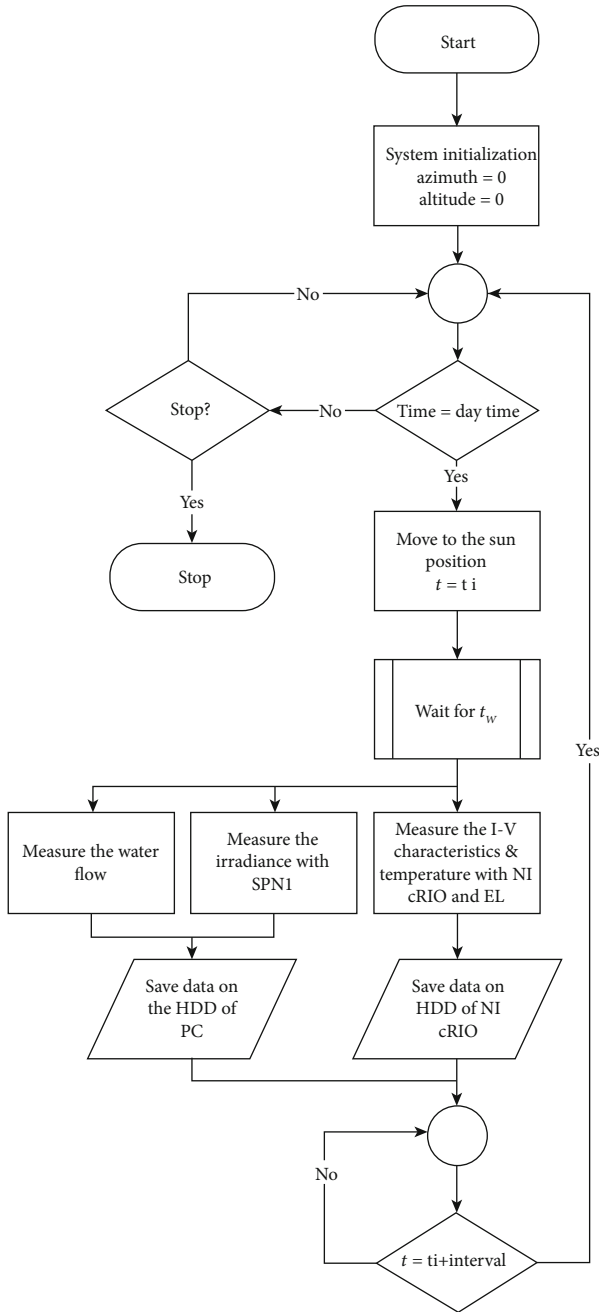
FIGURE 4: The flow chart of the system operation and measurement.

because of the heat absorption of the graphite sheet. In the case of the WAC configuration, the temperature of the CPVs is the smallest one, around 35°C, because of the alumina shield. The measurements were done during three days with almost the same irradiance in July.

The CPV efficiency under concentration is calculated based on Equation (1) taking into account the concentration ratio of the Fresnel lens [36]:

$$G^* = G \cdot C, \tag{2}$$

where G from Equation (1) is replaced by G^* which repre-

sents the modified solar radiation and C is the concentration ratio that includes the optical efficiency of the Fresnel lens ($\eta_{FL} = 83\%$) [18]. The average efficiencies obtained for CPVs based on Equations (1) and (2) were 32.3% for WAC, 31.4% for WoAC, and 30.8% for WGS.

One can observe in Figure 7 that the electric powers generated by the CPVs have decreased from WAC to WoAS and WGS configurations. This happened because their temperatures have increased (Figure 8).

For the WGS configuration, the concentration ratio was modified to 33 suns for the last part of the measurements and, as can be seen from Figure 7, the electric power of the CPVs increased to 4.06 W from 3.09 W (31.4%). At the same time, the temperature of the CPVs increased by 6°C (Figure 8).

3.2. TEG Analysis. The TEG I-V characteristics in concentrated sunlight were measured in the same manner as for CPVs using another available channel of the NI cRIO platform and the EL. In Figure 10, the I-V and P-V characteristics obtained for the TEG array are shown. The temperature difference between the TEG sides was 25°C, and the irradiance was 25 suns. Based on the I-V characteristic slope, the TEG resistance could be calculated (considering that the four used TEGs are connected in series) and the obtained value is 1.2 Ω which is comparable with the results obtained in [37]. At 25-sun concentration ratio, the maximum electric power obtained from the TEG was 120 mW in WGS configuration, having the temperature difference of 26°C. The electrical efficiency of the TEGs can be calculated using the following equation [38, 39]:

$$\eta_{TEG} = \frac{P_{max}}{G^{**} \cdot A_{TEG}} 100\%, \tag{3}$$

where η_{TEG} is the TEG's electrical efficiency, A_{TEG} is the TEG's array area, and $G^{**} = G^* C'$ is the irradiance for TEGs, where the concentration ratio includes also the CPV's electric conversion efficiency, $C' = C \cdot (1 - \eta_{CPV}/100)$. Even if the exposed surfaces have different reflectivity, for comparison we considered for all three cases the same active area of 16 cm^2, without considering the surface reflectivity. The electrical powers generated by the TEGs and the temperature differences between TEG sides in the three configurations are shown in Figures 11 and 12. The average efficiency obtained for 25-sun concentration ratio based on Equation (3) was 0.120% for WAC, 0.26% for WoAC, and 0.44% for WGS.

When the concentration ration was fixed at 33 suns, the maximum electric power generated by the TEG array was 170 mW at a temperature difference of 30.5°C. In this case, the TEG efficiency reached 0.45%.

3.3. STC Analysis. To characterize the STC, the water inlet and outlet temperatures and the water flow rate were measured. The difference between the two temperatures was calculated (Figure 13).

The average water temperature difference between the inlet and outlet of the STC at a 0.4 l/min water flow rate was 1°C for WAC, 1.5°C for WoAC, and 1.9°C for WGS.
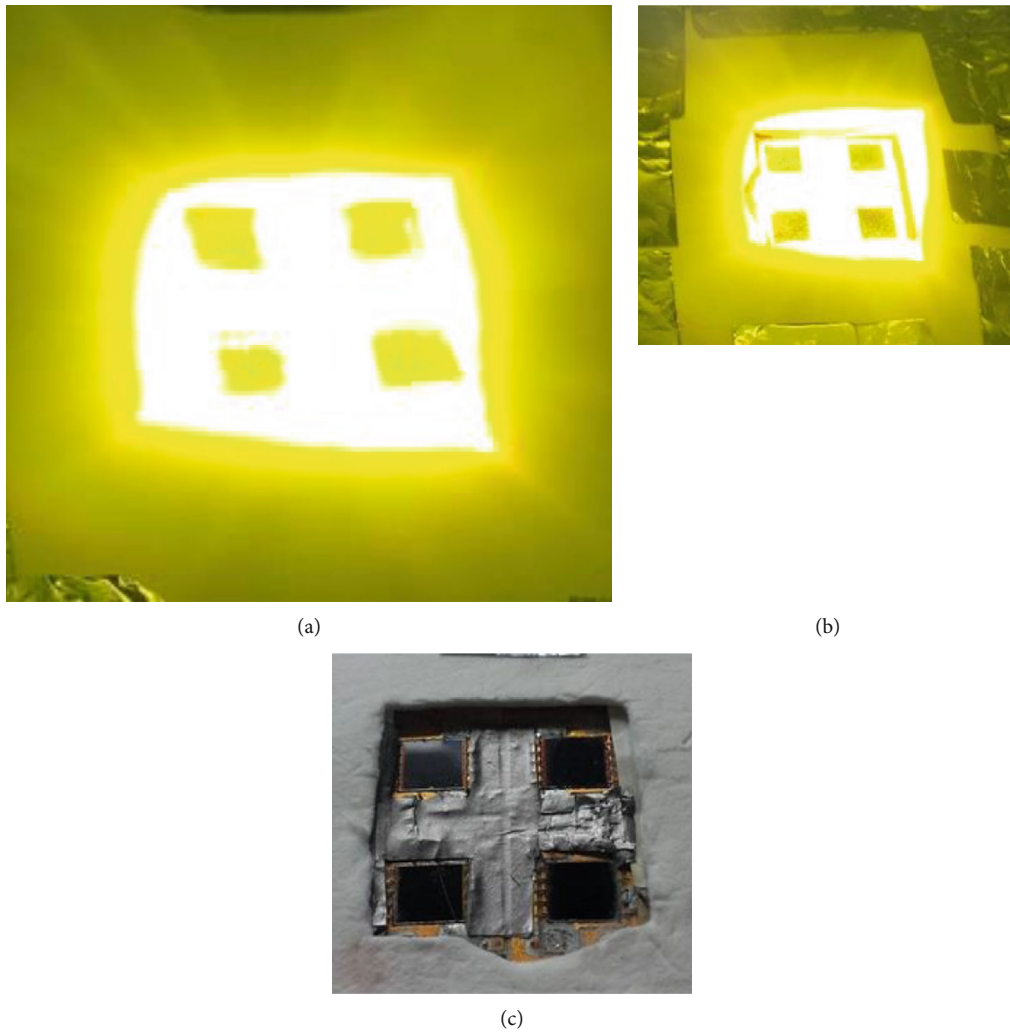
(a)

(b)

(c)

FIGURE 5: The tested configurations of HS: (a) with alumina cross; (b) without alumina cross; (c) with graphite sheet.
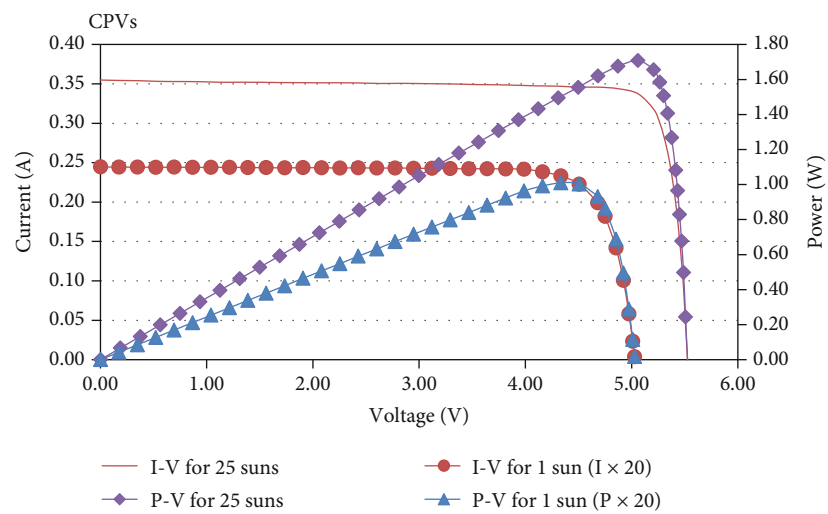

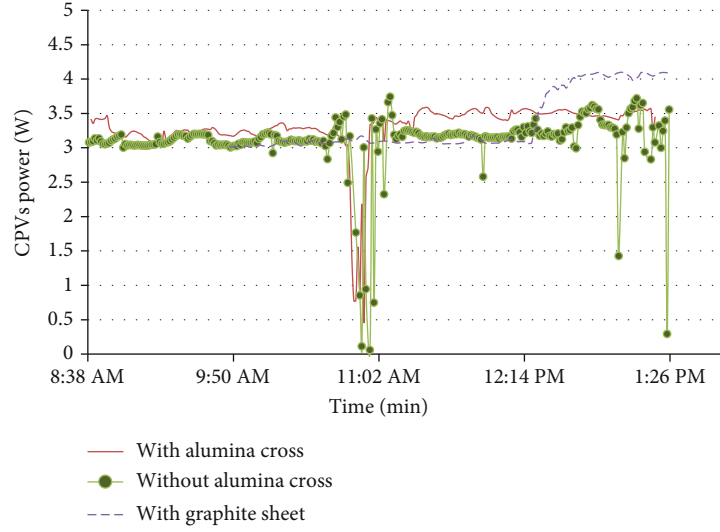FIGURE 6: The I-V and P-V characteristics in concentrated and nonconcentrated sunlight for CPVs.
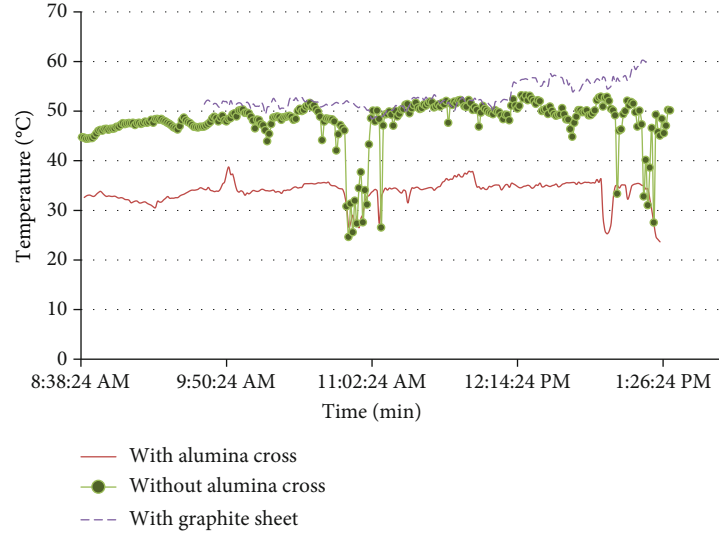
FIGURE 7: The CPV electric power.

FIGURE 8: The CPV temperature.

The thermal efficiency of the STC can be calculated based on the following equation [38]:

$$\eta_{STC} = \frac{\dot{Q}_W}{G^{***} \cdot A_{STC}} 100\%, \qquad (4)$$

where η_{STC} is the STC thermal efficiency, A_{STC} is the STC area, $G^{***} = G^* C''$ is the irradiance for STC, where the concentration ratio includes also the CPV's and TEG's electric conversion efficiencies, $C'' = C \cdot (1 - \eta_{CPV}/100 - \eta_{TEG}/100)$, and $\dot{Q}_W$ is the heat transfer rate that is calculated with the following equation:

$$\dot{Q}_W = \dot{m} c_P \Delta T, \qquad (5)$$

where $\dot{m}$ is the water flow-rate, c_p is the water specific heat capacity, and $\Delta T = T_{out} - T_{in}$ is the temperature difference between water outlet and inlet of the STC. Based on Equation (4), the STC efficiency was calculated for the three configurations: 26.3% for WAC, 35.7% for WoAC, and 52.0% for WGS.

For short periods of time, the water flow rate was modified in order to observe the effect in the STC efficiency (Figure 13 marked with red circles). At a 0.56 l/min water flow rate, the efficiency was 52.7%, and at 0.3 l/min, the efficiency dropped to 51.8%. This confirms that the water flow rate can have an important effect on the STC thermal efficiency [19]. Considering this setup in one hour, the temperature of 24 liters of water could be increased with ~2°C. If the system is multiplied by 5 times in 8 hours, 1 m³ of water could be heated increasing its temperature with ~2°C. This
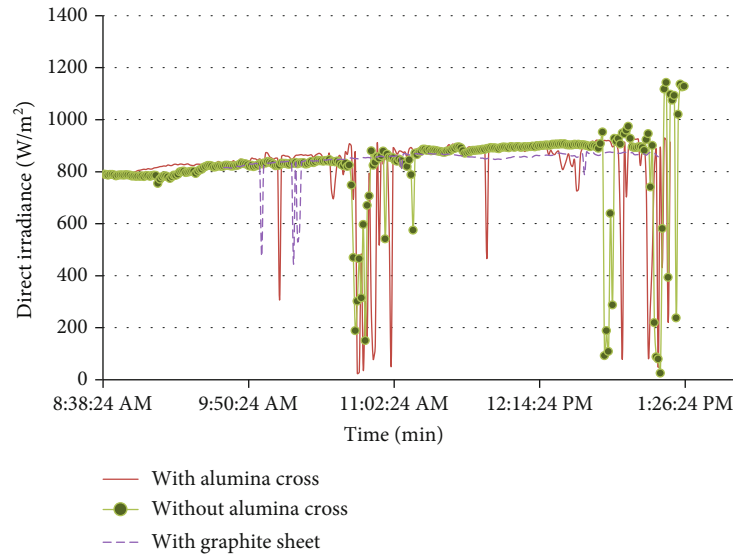
FIGURE 9: The direct sun irradiance during the HS study.
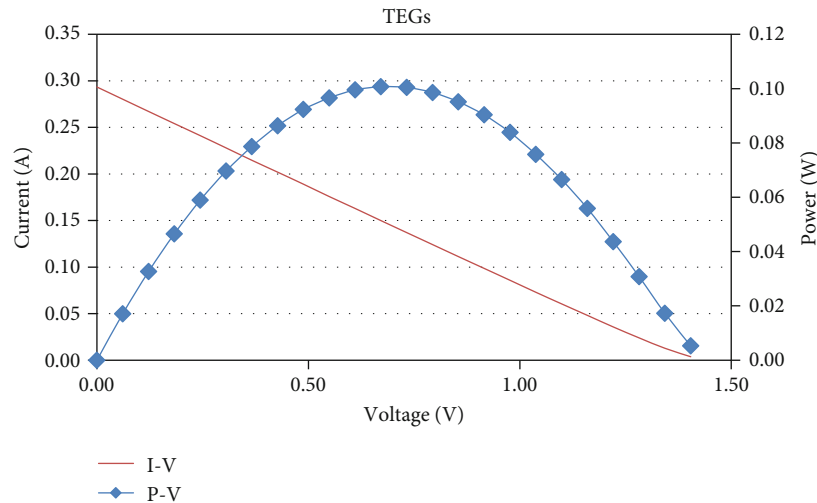

FIGURE 10: The I-V and P-V characteristics of TEGs in concentrated sunlight (25 suns, at $\Delta T = 25°C$).

indicates that using the HS with STC can be useful for increasing water temperature for a small swimming pool.

3.4. Discussions. The efficiency results analysed for CPVs, TEGs, and STC are shown in Table 2.

For the efficiency calculus of the HS components, C_{used} concentration ration was used due to the fact that the incident irradiance is absorbed by each component (CPVs and TEGs) and transferred to the next component minus what is converted into electricity. One can observe in Table 2 that the CPV efficiency has decreased from WAC to WoAS and to WGS configurations as a consequence of their temperatures' increase (Figure 8). This increase in temperature conducts to raising the efficiency of the TEGs and STC. In the WGS configuration, the CPV efficiency decreases once with the increase in concentration ratio. According to the used CPV datasheet [32], their efficiency should increase once with the concentration ratio (until 500 suns), but from Table 2,

one can observe that it decreases slowly. This can be explained by the increasing of their temperatures with 6°C, but also by the uniform breaking and chromatic aberration that increase when the illumination spot becomes equal to the system active area. In [40], it is shown that the fill factor of the CPVs and also their efficiency are affected by the chromatic aberration created by the Fresnel lens.

A CPV/TEG HS using a water cooled heat sink was studied in our previous paper [28]. The efficiency of the CPV shows a decreasing behaviour when the irradiance was increased. The efficiency variations reported in the paper are between 35.33% and 23.02% for an irradiance variation between 8 and 37 suns. The reported efficiency of the CPV at 25 suns is 27%. A similar CPV efficiency has been reported [30]. Comparing with the results obtained in this paper, it can be observed that there is ~5% difference. This can be explained through the spectrum used (in the cited paper, a solar simulator was used), but high influence in this
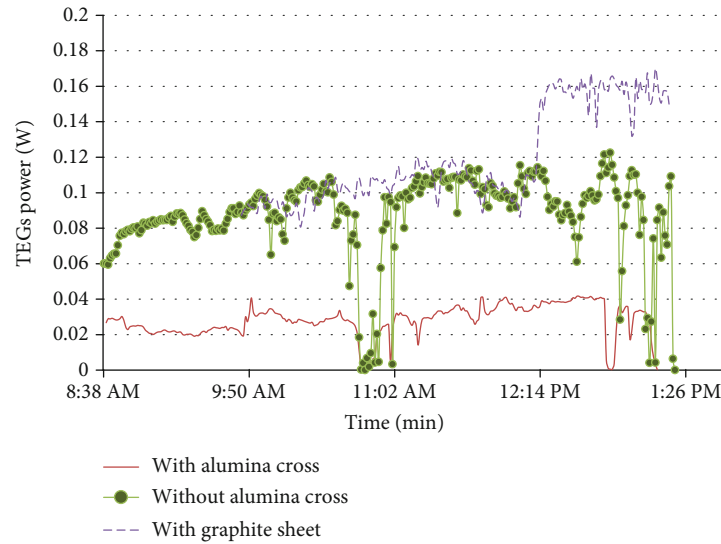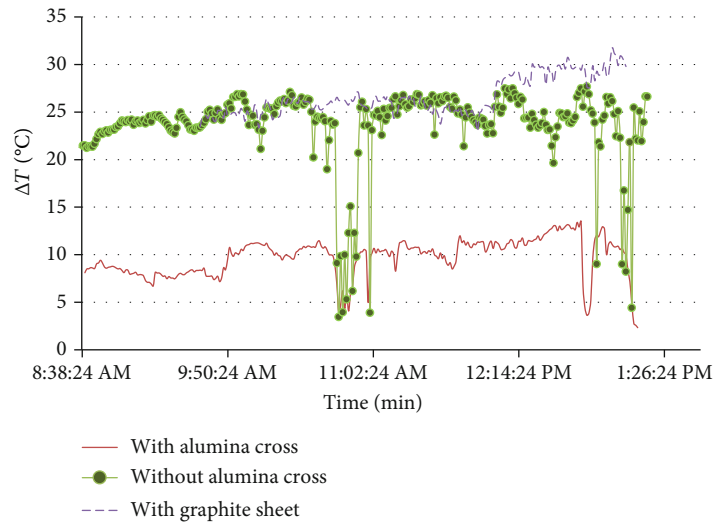
Figure 11: The TEG electric power.

Figure 12: The temperature differences between TEG sides.

difference is given by the temperature. In the cited paper, the reported CPV temperature overpasses 100°C, while in our case, the temperature is ~35°C for the first case and ~50°C for the last two cases. These differences are explained by the differences in testing conditions: irradiance spectrum (Xe lamps were used for solar simulator versus sunlight) and enclosed room versus free space.

The contribution of the TEG is small on the overall electrical energy generation, having a maximum power of 0.12 W in the WGS. The ratio of the average maximum powers generated by the TEG and CPV is shown in Figure 14. This ratio increases with the increase of absorbed heat and also with the solar concentration [28], starting from 0.9% up to 4%. The WGS2 is the WGS case with the concentration of 33 suns. Although the available commercial TEG efficiency is very small, a new TEG is reported in recent literature with an efficiency of 7.4% [41]. These high efficiencies of the proposed TEG are obtained at high temperature (around of 600°C).

At low temperature, the efficiency of the TEGs is smaller being in the range of 1-2%. In [42], it is shown that the efficiency for the TEGs with figure of merit, ZT = 2 at $\Delta T = 25$ °C, is around 2%. By using such TEGs, its contribution will significantly increase the overall efficiency of the HS. In our case, considering the WGS case, the TEG contribution will increase more than 4.5 times. This means that the power generated by the TEG could be around 540 mW, which represents 17% from the CPV total power generation.

By using the graphite sheet, it was shown that the performance of the TEG and STC increases, in the detriment of the CPV. In our setup, from a 16 cm^2 exposed surface, only 4 cm^2 are active. The CPVs are very good absorbers, and increasing their density on the exposed surface could increase the performance of the HS by increasing the electrical conversion of the CPV, but also due to more heat generated by CPVs and used by TEG and STC. A custom module or module like [43] could be used to increase the CPV density.
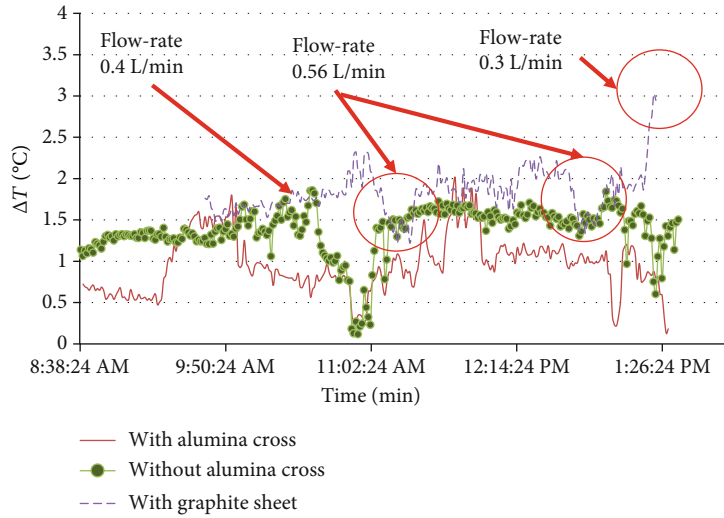
FIGURE 13: The variation of the temperature difference for STC.

TABLE 2: The efficiencies of the HS components in the three cases considered.

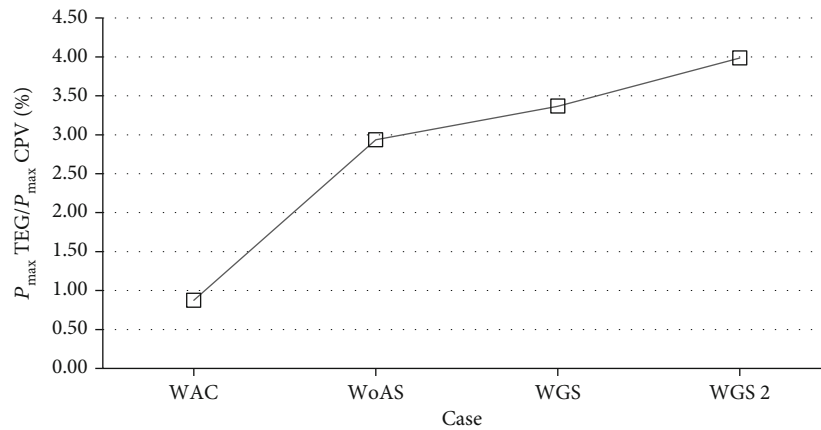| HS components	C (sun)	C_{used} (sun)	Efficiency (%)		
			WAS	WoAS	WGS
CPVs	25	C	32.32	31.37	30.81
	33		-	-	30.70
TEGs	25	$C' = C \cdot (1 - \eta_{CPV}/100)$	0.12	0.26	0.44
	33		-	-	0.45
STC	25	$C' = C \cdot (1 - \eta_{CPV}/100 - \eta_{TEG}/100)$	26.32	35.69	52.03
	33		-	-	54.21

FIGURE 14: Ratio between the maximum power of the TEG and CPV versus considered cases.

4. Conclusions

In this paper, a HS having a CPV/TEG/STC structure was studied at 25-sun concentration ratio. Three setups were considered for the exposed surface of the HS to the irradiance: the CPV active area, the support CPV area, and the support CPV area covered with a graphite layer. Based on this particular setup of the HS, the analysis of the effect of increasing the heat absorbance over the HS components was successfully done. It was noticed that due to the more heat absorbance in the three studied cases, the CPV efficiency decreases from 32.3% to 30.8%, while the efficiency of the TEGs increases from 0.12% to 0.44%, and for the STC, it increases from 26.3% to 52.0%. Using a heat absorbing material on the exposed area increased the electric and thermal power generated by the TEGs and STC, but decreased the electrical power generated by the CPVs.

Increasing the concentration ratio, the efficiency of the CPVs has shown a small decrease due to the increase of their temperature but the efficiency of the other two components,

TEGs and STC, showed a small increase. We found that the small flow rate variation of the water affects the efficiency of the STC.

Through this study, we showed that the exposed surface absorbance should be considered for HS design in order to have better overall efficiency. In the same time, the experiments in real working conditions should be performed to prove the HS performances. The advantage of hybrid systems is as follows: increased efficiency of the CPVs by a drop in their temperature and energy cogeneration (electrical by TEG and thermal by STC). These performances of the HS could be improved by using the TEGs with high performances and optimizing the surface reflectance of the CPV support surface.

Based on the three setups that were studied in this paper, it can be concluded that

(i) if the important part is electrical energy generation, then the first case should be used, due to the low temperature reached by the CPVs

(ii) if the thermal energy is also important, then the third case should be used in order to increase the STC efficiency. In this case, the electrical cogeneration of the TEG is increased to the detriment of the CPV generation. In this configuration, the thermal energy is increased and the proposed HS could be used as domestic system for heating the water of small swimming pool

Further works will be focused on studying the effect of increasing the density of the CPVs over the HS performances combined with concentration ratio variation and long-term monitor. The customization and the CPV density increase will strongly affect the costs for the HS. Therefore, the economic aspects represent another further study to be undertaken. Another direction of the further research is to find through simulations and experiments the optimal structure and dimensions for domestic applications, like water heating for a small swimming pool.

Data Availability

The datasets used in the present study are available from the corresponding author upon reasonable request.

Conflicts of Interest

The authors declare that there is no conflict of interest regarding the publication of this paper.

References

[1] M. A. Green, Y. Hishikawa, E. D. Dunlop et al., "Solar cell efficiency tables (version 53)," *Progress in Photovoltaics: Research and Applications*, vol. 27, no. 1, pp. 3–12, 2019.

[2] R. Santbergen and R. J. C. van Zolingen, "The absorption factor of crystalline silicon PV cells: a numerical and experimental study," *Solar Energy Materials & Solar Cells*, vol. 92, no. 4, pp. 432–444, 2008.

[3] J. Siecker, K. Kusakana, and B. P. Numbi, "A review of solar photovoltaic systems cooling technologies," *Renewable and Sustainable Energy Reviews*, vol. 79, pp. 192–203, 2017.

[4] D. T. Cotfas and P. A. Cotfas, "Multi concept methods to enhance photovoltaic systems efficiency," *International Journal of Photoenergy*, vol. 2019, 14 pages, 2019.

[5] K. A. Moharram, M. S. Abd-Elhady, H. A. Kandil, and H. El-Sherif, "Enhancing the performance of photovoltaic panels by water cooling," *Ain Shams Engineering Journal*, vol. 4, no. 4, pp. 869–877, 2013.

[6] A. A. Alzaabi, N. K. Badawiyeh, H. O. Hantoush, and A. K. Hamid, "Electrical/thermal performance of hybrid PV/T system in Sharjah, UAE," *International Journal of Smart Grid and Clean Energy*, vol. 3, pp. 385–389, 2014.

[7] C. Good, "Environmental impact assessments of hybrid photovoltaic-thermal (PV/T) systems," *Renewable and Sustainable Energy Reviews*, vol. 55, pp. 234–239, 2015.

[8] S. Mehrotra, P. Rawat, M. Debbarma, and K. Sudhakar, "Performance of a solar panel with water immersion cooling technique," *International Journal of Science, Environment and Technology*, vol. 3, pp. 1161–1172, 2014.

[9] R. Mazón-Hernández, J. R. García-Cascales, F. Vera-García, A. S. Káiser, and B. Zamora, "Improving the electrical parameters of a photovoltaic panel by means of an induced or forced air stream," *International Journal of Photoenergy*, vol. 2013, 10 pages, 2013.

[10] C. G. Popovici, S. V. Hudişteanu, T. D. Mateescu, and N.-C. Chereches, "Efficiency improvement of photovoltaic panels by using air cooled heat sinks," *Energy Procedia*, vol. 85, pp. 425–432, 2016.

[11] W. Pang, Y. Liu, S. Shao, and X. Gao, "Empirical study on thermal performance through separating impacts from a hybrid PV/TE system design integrating heat sink," *International Communications in Heat and Mass Transfer*, vol. 60, pp. 9–12, 2015.

[12] S. Nižetić, I. Marinić-Kragić, F. Grubišić-Čabo, A. M. Papadopoulos, and G. Xie, "Analysis of novel passive cooling strategies for free-standing silicon photovoltaic panels," *Journal of Thermal Analysis and Calorimetry*, vol. 141, no. 1, pp. 163–175, 2020.

[13] F. G. Čabo, S. Nižetić, E. Giama, and A. Papadopoulos, "Techno-economic and environmental evaluation of passive cooled photovoltaic systems in Mediterranean climate conditions," *Applied Thermal Engineering*, vol. 169, article 114947, 2020.

[14] D. T. Cotfas, P. A. Cotfas, D. Ciobanu, and O. M. Machidon, "Characterization of photovoltaic–thermoelectric–solar collector hybrid systems in natural sunlight conditions," *Journal of Energy Engineering*, vol. 143, no. 6, article 04017055, 2017.

[15] G. Li, X. Chen, and Y. Jin, "Analysis of the primary constraint conditions of an efficient photovoltaic-thermoelectric hybrid system," *Energies*, vol. 10, no. 1, p. 20, 2017.

[16] A. Rezania and L. A. Rosendahl, "Feasibility and parametric evaluation of hybrid concentrated photovoltaic-thermoelectric system," *Applied Energy*, vol. 187, pp. 380–389, 2017.

[17] T. H. Kil, S. Kim, D. H. Jeong et al., "A highly-efficient, concentrating-photovoltaic/thermoelectric hybrid generator," *Nano Energy*, vol. 37, pp. 242–247, 2017.

[18] T. Liao, B. Lin, and Z. Yang, "Performance characteristics of a low concentrated photovoltaic-thermoelectric hybrid power

generation device," *International Journal of Thermal Sciences*, vol. 77, pp. 158–164, 2014.

[19] F. Saeedi, F. Sarhaddi, and A. Behzadmehr, "Optimization of a PV/T (photovoltaic/thermal) active solar still," *Energy*, vol. 87, pp. 142–152, 2015.

[20] M. George, A. K. Pandey, N. A. Rahim, V. V. Tyagi, S. Shahabuddin, and R. Saidur, "Concentrated photovoltaic thermal systems: a component-by-component view on the developments in the design, heat transfer medium and applications," *Energy Conversion and Management*, vol. 186, pp. 15–41, 2019.

[21] W. T. Xie, Y. J. Dai, R. Z. Wang, and K. Sumathy, "Concentrated solar energy applications using Fresnel lenses: a review," *Renewable and Sustainable Energy Reviews*, vol. 15, no. 6, pp. 2588–2606, 2011.

[22] M. Tian, Y. Su, H. Zheng, G. Pei, G. Li, and S. Riffat, "A review on the recent research progress in the compound parabolic concentrator (CPC) for solar energy applications," *Renewable and Sustainable Energy Reviews*, vol. 82, pp. 1272–1296, 2018.

[23] X. Ju, C. Xu, X. Han, X. Du, G. Wei, and Y. Yang, "A review of the concentrated photovoltaic/thermal (CPVT) hybrid solar systems based on the spectral beam splitting technology," *Applied Energy*, vol. 187, pp. 534–563, 2017.

[24] F. Yazdanifard, E. Ebrahimnia-Bajestan, and M. Ameri, "Performance of a parabolic trough concentrating photovoltaic/thermal system: effects of flow regime, design parameters, and using nanofluids," *Energy Conversion and Management*, vol. 148, pp. 1265–1277, 2017.

[25] A. Riahi, A. B. H. Ali, A. Fadhel, A. Guizani, and M. Balghouthi, "Performance investigation of a concentrating photovoltaic thermal hybrid solar system combined with thermoelectric generators," *Energy Conversion and Management*, vol. 205, article 112377, 2020.

[26] S. Mahmoudinezhad, S. A. Atouei, P. A. Cotfas, D. T. Cotfas, L. A. Rosendahl, and A. Rezania, "Experimental and numerical study on the transient behavior of multi-junction solar cell-thermoelectric generator hybrid system," *Energy Conversion and Management*, vol. 184, pp. 448–455, 2019.

[27] A. Mohammadnia, A. Rezania, B. M. Ziapour, F. Sedaghati, and L. Rosendahl, "Hybrid energy harvesting system to maximize power generation from solar energy," *Energy Conversion and Management*, vol. 205, p. 112352, 2020.

[28] S. Mahmoudinezhad, A. Rezania, D. T. Cotfas, P. A. Cotfas, and L. A. Rosendahl, "Experimental and numerical investigation of hybrid concentrated photovoltaic - Thermoelectric module under low solar concentration," *Energy*, vol. 159, pp. 1123–1131, 2018.

[29] D. Yang and H. Yin, "Energy conversion efficiency of a novel hybrid solar system for photovoltaic, thermoelectric, and heat utilization," *IEEE Transactions on Energy Conversion*, vol. 26, no. 2, pp. 662–670, 2011.

[30] D. T. Cotfas, P. A. Cotfas, L. Floroian, and D. I. Floroian, "Study of combined photovoltaic cell/thermoelectric element/-solar collector in medium concentrated light," in *2017 International Conference on Optimization of Electrical and Electronic Equipment (OPTIM) & 2017 Intl Aegean Conference on Electrical Machines and Power Electronics (ACEMP)*, pp. 747–752, Brasov, Romania, 2017.

[31] P. Pérez-Higueras, E. Muñoz, G. Almonacid, and P. G. Vidal, "High Concentrator PhotoVoltaics efficiencies: Present status and forecast," *Renewable and Sustainable Energy Reviews*, vol. 15, no. 4, pp. 1810–1815, 2011.

[32] 2020, https://solaerotech.com/wp-content/uploads/2018/03/CTJ-Datasheet.pdf.

[33] 2020, https://www.tme.eu/Document/f90b783c096cf8ceee627b2a275a42d4/pm-40x40-89.pdf.

[34] M. Victoria, S. Askins, R. Herrero et al., "Measuring primary lens efficiency: a proposal for standardization," in *12th International Conference on Concentrator Photovoltaic Systems (CPV-12)*, p. 120001, Freiburg, Germany, 2016.

[35] P. A. Cotfas, D. T. Cotfas, C. Gerigan, and O. M. Machidon, "System design to study hybrid systems in concentrated light using Fresnel lens," in *2017 International Conference on Optimization of Electrical and Electronic Equipment (OPTIM) & 2017 Intl Aegean Conference on Electrical Machines and Power Electronics (ACEMP)*, pp. 753–758, Brasov, Romania, 2017.

[36] F. Karimi, H. Xu, Z. Wang, J. Chen, and M. Yang, "Experimental study of a concentrated PV/T system using linear Fresnel lens," *Energy*, vol. 123, pp. 402–412, 2017.

[37] H. Terzioglu, "Analysis of effect factors on thermoelectric generator using Taguchi method," *Measurement*, vol. 149, p. 106992, 2020.

[38] M. H. Nia, A. A. Nejad, A. M. Goudarzi, M. Valizadeh, and P. Samadian, "Cogeneration solar system using thermoelectric module and Fresnel lens," *Energy Conversion and Management*, vol. 84, pp. 305–310, 2014.

[39] M. H. Shareef, A. Sajid, A. A. Majeed, and M. A. B. Adnan, "Efficiency calculation of a thermoelectric generator," *International Journal of Science and Research*, vol. 5, no. 7, pp. 1520–1522, 2016.

[40] M. Steiner, G. Siefer, T. Schmidt, M. Wiesenfarth, F. Dimroth, and A. W. Bett, "43% sunlight to electricity conversion efficiency using CPV," *IEEE Journal of Photovoltaics*, vol. 6, no. 4, pp. 1020–1024, 2016.

[41] D. Kraemer, Q. Jie, K. McEnaney et al., "Concentrating solar thermoelectric generators with a peak efficiency of 7.4%," *Nature Energy*, vol. 1, no. 11, article 16153, 2016.

[42] D. Champier, "Thermoelectric generators: a review of applications," *Energy Conversion and Management*, vol. 140, pp. 167–181, 2017.

[43] 2020, http://www.azurspace.com/index.php/en/products/products-cpv/cpv-dense-array-module.

Research Article

Calculation of Seven Photovoltaic Cells Parameters Using Parallelized Successive Discretization Algorithm

Adrian M. Deaconu [1], **Daniel T. Cotfas** [2], **and Petru A. Cotfas** [2]

[1]*Faculty of Mathematics and Computer Science, Transilvania University of Brasov, Braşov, Romania*
[2]*Faculty of Electrical Engineering and Computer Science, Transilvania University of Brasov, Braşov, Romania*

Correspondence should be addressed to Adrian M. Deaconu; a.deaconu@unitbv.ro

Some parameters must be calculated with very good accuracy for the purpose of designing, simulating, and evaluating the performance of a photovoltaic system. The seven parameters of the photovoltaic cell and panels for the two-diode model are determined using a parallelized metaheuristic algorithm based on successive discretization. The parameters obtained for a photovoltaic cell and four panels using the proposed algorithm are compared with the ones calculated through over twenty methods from recent research literature. The root mean square error is used to prove the superiority of the Parallelized Successive Discretization Algorithm (PSDA). The smallest values for root mean square error (RMSE) in both cases, photovoltaic cell and panels, are obtained for the algorithm presented in this paper. The seven parameters for three panels known in the specialised literature, Kyocera KC200GT, Leibold Solar Module LSM 20, and Leybold Solar Module STE 4/100 are determined for the first time using PSDA.

1. Introduction

Fossil fuel is inevitable exhausting, and its price has continually increased in the last decades. There is also an increasing concern on the environmental pollution and on the climate changes related to the use of fossil fuel. It is strongly believed that the renewable energy is the clean alternative solution of today and for the future. Many researchers have focused on renewable solar energy in general and, in particular, on the generation of electric power using photovoltaic cells which is desired to become in the near future one of the most important energy sources.

Nowadays, there are many photovoltaic cells types, some of them relatively new, such as Perovskite or multijunctions—triple or four junctions, which must be analyzed and characterized to optimize their efficiency. Very good photovoltaic panels are achieved if the photovoltaic cells used are "twins." This can be realized if the photovoltaic cells are characterized before the fabrication process of the photovoltaic panels, and they are selected so that the parameters have the same values.

The characterization process must be very fast so as to increase the productivity.

Some parameters must be calculated with very good precision for the purpose of designing, simulation, and evaluation of the performance of a photovoltaic system. Nowadays, the estimation of these parameters is an important research topic, for which researchers develop new methods and algorithms. The parameters of the photovoltaic cells and panels can be determined using the current voltage characteristic, called I-V characteristic in the following, equivalent circuit, and the mathematical model [1, 2]. The one-diode model is generally used to determine the parameters of the photovoltaic cells, due to the simplicity and good agreement for the parameters results [3]. Lately, the researchers are using the two-diode model to determine the photovoltaic cells parameters, especially for the monocrystalline and polycrystalline silicon photovoltaic cells and panels. In this case, both mechanisms, the diffusion and the generation and recombination, are taken into account. Using the two-diode model leads to growth accuracy with which the parameters of the photovoltaic cells are determined.

The parameters of the photovoltaic cells and panels were determined using graphical analysis and numerical analysis with different approximation [1]. The metaheuristic algorithms based on natural phenomena were used lately with success because are suitable for nonlinear multimodal as is the problem for photovoltaic devices. The parameters of the photovoltaic cells and panels using the metaheuristic algorithms are calculated with high accuracy due to avoiding the errors made through approximation in the other methods, and the necessary time for their determination is reduced continuously due to the optimization of the algorithms and use of the hybrid algorithms [3].

We shall briefly present below the best currently known algorithms for determining the solar cell parameters. They are taken into consideration to compare their performance against the Parallelized Successive Discretization Algorithm (PSDA) presented in this paper. Most of these algorithms are metaheuristic methods inspired from the behavior of populations of different groups of people or from the behavior of swarms of animals or insects. Population classification evolution algorithm (PCE) is an evolutional algorithm, with a fast convergence speed and a very good accuracy [4]. Simplified TBLO (STBLO) [5] and generalized oppositional TBLO (GOTBLO) [6] are improved versions of teaching-learning-based optimization (TLBO) algorithm which is a population-based method. Improved shuffled complex evolution (ISCE) is an improved version of complex evolution strategy (SCE) which was applied with success to calculate the parameters of one-diode and two-diode models for photovoltaic cell and for panel [7]. Rcr-IJADE has better performance than other classic or adaptive differential evolution algorithms [8]. MABC is a modified version of artificial bee colony (ABC) algorithm with better results than the regular ABC [9]. EHA-NMS and NM-MPSO are hybrid algorithms and are based on Nelder–Mead and MABC [10] and, respectively, particle swarm optimization PSO [9]. Cat swarm optimization algorithm (CSO) is developed by analyzing the behaviors of cats. The performance of CSO surpasses that of PSO [11]. Bird mating optimizer (BMO) tries to imitate the mating strategies of bird species, without premature convergence, and thus, its solution is close to the global one [12]. Chaotic whale optimization algorithm (CWOA) is an algorithm developed on the hunting mechanism of humpback whales, and it can refine complex and multimodal objective functions [13]. Artificial bee swarm optimization algorithm (ABSO) is based on the intelligent behaviors of honey bees such as collection and processing of nectar [12]. Innovative global harmony search (IGHS) and grouping-based global harmony search (GGHS) algorithms are improved versions of the harmony search algorithm trying to imitate the improvisation process of musicians [14]. Simulated annealing (SA) is a single-searcher algorithm with less chance to find the global minimum [15]. Guaranteed convergence particle swarm optimization (GCPSO) [16] is an improved version of the PSO algorithm, and it has the ability to avoid premature convergence and to determine the parameters of the photovoltaic panels quickly and accurately. Time-varying acceleration coefficients particle swarm optimization (TVACPSO) is an improved PSO. WDOWOAPSO is a hybrid method based on PSO and the wind-driven optimization (WDO) technique [17]. Artificial Bee Colony-Differential Evolution (ABC-DE) resulted from ABC, and its performance is improved for finding the global optimum and for convergence speed [18]. Flexible particle swarm optimization (FPSO) improves the PSO algorithm through increasing the ability of global search [19].

In this paper, a metaheuristic algorithm based on the discretization process of functions that systematically try to improve the approximate solution is presented. Discretization is defined in Mathematics as the continuous functions, variables, models, and equations transferred into discrete counterparts. It usually represents the first stage of achieving proper values for numerical evaluation or implementation on digital computers. Such techniques are implemented in order to solve miscellaneous problems [20], among the optimizing ones [21]. If continuous data is discretized, discretization error appears in various amounts. The aim is decreasing the errors down to a negligible value in terms of modeling scope.

The idea of successive discretization algorithm (SDA) applied for parameter estimation of PV cells is to compute a set of approximate solutions selected from values obtained by a discretization process and having the minimum root mean square error. Around each of these selected values, a more refined discretization is performed and a new set of approximate solutions is selected and so on. The successive discretization process performed a preset number of iterations or until no better solution is found than the best solution found so far in the previous iteration.

In this paper, we adapt and implement SDA in parallel for the two-diode model, and we compare the obtained solution with the solutions given by the best known methods at the moment. The novelty and the contributions of the paper are

(i) the new algorithm PSDA is presented in the paper

(ii) the results obtained for the RMSE for all devices under analysis are the best in comparison with the other algorithms from the specialised literature

(iii) the time needed to extract the parameters of the photovoltaic cell and panels for the two-diode model increases, and the PSDA algorithm is the proper tool to reduce it; the duration is reduced 6 times using the PSDA in comparison with SDA algorithm

(iv) three datasets are analyzed for the first time using the two-diode model: Kyocera KC200GT, Leibold Solar Module LSM 20, and Leybold Solar Module STE 4/100.

2. Method

2.1. Models for Photovoltaic Cell and Panel.
The equivalent circuit of the photovoltaic panel is presented in Figure 1, and the mathematical model is given by Eq. (1). The following seven parameters can be determined: the photogenerated current I_{ph}, the reverse saturation current I_{od} and ideality factor of diode n_d which correspond to diffusion mechanism,
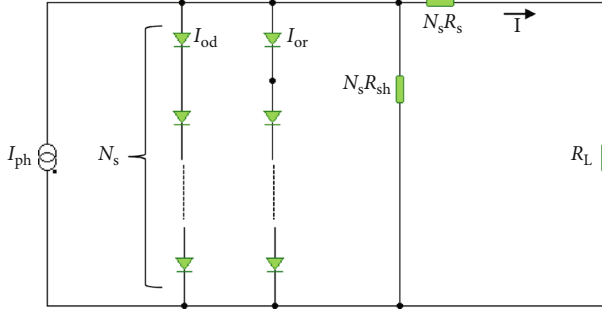
FIGURE 1: Equivalent circuits of photovoltaic panel. Two-diode model.

the reverse saturation current I_{or} and ideality factor of diode n_r which correspond to generation and recombination mechanism, and the parasitic resistance–series resistance R_s and shunt resistance R_{sh} [1]. N_s is the number of the photovoltaic cells connected in series. N_s is one in case of the photovoltaic cell.

$$I = I_{ph} - I_{od}\left(e^{\frac{V+IN_sR_s}{n_dN_sV_T}} - 1\right) - I_{or}\left(e^{\frac{V+IN_sR_s}{n_rN_sV_T}} - 1\right) - \frac{V + IN_sR_s}{N_sR_{sh}} \quad (1)$$

2.2. Parallelized Successive Discretization Algorithm.

SDA algorithm was successfully applied for the one-diode model in [3]. It was compared with other methods used to determine the parameters of the photovoltaic cells and panels. SDA proved to be the best among the known methods at the moment the article was published. In this paper, we adapt SDA to solve the more complex problem of estimating the seven parameters for the two-diode model. Since the amount of calculations is considerably higher than for the one-diode model, a direct adaptation of SDA for the two-diode model leads to a very slow algorithm or to an algorithm that finds a low-quality solution. Therefore, a parallel implementation of SDA is needed, fast enough and able to compute very good solutions. In the production process of photovoltaic panels, it is very important to accurately and quickly estimate the cell parameters.

2.2.1. Discretization Process.

The PSDA algorithm is based on discretization, which transfers continuous functions and equations into discrete counterparts. When the continuous data are discretized, some errors can appear, and the target is to reduce them [3].

We denote by

$$F_{I,V}^2\left(I_{ph}, I_{od}, n_d, I_{or}, n_r, R_s, R_{sh}\right) = I_{ph} - I_{od}\left(e^{\frac{V+IR_s}{n_dV_T}} - 1\right)$$
$$- I_{or}\left(e^{\frac{V+IR_s}{nV_T}} - 1\right) \quad (2)$$
$$- \frac{V + IR_s}{R_{sh}} - I.$$

Using Equations (1) and (2), the following equation is obtained:

$$F_{I,V}^2\left(I_{ph}, I_{od}, n_d, I_{or}, n_r, R_s, R_{sh}\right) = 0. \quad (3)$$

The root mean square error (RMSE), given by Equation (4), has to be minimized for the photovoltaic cell and panel parameters, I_{pH}, I_{od}, n_d, I_{or}, n_r, R_s, and R_{sh} calculated for the given pairs of current and voltage (I, V).

$$\mathrm{RMSE}\left(I_{ph}, I_{od}, n_d, I_{or}, n_r, R_s, R_{sh}\right) = \sqrt{\frac{\sum\left(F_{I,V}^2\left(I_{ph}, I_{od}, n_d, I_{or}, n_r, R_s, R_{sh}\right)\right)^2}{p}}, \quad (4)$$

where p represents the number of the given (I, V) pairs.

The intervals $J_i = [a_i, b_i]$ $(i = 1, 2, \cdots, 7)$ are considered for the definition of domains for the seven parameters enumerated before.

The function $F_{I,V}^2$ is continuous on the 7-dimensional interval $J_1 \times J_2 \times J_3 \times J_4 \times J_5 \times J_6 \times J_7$, which is called the discretization 7D interval. The discretization process is applied to the objective function $F_{I,V}^2$. The solution is searched in $J_1 \times J_2 \times J_3 \times J_4 \times J_5 \times J_6 \times J_7$. This 7D interval is the given boundaries for the searched solutions.

For each interval J_i, a positive integer $d_i \in N^*$ is considered $(i = 1, 2, \cdots, 7)$. Inside each of these 7 intervals, the values v_j^i $(j = 1, \cdots, d_i)$ are taken so that

$$a_i < v_1^i < v_2^i < \cdots < v_{d_i}^i < b_i. \quad (5)$$

The values v_j^i $(j = 1, \cdots, d_i)$ are calculated using Equation (6) in order to obtain a good uniform distribution of the points in the interval J_i:

$$v_j^i = a_i + jl_i, \quad (6)$$

where l_i is calculated using the following relation:

$$l_i = \frac{b_i - a_i}{d_i + 1}. \quad (7)$$

Using Equations (6) and (7), the following relations are obtained:

$$v_1^i = a_i + l_i \text{ and } v_{d_i}^i = b_i - l_i. \quad (8)$$

For the photovoltaic cell or panel, the following set of septets of parameters is considered:

$$G = \left\{ \left(v_{j_1}^1, v_{j_2}^2, v_{j_3}^3, v_{j_4}^4, v_{j_5}^5, v_{j_6}^6, v_{j_7}^7\right) \mid j_i = 1, \cdots, d_i, i = 1, \cdots, 7 \right\}. \quad (9)$$

PSDA calculates $\left(v_{k_1}^1, v_{k_2}^2, v_{k_3}^3, v_{k_4}^4, v_{k_5}^5, v_{k_6}^6, v_{k_7}^7\right)$ so that

$$\mathrm{RMSE}\left(v_{k_1}^1, v_{k_2}^2, v_{k_3}^3, v_{k_4}^4, v_{k_5}^5, v_{k_6}^6, v_{k_7}^7\right) = \min_{g \in G}\mathrm{RMSE}(g). \quad (10)$$

The septet $\left(v_{k_1}^1, v_{k_2}^2, v_{k_3}^3, v_{k_4}^4, v_{k_5}^5, v_{k_6}^6, v_{k_7}^7\right)$ is an approximate solution of Equation (3).
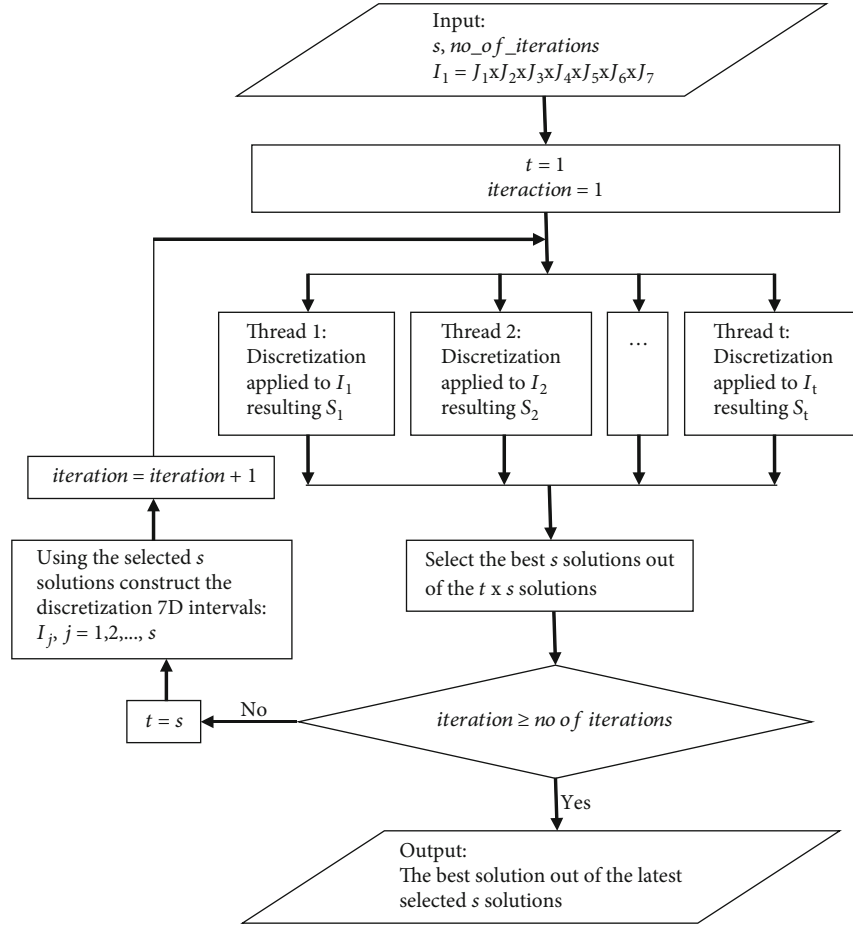
Figure 2: Flowchart of the parallel implementation of the algorithm.

Table 1: The seven parameters of the RTC photovoltaic cell.

| Algorithm	I_{ph} A	I_{od} μA	I_{or} μA	n_d	n_r	R_s Ω	R_{sh} Ω	RMSE E-04
PSDA	0.76077943	0.22615047	0.74934181	1.4510581	2.00119185	0.03674321	55.48427327	9.82473
PCE [4]	0.760781	0.226015	0.749340	1.450923	2.000000	0.03674	55.483160	9.8248
STLBO [5]	0.76078	0.22566	0.75217	1.45085	2.00000	0.03674	55.4920	9.8248
ISCE [7]	0.76078108	0.22597409	0.74934898	1.4510167	2.000000	0.03674043	55.48544409	9.82484
Rcr-IJADE [8]	0.76078108	0.22597414	0.74934851	1.45101670	2.000000	0.03674043	55.48543800	9.824849
EHA-NMS [10]	0.76078108	0.22597420	0.74934836	1.45101674	2.000000	0.03674043	55.48544722	9.824849
NM-MPSO [10]	0.76078	0.22476	0.75524	1.45054	1.99998	0.03675	55.5296	9.825
CSO [11]	0.76078	0.22732	0.72785	1.45151	1.99769	0.036737	55.3813	9.8252
FPSO [19]	0.76078	0.22731	0.72786	1.45160	1.99969	0.036737	55.3923	9.8253
BMO [12]	0.76078	0.21110	0.87688	1.44533	1.99997	0.03682	55.8081	9.8262
CWOA [13]	0.76077	0.24150	0.60000	1.45651	1.9899	0.03666	55.2016	9.8272
MABC [9]	0.7607821	0.24102992	0.6306922	1.4568573	2.0000538	0.03671215	54.7550094	9.8276
GOTLBO [6]	0.760752	0.220462	0.800195	1.448974	1.999973	0.036783	56.075304	9.83177
ABSO [12]	0.76078	0.26713	0.38191	1.46512	1.98152 4	0.03657	54.6219	9.834
ICHS [14]	0.76079	0.16791	0.97310	1.42814	1.92126	0.03690	56.8368	9.8635
GGHS [14]	0.76056	0.37014	0.13504	1.49638	1.92998	0.03562	62.7899	10.684
SA [15]	0.7623	0.4767	0.01	1.5172	2	0.0345	43.1034	166.4
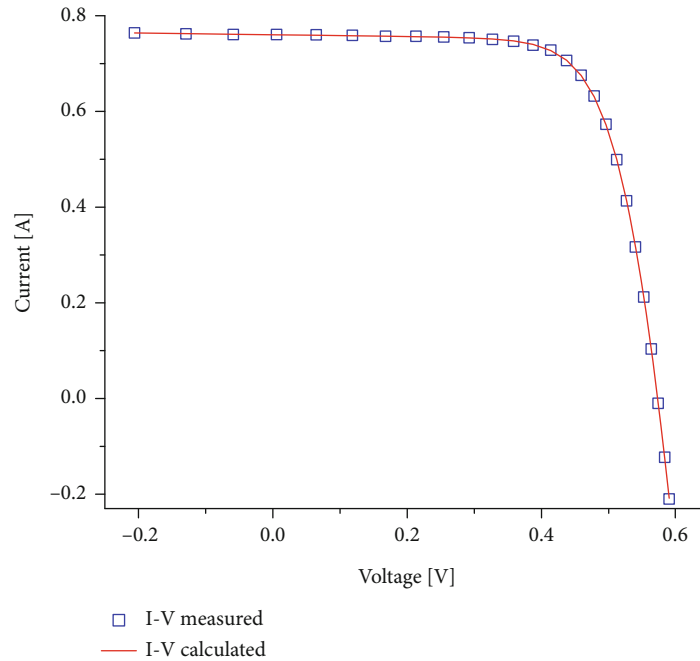
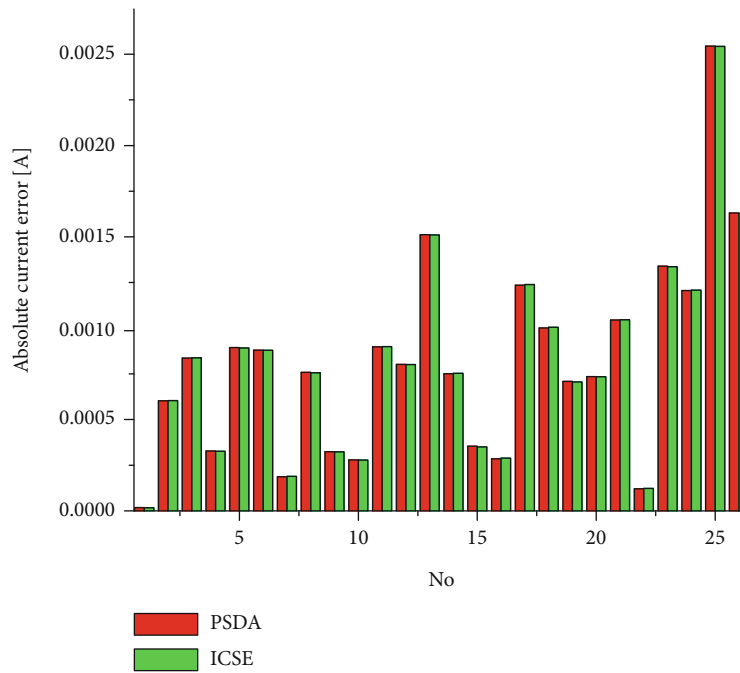FIGURE 3: The I-V characteristics for RTC photovoltaic.

FIGURE 4: Absolute current error comparison for RTC.

2.2.2. Improving the Solution by Successive Discretization.

The best approximate solution for Equation (3) can be improved using a successive discretization–refining initial solution.

The best $s \geq 1$ ("s" is established at the beginning of the algorithm) septets are considered $g_j = (v^1_{k^j_1}, v^2_{k^j_2}, v^3_{k^j_3}, v^4_{k^j_4}, v^5_{k^j_5}, v^6_{k^j_6}, v^7_{k^j_7})$ $(j = 1, \cdots, s)$ in the set G, having the smallest RMSE errors (Cotfas D.T., [3]). For each septet g_j, the

solutions are refined for Equation (3) in the neighborhood of g_j:

$$J^j_1 \times J^j_2 \times J^j_3 \times J^j_4 \times J^j_5 \times J^j_6 \times J^j_7, \tag{11}$$

where

$$J^j_i = \left[v^i_{k^j_i} - l_i, v^i_{k^j_i} + l_i \right], i = 1, \cdots, 7. \tag{12}$$
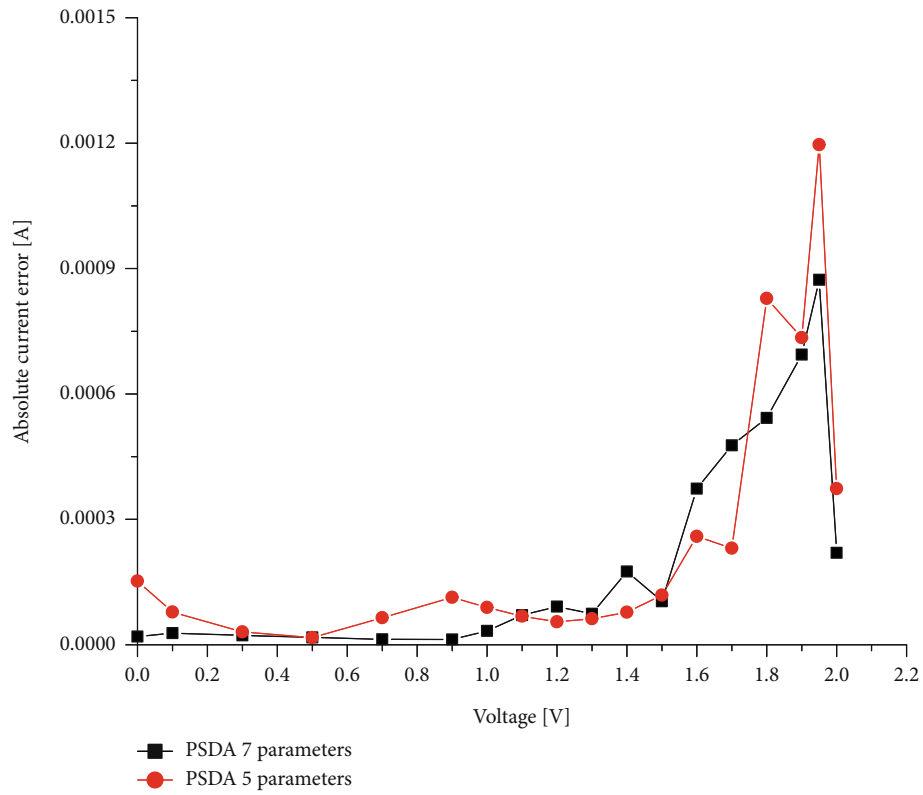
Figure 5: Comparison between the two-diode and one-diode model for RTC.
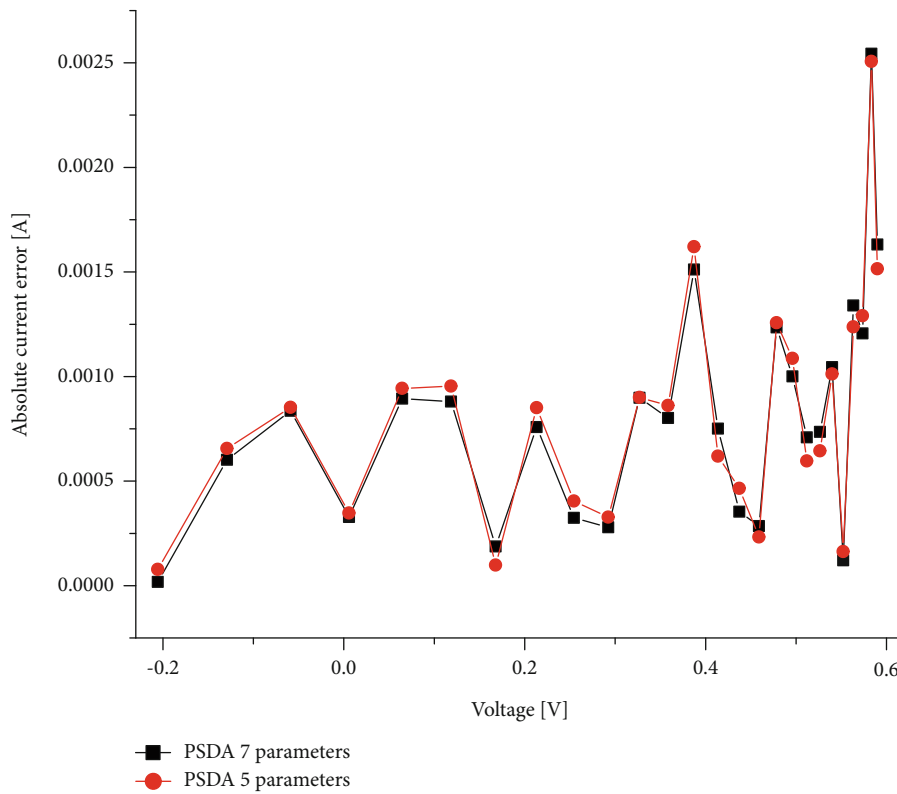
Figure 6: Comparison between the two-diode and one-diode model for STE 4/100 panel.

TABLE 2: The seven parameters of the PWP201 photovoltaic panel.

Algorithm	I_{ph} A	I_{od} μA	I_{or} pA	n_d	n_r	R_s Ω	R_{sh} Ω	RMSE E-03
PSDA	1.032534389	2.511410784	1.14561846	1.317303011	1.31739967	1.234479859	721.503996	2.010645
GCPSO [16]	1.03238233	2.51291639	1.00005742	1.31730465	1.31693992	1.2392884	744.7153985	2.0465
WDOWOAPSO [17]	1.03238234	1.72494775	0.78796322	1.31730435	1.31730449	1.23928868	744.7142646	2.046535
TVACPSO [17]	1.031434	2.6381241	1	1.3209988	2.7777778	1.235632	821.65281	2.0530
ABC-DE [18]	1.0318 E−01	0.32774	2.4305	1.3443	1.3443	1.2062	845.2495	2.4000
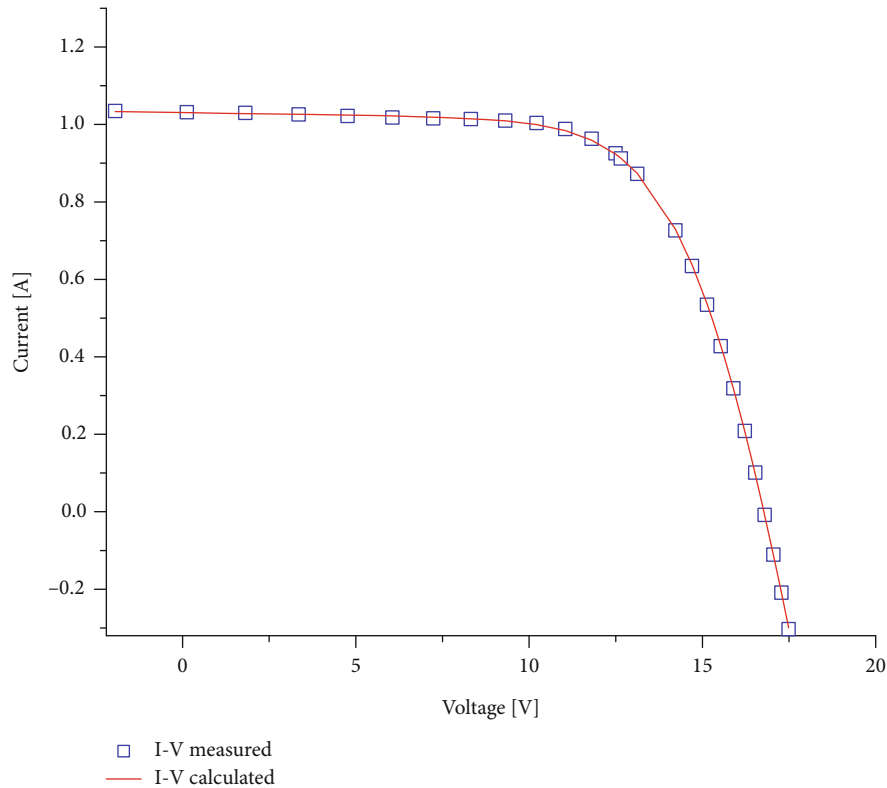
FIGURE 7: The I-V characteristics for PWP201 photovoltaic panel.

A total of s septets are calculated for each interval from Equation (11) ($j = 1, \cdots, s$). From these s^2 values, the best s solutions are selected, and the refining discretization is applied again. A predefined number of refining iterations are performed, and, in the end, the best overall septet is considered the final solution for Equation (3) (having the smallest RMSE error).

2.2.3. PSDA for Double-Diode Solar Cell Model. The idea of the algorithm is as follows. Discretizations are performed on given 7D intervals (see (11) and (12)). At the end of each iteration of the algorithm, "s" good solutions are constructed. In the vicinity of each of these solutions, a new discretization is applied to refine that solution. These discretizations can be performed in parallel on different machines or on different parallel threads on the same machine. The flowchart of the parallel implementation of the algorithm is presented in Figure 2.

Every discretization is executed t times on parallel threads. In the first iteration, there is only one thread, but starting from the second iteration, there are s parallel threads. Before starting the threads, all the values in the vector "finished" are set to the value *false*. Each discretization gets a 7D interval I_j, constructs s solutions, and returns them in the set S_j. When the j-th discretization is finished, the j-th component of the vector "finished" is set to the value *true*. After all the values in the vector "finished" are *true*, it means that all the discretization threads are terminated, and all the sets S_j ($j = 1, \cdots, t$) are constructed.

On an 8-thread I7 processor by performing in parallel the discretization calls the algorithm finishes more than 6 times faster than the nonparallel implementation of the algorithm that computes the discretization on one thread. The above implementation of the algorithm proved to bring the processor utilization across all cores of the computer almost to the maximum (over 98%).
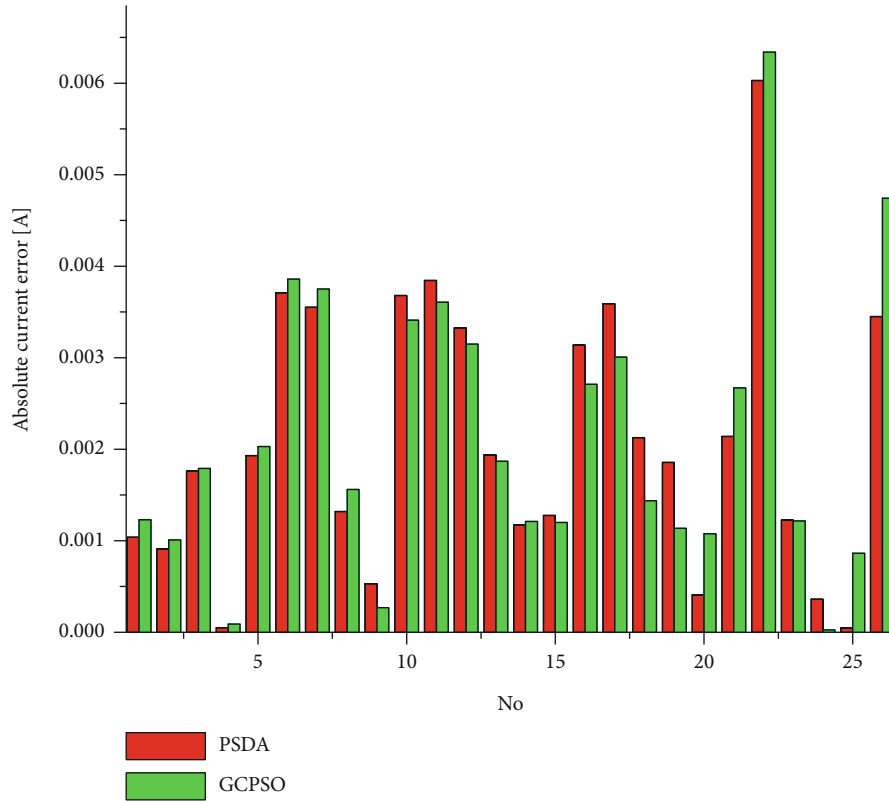
FIGURE 8: Absolute current error comparison for PWP201.

TABLE 3: The seven parameters of the Kyocera KC200GT photovoltaic panel.

Algorithm	I_{ph} A	I_{od} μA	I_{or} pA	n_d	n_r	R_s Ω	R_{sh} Ω	RMSE E-03
PSDA	8.199056758	3.603852195E-4	3.79468615E-5	60.779659859	49.6103408	0.286457209	110.644764	11.98170

3. Results and Discussion

The PSDA algorithm is applied for five datasets—one for RTC photovoltaic cell and the others for four photovoltaic panels: PWP201 [22], Kyocera KC200GT [23], Leibold Solar Module LSM 20 [24], and STE 4/100 [24]. The seven parameters for three out of these four panels are determined for the first time in this paper. The current voltage (I-V) characteristic for RTC is measured at 1000 W/m^2, and the temperature of the photovoltaic cell was 33°C; PWP201 panel is measured at 1000 W/m^2, and the temperature of the photovoltaic panel was 45°C; Kyocera KC200GT panel is measured at 1000 W/m^2 irradiance and 25°C temperature; for LSM 20 panel, the I-V characteristic is measured at 360 W/m^2, and the temperature of the photovoltaic panel was 24°C. The STE 4/100 panel is measured at 900 W/m^2 irradiance and 22°C temperature. The limit intervals for the seven parameters of photovoltaic cell and panel are chosen to be similar with the ones used in the other algorithms [7] for the RTC photovoltaic cell and PWP201 panel. For the Kyocera KC200GT panel, Leibold Solar Module LSM 20, and STE 4/100 panel, the two-diode model is applied for the first time.

3.1. RTC Photovoltaic Cell. The points of RTC photovoltaic cell and the current calculated using PSDA algorithm are shown in Table S1. The seven parameters of the RTC photovoltaic cell and the root mean square error determined by the PSDA algorithm and the values calculated by other algorithms are presented in Table 1.

The I-V pairs of the RTC photovoltaic cell measured and calculated with PSDA algorithm are compared (see Figure 3). A very good matching can be observed, also proven by the lowest value of the root mean square error (see Table 1).

The absolute current error for RTC photovoltaic cell obtained with two algorithms, PSDA and ICSE, is presented in Figure 4. The PSDA absolute current error is lower than for ISCE ones for all measurement points without a uniform distribution. The highest values of the absolute error are around the open circuit voltage cell. The same distribution of the absolute current error is reported in [25].

In the absolute current error for RTC photovoltaic cell calculated with the two-diode model—the seven parameters and with the one-diode model—five parameters are presented in Figures 5 and 6. It can be observed that the absolute current error calculated with the two-diode model is lower
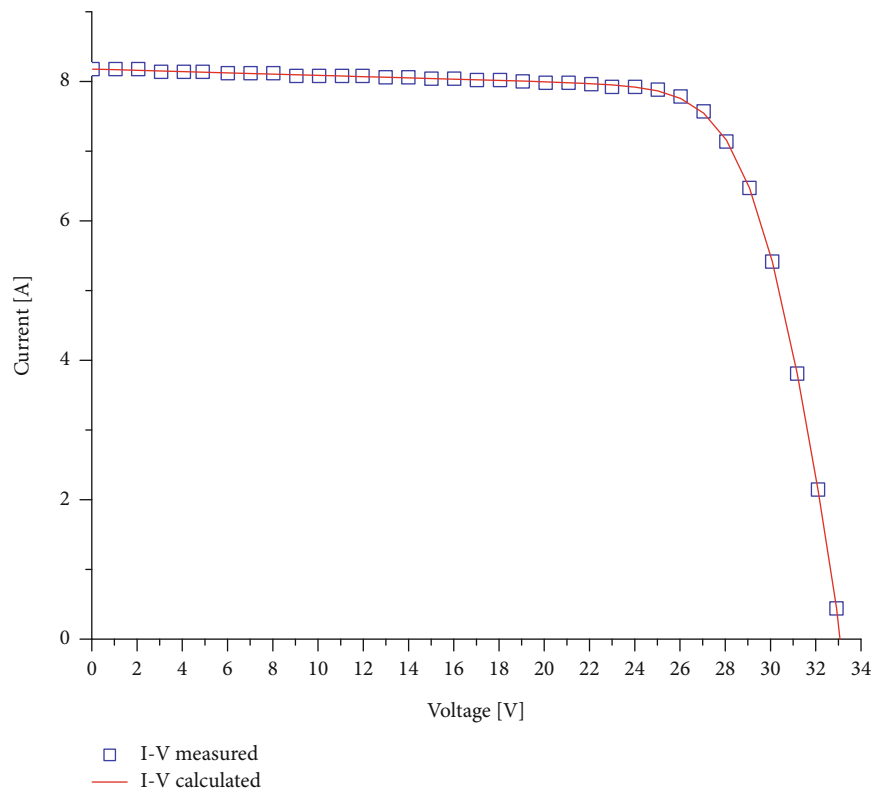
FIGURE 9: The I-V characteristics for Kyocera KC200GT photovoltaic panel.
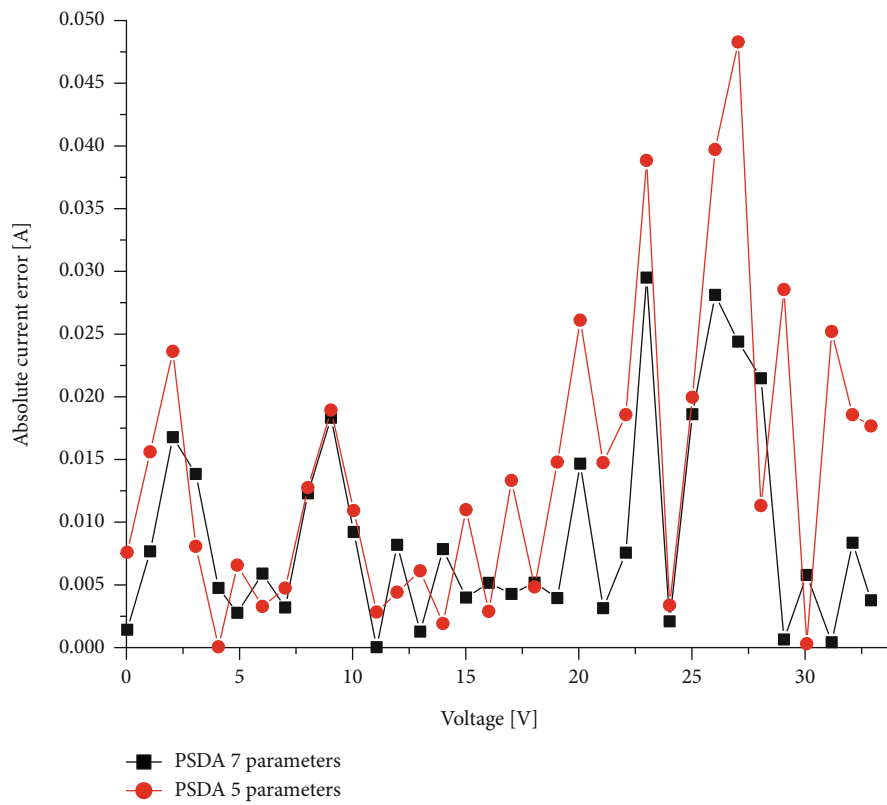

FIGURE 10: Comparison between the two-diodes and one-diode model for the Kyocera KC200GT panel.

TABLE 4: The seven parameters of the LSM 20 photovoltaic panel.

Algorithm	I_{ph} A	I_{od} μA	I_{or} μA	n_d	n_r	R_s Ω	R_{sh} Ω	RMSE E-04
PSDA	0.153932108	2.988457072E-3	3.17136807E-3	26.632811966	26.75109623	6.1728707055	3546.219520	17.5889

□ I-V measured
— I-V calculated
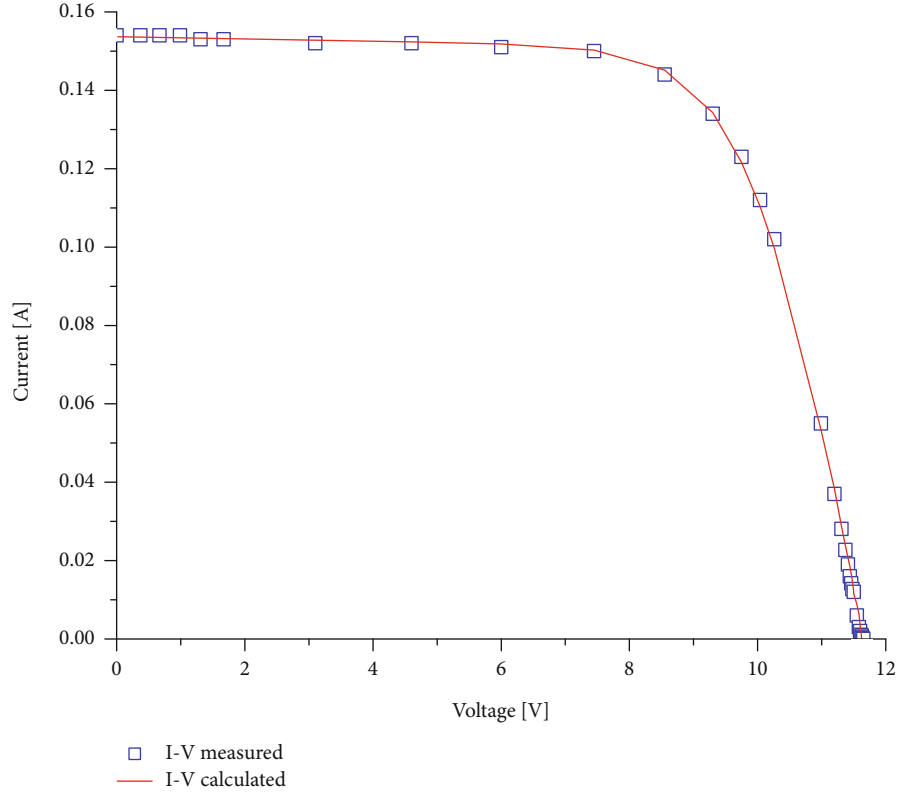
FIGURE 11: The I-V characteristics for LSM 20 photovoltaic panel.

than the ones determined with the one-diode model. This shows that the best solution for the photovoltaic cell parameters is obtained using the two-diode model.

3.2. PWP201 Photovoltaic Panel. The points of PWP201 photovoltaic panel and the current calculated using PSDA algorithm are shown in Table S2. The seven parameters of the PWP201 photovoltaic panel and the root mean square error determined through the PSDA algorithm and the values calculated through other algorithms are presented in Table 2.

The seven parameters of the PWP201 photovoltaic panel, the root mean square error determined through the PSDA algorithm, and the values calculated through other four algorithms are presented in Table 2. PSDA gives similar solutions to other algorithms but with the lowest root mean square error.

By comparing the five algorithms taken into account for PWP201 photovoltaic panel, it can be observed that all seven parameters fluctuate in the function of the applied algorithm. These fluctuations are higher than the ones for RTC photovoltaic cell. The number of I-V pairs is the same for the two photovoltaic devices, but the voltage interval is much higher

for the panel than for the photovoltaic cell, and the calculations are made for fewer points. The I-V characteristics of the PWP201 photovoltaic panel measured and calculated with PSDA algorithm are compared (see Figure 7), and the matching is very good.

The absolute current error for PWP201 photovoltaic panel calculated with two algorithms, PSDA and GCPSO, is presented in Figure 8. The PSDA absolute current error is lower than for GCPSO ones for the majority of the measurements.

The seven parameters for the next three panels are determined for the first time using PSDA. In the literature, there are no other values for the two-diode model to compare with, and so, the solutions are compared with the best ones obtained for the one-diode model.

3.3. Kyocera KC200GT Photovoltaic Panel. The points of Kyocera KC200GT photovoltaic panel and the current calculated using PSDA algorithm are shown in Table S3. The seven parameters of the Kyocera KC200GT photovoltaic panel and the root mean square error determined through the PSDA algorithm are presented in Table 3.
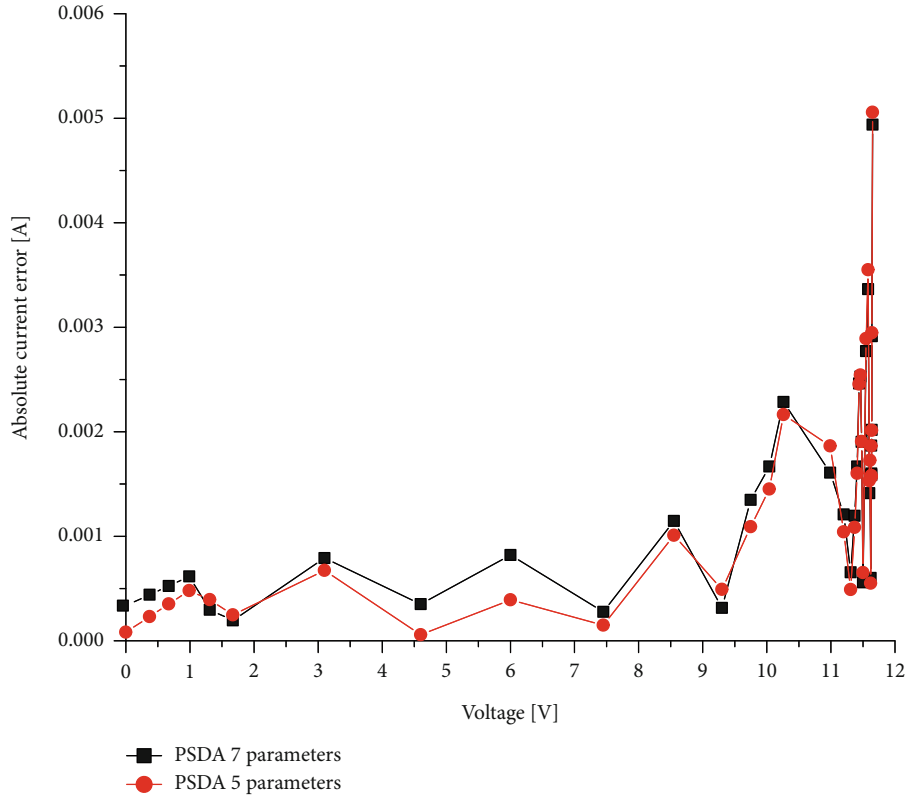
Figure 12: Comparison between the two-diode and one-diode model for LSM 20 panel.

Table 5: The seven parameters of the STE 4/100 photovoltaic panel.

Algorithm	I_{ph} A	I_{od} μA	I_{or} μA	n_d	n_r	R_s Ω	R_{sh} Ω	RMSE E-04
PSDA	0.026434533	7.468752134E-5	4.91018373E-3	4.2799344307	5.199781435	1.1820913872	2109.248002	3.348041

The calculated I-V characteristic of the Kyocera KC200GT photovoltaic panel using PSDA algorithm, which consists 54 multicrystalline silicon photovoltaic cells connected in series, is matching with the I-V points measured [23] (Figure 9).

The comparison between the absolute errors of the current for the one and two-diode models shows that the last model gives for the majority of the I-V points better results (Figure 10). The two-diode model has to be used when the accuracy in calculation of the photovoltaic panel parameters is crucial.

3.4. Leibold Solar Module LSM 20. The points of LSM 20 photovoltaic panel and the current calculated using PSDA algorithm are shown in Table S4. The seven parameters of the LSM 20 photovoltaic panel RMSE determined through the PSDA algorithm are presented in Table 4.

The I-V characteristics of the Leibold Solar Module LSM 20 measured and calculated with PSDA algorithm are compared (see Figure 8). The matching for the measured and calculated points is very good; this is confirmed by the root mean square error which is very small (Table 4) (Figure 11).

Figure 12 illustrates the absolute error for the current, obtained for the LSM 20 photovoltaic panel, using the one- and two-diode models. The RMSE obtained with the two-diode model is smaller than the one obtained with the one-diode model, which is 17.64E-4. This is confirmed by the absolute error obtained through both models. The higher values of the absolute error are splited for the two models used.

3.5. Leybold Solar Module STE 4/100. The points of STE 4/100 photovoltaic panel and the current calculated using PSDA algorithm are shown in Table S5. The seven parameters of the STE 4/100 photovoltaic panel and the root mean square error determined through the PSDA algorithm are presented in Table 5.

The I-V pairs of the Leybold Solar Module STE 4/100 measured and calculated with PSDA algorithm are compared (see Figure 13). A very good matching can be observed, also proven by the lowest value of the root mean square error (see Table 5).

The absolute current error for STE 4/100 photovoltaic panel calculated with the two-diode model and with the
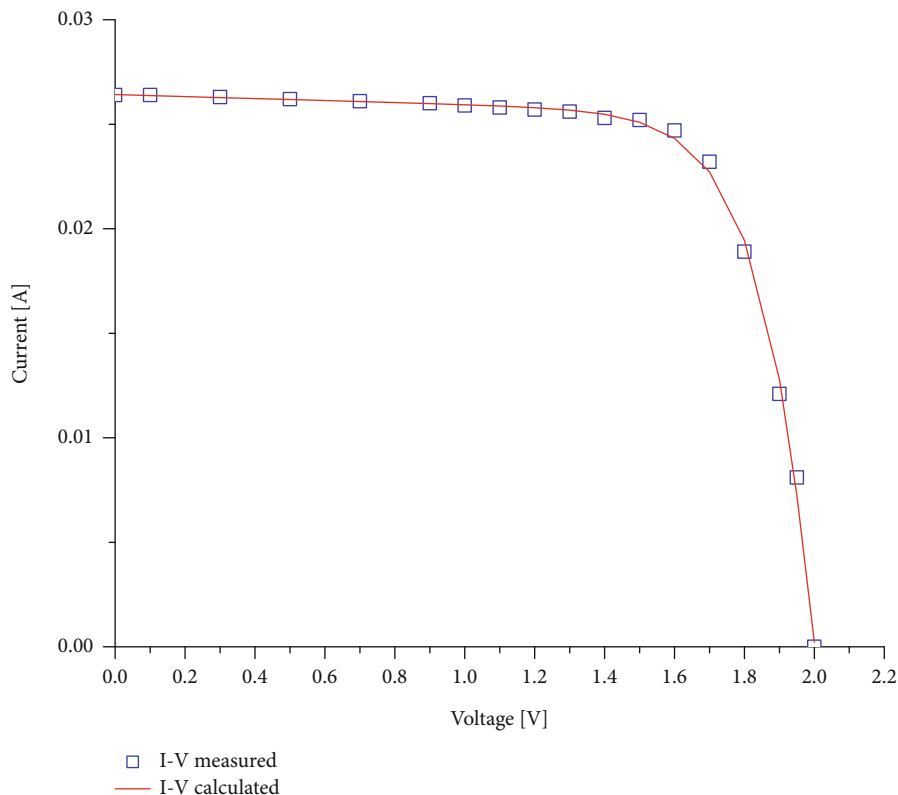
FIGURE 13: The I-V characteristics for STE 4/100 photovoltaic panel.

one-diode model is presented in Figure 5. It can be observed that the absolute current error calculated for the majority points with the two-diode model is lower than the ones determined with the one-diode model. The RMSE obtained with the one-diode model is 4.0853E-4 (Figure 6).

PSDA algorithm was executed with $s = 10$ and with a total of 4 iterations on an 8-thread I7 processor at 1.9 GHz. It ended in 46 seconds. The nonparallel implementation took almost 5 minutes to finish (more than 6 times slower).

4. Conclusions

The estimation of the parameters for the solar cells and panels is very important for designing, simulation, and evaluation of the performance of photovoltaic systems. This problem is currently intensively studied by many researchers. In this paper, the Parallelized Successive Discretization Algorithm is developed and presented to deal with this problem. It is a metaheuristic approach that proved to be a powerful tool for approximating the solution of the implicit transcendental equation problem of finding the seven parameters for the two-diode model. The problem is transformed into a multidimensional optimization problem of minimizing the root mean square error and then solved using multiple and increasing in refining discretizations. The parallel implementation helped to speed up the algorithm since the amount of computations is high and complex. PSDA proves to be fast and reliable that gives very good (the best) estimation of

parameters among the current known algorithms used for the two-diode model. In this paper, the results given by PSDA for one photovoltaic cell and for four panels were given for the two-diode model. The parameters were obtained for the first time for three panels for which only the parameters of one-diode model were determined in the literature.

The sensitivity analysis of the PSDA algorithm is one of the future research directions, and another is to use the PSDA algorithm to extract the parameters of the other photovoltaic cells and panels, for example organic photovoltaic cell using a proper equivalent circuit and the corresponding mathematical model.

Data Availability

Data in supplementary information files.

Conflicts of Interest

The authors declare that there is no conflict of interest regarding the publication of this paper.

Acknowledgments

Supplementary Materials

Table S1: the current calculated using the PSDA algorithm and the relative error, calculated by subtracting the calculated from the measured current values for RTC photovoltaic cell. Table S2: the current calculated using the PSDA algorithm and the relative error for PWP201 photovoltaic panel. Table S3: the current calculated using the PSDA algorithm and the relative error for LSM 20 photovoltaic panel. Table S4: the current calculated using the PSDA algorithm and the relative error for LSM 20 photovoltaic panel. Table S5: the current calculated using the PSDA algorithm and the relative error for LSM 20 photovoltaic panel. *(Supplementary Materials)*

References

[1] D. T. Cotfas, P. A. Cotfas, and S. Kaplanis, "Methods to determine the dc parameters of solar cells: a critical review," *Renewable and Sustainable Energy Reviews*, vol. 28, pp. 588–596, 2013.

[2] D. T. Cotfas, P. A. Cotfas, and S. Kaplanis, "Methods and techniques to determine the dynamic parameters of solar cells: review," *Renewable and Sustainable Energy Reviews*, vol. 61, pp. 213–221, 2016.

[3] D. T. Cotfas, A. M. Deaconu, and P. A. Cotfas, "Application of successive discretization algorithm for determining photovoltaic cells parameters," *Energy Conversion and Management*, vol. 196, pp. 545–556, 2019.

[4] Y. Zhang, P. Lin, Z. Chen, and S. Cheng, "A population classification evolution algorithm for the parameter extraction of solar cell models," *International Journal of Photoenergy*, vol. 2016, Article ID 2174573, 16 pages, 2016.

[5] Q. Niu, H. Zhang, and K. Li, "An improved TLBO with elite strategy for parameters identification of PEM fuel cell and solar cell models," *International Journal of Hydrogen Energy*, vol. 39, no. 8, pp. 3837–3854, 2014.

[6] X. Chen, K. Yu, W. Du, W. Zhao, and G. Liu, "Parameters identification of solar cell models using generalized oppositional teaching learning based optimization," *Energy*, vol. 99, pp. 170–180, 2016.

[7] X. Gao, Y. Cui, J. Hu et al., "Parameter extraction of solar cell models using improved shuffled complex evolution algorithm," *Energy Conversion and Management*, vol. 157, pp. 460–479, 2018.

[8] W. Gong and Z. Cai, "Parameter extraction of solar cell models using repaired adaptive differential evolution," *Solar Energy*, vol. 94, pp. 209–220, 2013.

[9] M. Jamadi, F. Merrikh-Bayat, and M. Bigdeli, "Very accurate parameter estimation of single- and double-diode solar cell models using a modified artificial bee colony algorithm," *International Journal of Energy and Environmental Engineering*, vol. 7, no. 1, pp. 13–25, 2016.

[10] Z. Chen, L. Wu, P. Lin, Y. Wu, and S. Cheng, "Parameters identification of photovoltaic models using hybrid adaptive Nelder-Mead simplex algorithm based on eagle strategy," *Applied Energy*, vol. 182, pp. 47–57, 2016.

[11] L. Guo, Z. Meng, Y. Sun, and L. Wang, "Parameter identification and sensitivity analysis of solar cell models with cat swarm optimization algorithm," *Energy Conversion and Management*, vol. 108, pp. 520–528, 2016.

[12] A. Askarzadeh and A. Rezazadeh, "Extraction of maximum power point in solar cells using bird mating optimizer-based parameters identification approach," *Solar Energy*, vol. 90, pp. 123–133, 2013.

[13] D. Oliva, M. Abd El Aziz, and A. Ella Hassanien, "Parameter estimation of photovoltaic cells using an improved chaotic whale optimization algorithm," *Applied Energy*, vol. 200, pp. 141–154, 2017.

[14] A. Askarzadeh and A. Rezazadeh, "Parameter identification for solar cell models using harmony search-based algorithms," *Solar Energy*, vol. 86, no. 11, pp. 3241–3249, 2012.

[15] K. M. El-Naggar, M. R. AlRashidi, M. F. AlHajri, and A. K. Al-Othman, "Simulated annealing algorithm for photovoltaic parameters identification," *Solar Energy*, vol. 86, no. 1, pp. 266–274, 2012.

[16] H. G. G. Nunes, J. A. N. Pombo, S. J. P. S. Mariano, M. R. A. Calado, and J. A. M. Felippe de Souza, "A new high performance method for determining the parameters of PV cells and modules based on guaranteed convergence particle swarm optimization," *Applied Energy*, vol. 211, pp. 774–791, 2018.

[17] H. G. G. Nunes, J. A. N. Pombo, P. M. R. Bento, S. J. P. S. Mariano, and M. R. A. Calado, "Collaborative swarm intelligence to estimate PV parameters," *Energy Conversion and Management*, vol. 185, pp. 866–890, 2019.

[18] O. Hachana, K. E. Hemsas, G. M. Tina, and C. Ventura, "Comparison of different metaheuristic algorithms for parameter identification of photovoltaic cell/module," *Journal of Renewable and Sustainable Energy*, vol. 5, no. 5, article 053122, 2013.

[19] S. M. Ebrahimi, E. Salahshour, M. Malekzadeh, and F. Gordillo, "Parameters identification of PV solar cells and modules using flexible particle swarm optimization algorithm," *Energy*, vol. 179, pp. 358–372, 2019.

[20] S. Kotsiantis and D. Kanellopoulos, "Discretization techniques: a recent survey," *GESTS International Transactions on Computer Science and Engineering*, vol. 32, pp. 47–58, 2006.

[21] S. Garcia, J. Luengo, J. A. Saez, V. Lopez, and F. Herrera, "A survey of discretization techniques: taxonomy and empirical analysis in supervised learning," *IEEE Transactions on Knowledge and Data Engineering*, vol. 25, no. 4, pp. 734–750, 2013.

[22] T. Easwarakhanthan, J. Bottin, I. Bouhouch, and C. Boutrit, "Nonlinear minimization algorithm for determining the solar cell parameters with microcomputers," *International Journal of Solar Energy*, vol. 4, no. 1, pp. 1–12, 1986.

[23] J. Ma, *Optimization approaches for parameter estimation and maximum power point tracking (MPPT) of photovoltaic systems, [Ph.D. thesis]*, University of Liverpool Repository, Liverpool, 2014.

[24] F. F. Muhammad, A. W. Karim Sangawi, S. Hashim, S. K. Ghoshal, I. K. Abdullah, and S. S. Hameed, "Simple and efficient estimation of photovoltaic cells and modules parameters using approximation and correction technique," *PLoS One*, vol. 14, no. 5, article e0216201, 2019.

[25] H. Chen, S. Jiao, M. Wang, A. A. Heidari, and X. Zhao, "Parameters identification of photovoltaic cells and modules using diversification-enriched Harris hawks optimization with chaotic drifts," *Journal of Cleaner Production*, vol. 244, article 118778, 2020.

Research Article

Crystalline Silicon PERC Solar Cell with Ozonized AlOx Passivation Layer on the Rear Side

Pang-Kai Liu, Yu-Lun Cheng, and Likarn Wang [ID]

Institute of Photonics Technologies, National Tsing Hua University, Hsinchu, Taiwan

Correspondence should be addressed to Likarn Wang; lkwang@ee.nthu.edu.tw

We present a method of ozonation to form the rear-side passivation layers of crystalline silicon PERC cells. In the method, a thin aluminum film was deposited on the back surface of a silicon wafer and then was oxidized into an aluminum oxide layer by gaseous ozone. Lifetimes of the wafers with such passivation layers proved to be increased with respect to those untreated, and the resultant PERC cells showed a performance improvement compared with standard cells with full back surface fields.

1. Introduction

A basic cell structure of crystalline silicon PERC (passivated emitter and rear cell) cells commonly fabricated by industry is shown in Figure 1 [1], where silver electrodes are screen printed on the front surface of a p-type textured wafer with an antireflection coating (ARC) and a diffused N+ layer, while local contacts are formed by fired aluminum paste at the laser-ablated parts of the back surface with a stack of AlOx/SiNx. A local BSF (back surface field) is formed on the rear contact to facilitate the collection of holes, and the thin AlOx (arising from Al_2O_3) layer contributing field-effect passivation will eject electrons and thus reduce recombination of electrons and holes near the rear side of the wafer [2].

The Al_2O_3 layer with an appropriate thickness can be deposited on a p-type silicon wafer by a PECVD [3, 4] or an ALD [5, 6] technique. The resultant passivation layer AlOx is formed at the interface of Si/Al_2O_3 after the wafer is annealed at a proper temperature and produces negative charges with a density that is several times as high as $10^{12}\,cm^{-2}$. In between silicon and AlOx, there exists a layer of SiOx in a tetrahedral geometry [7, 8]. The AlOx near the SiOx also has a tetrahedral geometry, rendering the insufficiency of aluminum atoms and henceforth negative charges. Nowadays, industrial PERC cells with such passivation layers have achieved a conversion efficiency of ~21% or even higher

[9, 10]. Deposition of an Al_2O_3 layer by either PECVD or ALD, however, is not a cost-effective way because the precursor trimethylaluminum and a vacuum-processing facility are both required. Many different methods for the formation of Al_2O_3 layers for the purpose of passivation have been developed without using vacuum-chamber-equipped facilities.

A good passivation layer was obtained by using a technique of reactive sputtering without using trimethylaluminum, resulting in PERC cells that showed a significant improvement in efficiency compared with standard full BSF cells [11]. A printable aluminum oxide paste was demonstrated to support an efficiency of 20.1%, which could be easily integrated into an existing production line and cause a reduction of additional cost for equipment [12]. The researchers of [13] reported a high-level passivation with an Al_2O_3 layer synthesized on a p-type crystalline silicon wafer by a sol-gel method. The inventors of [14] proposed spraying methanol solution containing aluminum elements (or specifically, containing aluminum acetylacetonate) on the surface of a silicon wafer for forming a passivation layer. This idea could result in a tremendous reduction in manufacturing cost, however, leaving unsolved a problem of uneven thicknesses of the passivation layers from sample to sample. In this study, we present a different method for forming an Al_2O_3 layer for the back surface passivation of a PERC cell. Although vacuum-supported equipment is employed in the method, Al_2O_3 layers with a uniform thickness can be
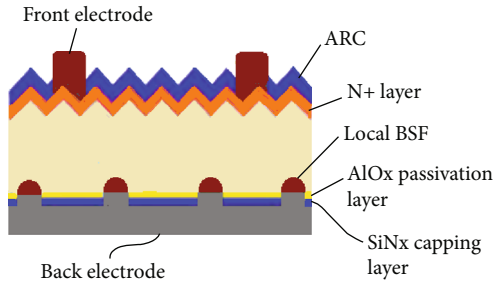
Figure 1: Structure of a crystalline silicon PERC cell commonly fabricated by industry.

formed without trimethylaluminum used. In this new method, a thin aluminum film was first deposited on the back surface of a phosphorus-diffused silicon wafer and then oxidized into an aluminum oxide layer by gaseous ozone. Such an aluminum oxide layer proved to produce a good level of passivation after annealed at a proper temperature. Section 2 reveals the formation of such a passivation layer and briefs the fabrication process of PERC cells in this study. Experimental results for minority carrier lifetime and cell performance measurements are presented in Section 3, followed by a conclusion section.

2. Experiments

2.1. Al_2O_3 Layer Formed by Ozonation Method. Pseudosquare- (100-) oriented $200\,\mu m$ thick diamond-wire-sawn single-crystalline silicon wafers in the dimensions of $156 \times 156\,mm^2$ were cut into smaller pieces with a size of $5.2 \times 5.2\,cm^2$. For lifetime measurement, these wafers were treated to form an Al_2O_3 layer on, respectively, their front and back surfaces. To form the Al_2O_3 layer, we first used an e-gun evaporator to deposit a 3 nm thick aluminum film on the two surfaces of the wafer. The panel setting for this film thickness was 3 nm, which, however, was believed to be smaller than the true value of thickness, as we will see later. The as-deposited wafers were then put in a beaker with a piece of saran wrap covering its top for hermetic seal while allowing an ozone gas supplier to constantly feed the beaker with gaseous ozone. After a period of time, the aluminum films were transformed into Al_2O_3 films, followed then by an annealing process. Such a treatment for Al_2O_3 formation was also applied to commercial blue wafers as well as textured wafers, the latter of which had a surface morphology of inverted pyramid-like structure (see Figure 2) that was formed by using our proprietary method. Here, the commercial blue wafers refer to the wafers processed in an industrial production line up to the step of deposition of PECVD ARC layers. Al_2O_3 films were formed only on the back surfaces of these wafers, and so we could observe the improvement in lifetime with respect to untreated commercial blue wafers.

Figure 3 shows the stack of $Al_2O_3/SiO_2/Si$ for a sample that was originally coated with an aluminum film and was subsequently ozone-treated and annealed at 600°C for 90 seconds. It can be seen that the thicknesses of Al_2O_3 and SiO_2 read, respectively, 7.64 nm and 3.15 nm. In the following,

we will show that this annealing condition gave rise to the best passivation effect. After oxidized, a 3 nm thick aluminum layer was supposed to become about 5 nm thick. The Al_2O_3 thickness obtained was not consistent with the expected for the possible reason of unreliable aluminum thickness at only several nanometers achieved by using e-gun evaporation.

A depth profile showing atomic compositions obtained by X-ray photoelectron spectroscopy is given in Figure 4 for a sample with the stack of $Al_2O_3/SiO_2/Si$ on a silicon substrate after the ozonation method was applied on the aluminum metal film, and the sample was annealed at 600°C for 90 seconds. Obviously, Al_2O_3 was formed at etch time less than ~100 seconds. After the etch time of 100 seconds, AlOx with $x > 1.5$ can be seen. For example, at the etch times between 125 and 150 seconds, x is about 1.7. However, we are aware that the depth profile does not appear to be as steep as it should be to show the respective layers on the silicon substrate. This is because the atomic composition at each etch time is taken as an average quantity over the atomic compositions obtained at neighboring etch times for the XPS instrument we used here. On the other hand, EDS analysis (Figure 5) reveals the compositions of Si, Al, O, and Pt (platinum) atoms, where Pt atoms were detected because the sample was covered with platinum metal for measurement. The oxygen/Si ratio appeared to be about $2:1$ at the positions of 40-43 nm, indicating a layer of SiO_2 there. For the region of 43-45 nm, the oxide was much like SiO_4, indicating a tetrahedral geometry. Then away from the SiO_4 layer, i.e., from the position of ~45 nm, the number of Al atoms increased and supported the existence of AlOx, where $5 > x > 1.6$, with Al vacancy at the positions of 44-46 nm, and approach Al_2O_3 at farther positions, i.e., the positions of 46-53 nm. After the point of 53 nm, a rapidly growing number of Pt atoms were detected. The structural transition from SiOx to Al_2O_3 over the interface region was consistent with the remark in [7].

2.2. PERC Cell Fabrication. Here, we used diamond-wiresawn single-crystalline silicon wafers for the study of PERC cells. These wafers were textured to have an inverted-pyramid-like structure on two sides and were then phosphorus diffused to form an n layer on the front side. After an Al_2O_3 layer was formed on the rear side of each diffused wafer with the size of $5.2 \times 5.2\,cm^2$, followed by annealing at 600°C for 90 seconds. Such an annealing condition was found to achieve the best minority carrier lifetime for bare wafers that were coated with Al_2O_3 on both sides and for diffused wafers coated with SiNx ARC on the front side and Al_2O_3 on the back side. Then, a 100 nm thick SiNx layer was deposited on the Al_2O_3 layer by PECVD, resulting in a stack of $Al_2O_3/SiNx$ on the rear side. A photolithographic process was subsequently employed to form a pattern of line-shaped openings on the rear side. Then, a SiNx layer with a thickness of 100 nm was deposited by PECVD to form an ARC layer on the front side. Aluminum paste and silver paste were subsequently screen printed on the rear side and the front side, respectively, followed by cofiring in a conveyor belt furnace.
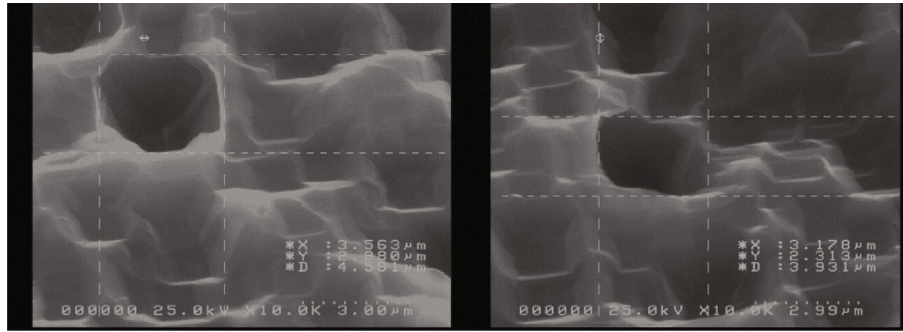
FIGURE 2: Surface morphologies measured at two positions of the wafer used for PERC cell fabrication in the study.
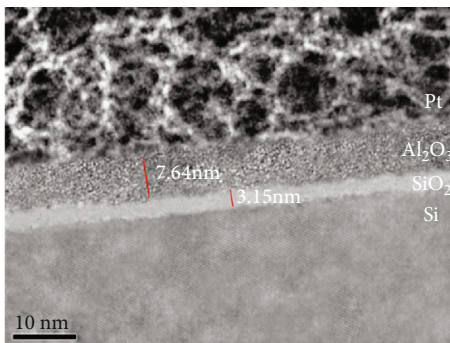

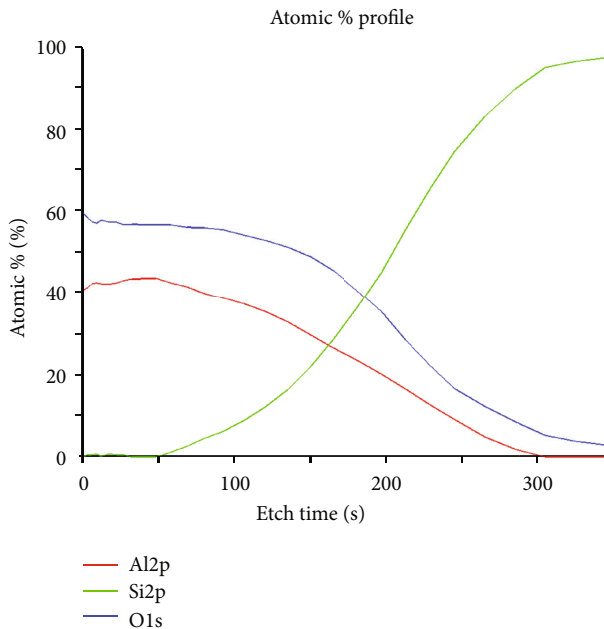FIGURE 3: TEM picture of $Al_2O_3/SiO_2/Si$ stack after the aluminum oxide was annealed at 600°C for 90 seconds.

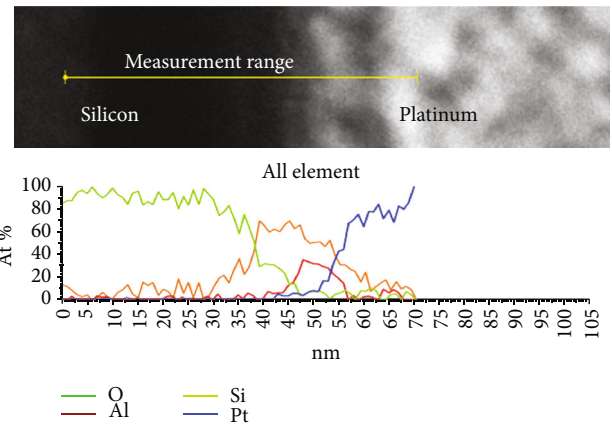FIGURE 4: XPS measurement of elements near the surface of an annealed sample with ozone-treated Al_2O_3.

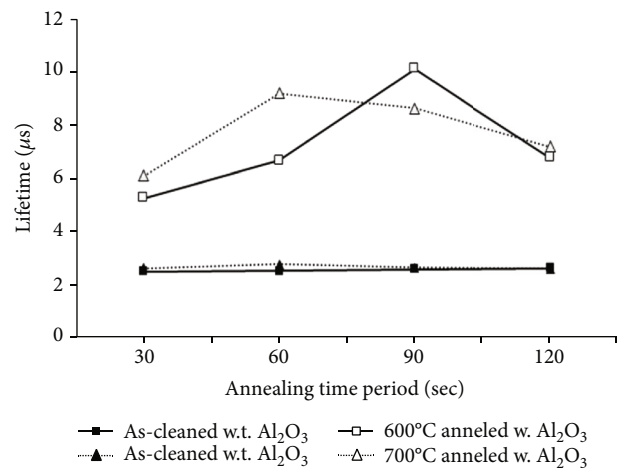FIGURE 5: EDS analysis for a sample with the stack of $Al_2O_3/SiO_2/Si$ after annealed at 600°C for 90 seconds.

FIGURE 6: Lifetimes of bare wafers achieved at 600°C and 700°C for various annealing time periods. A maximum lifetime of 10.15 μs occurred at 600°C for 90 seconds.

3. Experimental Results

3.1. Lifetime Measurement. First, we measured the lifetimes of bare wafers without Al_2O_3 formed yet on both the front and the rear sides. Figure 6 shows the lifetime measurement results by using the quasi-steady-state photoconductance technique with Sinton WCT-120, at the minority carrier density 10^{15} cm^{-3}. The bare wafers in the dimensions of 5.2×5.2 cm^2 were cleaned by supersonic acetone and were then SC-1 cleaned, followed by a saw damage removal process with a mixture of $CH_3COOH/HF/HNO_3$. Lifetimes of these wafers
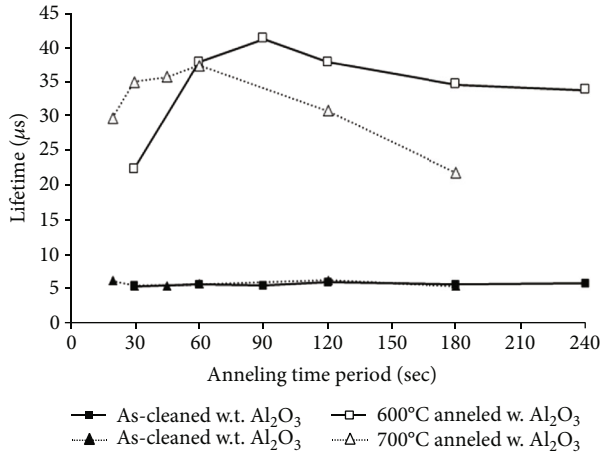
FIGURE 7: Lifetimes of commercial blue wafers achieved at 600°C and 700°C for various annealing time periods. A maximum lifetime of 41.15 μs occurred at 600°C for 90 seconds.

were measured and then were measured again after Al_2O_3 layers were formed by the ozonation method on both the front and the rear sides. Figure 6 shows the lifetimes for these ozone-treated bare wafers annealed at 600°C (blank squares) and 700°C (blank triangles), respectively, for various annealing time periods. The filled squares and filled triangles in the figure represent the lifetimes of the as-cleaned wafers that were not annealed and were measured here for reference only. The as-annealed wafers with Al_2O_3 layers marked by the blank squares and blank triangles should be compared with the as-cleaned wafers marked by the filled squares and filled triangles, respectively. It can be seen that the lifetime of the ozone-treated wafer annealed at the temperature of 600°C for an annealing time period of 90 seconds could improve by 3.9 times (from 2.6 μs to 10.15 μs) with respect to that of the corresponding as-cleaned wafer. On the other hand, the lifetime improvement for 700°C annealed ozone-treated wafer was 3.3 times at maximum (for an annealing time period of 60 seconds) with respect to that of the corresponding as-cleaned wafer. We have also measured the lifetimes of commercial blue wafers with and without an Al_2O_3 layer on the rear side. Figure 7 shows the lifetimes measured at 600°C and 700°C, respectively, for various annealing time periods. Again, we can see that the time period of 90 seconds was the best annealing time period for 600°C annealing, while the time period of 60 seconds was the best annealing time period for 700°C annealing, and that 600°C annealing supported a better lifetime than 700°C annealing. Likewise, the as-annealed wafers with Al_2O_3 layers are marked by the blank squares (for 600°C annealing) and blank triangles (for 700°C annealing), while the commercial blue wafers without Al_2O_3 layers (denoted by as-cleaned blue wafers) are marked by the filled squares and filled triangles, respectively. These as-cleaned blue wafers were not annealed and are shown only for comparison with the as-annealed blue wafers. The as-annealed blue wafers with Al_2O_3 layers marked by the blank squares and blank triangles should be compared with the as-cleaned blue wafers marked by the filled squares and filled triangles, respectively.
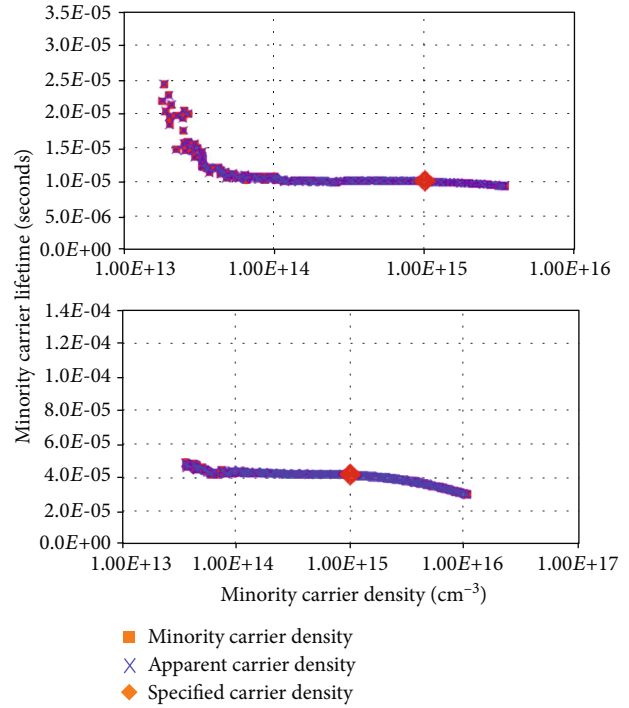

FIGURE 8: Minority carrier lifetime versus minority carrier density for the ozone-treated bare wafer (top) and the ozone-treated commercial blue wafer (bottom) both annealed at 600°C for 90 seconds. The specified carrier density is 10^{15} cm^{-3}.

Also, we can be aware that the lifetime was improved by 7.3 times (from 5.62 μs to 41.15 μs) at the best annealing condition with respect to the case of no passivation layer on the rear side. Therefore, we adopted 600°C/90 seconds for the annealing condition for the PERC cell fabrication in this study. The density of the negative charges induced by the annealed Al_2O_3 layer was measured by a CV measurement to be -2.30×10^{12} cm^{-2} in the best annealing condition. Figure 8 shows the lifetime versus minority carrier density for the ozone-treated bare wafer (top) and the ozone-treated commercial blue wafer (bottom) both annealed at 600°C for 90 seconds.

3.2. Cell Fabrication. The wafers used for PERC cell fabrication in the study were textured to have caves with inward inclined faces on two sides of the wafers. The sizes of these caves ranged from 1.5 to 3.5 μm, as can be seen from Figure 2. We also measured the lifetimes of these textured wafers with two-side ozone-treated Al_2O_3 layers. Figure 9 shows the lifetimes of the textured wafers with two-side Al_2O_3 layers formed on them and annealed at 600°C for various annealing time periods. The as-cleaned wafers without Al_2O_3 layers were of a textured type but not annealed, and their lifetimes are shown just for comparison with the lifetimes of the textured wafers with two-side ozone-treated Al_2O_3 layers. It can be seen that the best annealing condition for this type of wafers was the same as for standard bare wafers shown previously in Figure 6. Here, the highest lifetime of 10.1 μs occurred in the case of the 90-second annealing time period, which was 4.1 times higher compared to the
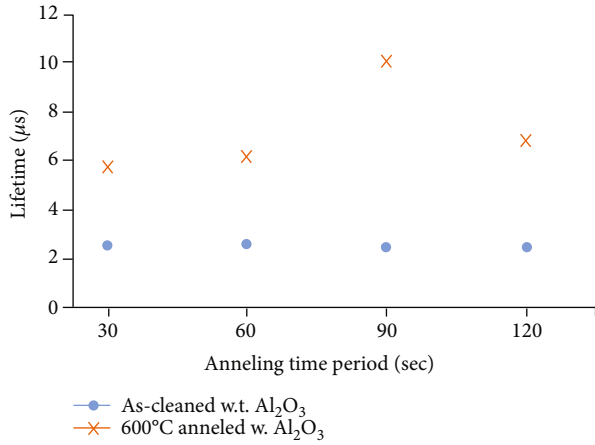
FIGURE 9: Lifetimes of textured wafers annealed at 600°C for various annealing time periods.
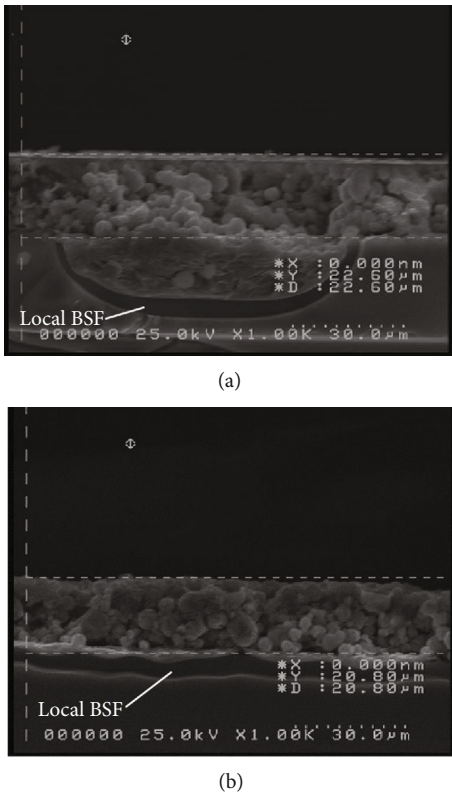

(a)

(b)

FIGURE 10: Local BSF for a PERC cell (a) and a full BSF for an Al-BSF cell (b).

case when the wafer was not coated with two-side Al$_2$O$_3$ layers.

Then, the textured wafers were used for the fabrication of solar cells. After phosphorus diffused with phosphorus pentoxide wafers used in a tube-based furnace at 870°C, these wafers exhibited a sheet resistance of 80 to 85 $\Omega/\square$. Then, the rear sides of the diffused wafers were dipped into a dilute NaOH solution to polish the back surface while the PSG remained on the front surface. The PSG was removed after-

TABLE 1: Electric parameters and conversion efficiencies measured for Al-BSF cells (A1 and A2) and PERC cells (B1, B2, and B3).

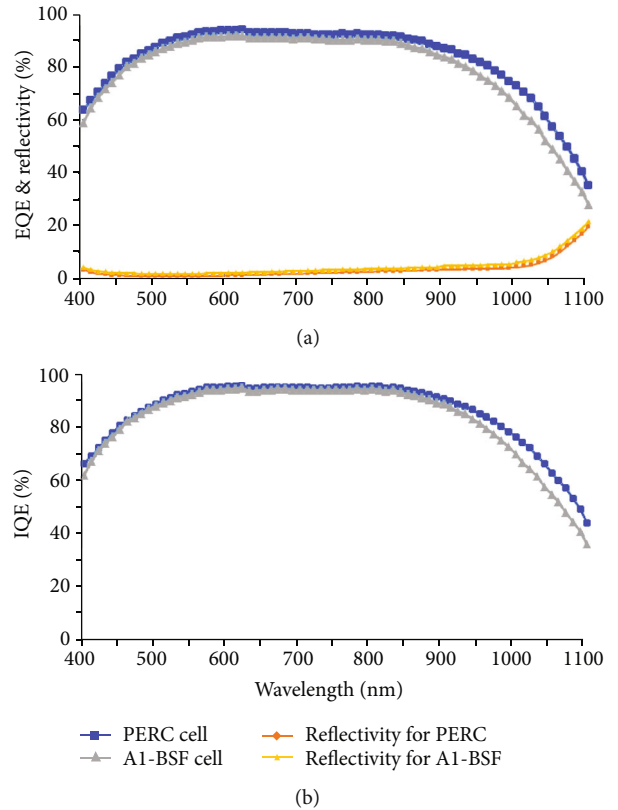| Cell	Jsc (mA/cm^2)	Voc (mV)	F.F. (%)	η (%)
A1	37.32	570	76.7	16.32
A2	37.37	570	76.4	16.27
B1	37.89	590	75.7	16.92
B2	38.14	590	74.7	16.81
B3	37.5	600	75.1	16.73

(a)

(b)

FIGURE 11: EQE, reflectivity (a), and IQE (b) of the two best cells in this study.

ward by dipping the wafers into a solution of dilute HF. An Al$_2$O$_3$ layer was then coated on the rear side of each wafer using the aforementioned ozonation method, followed by deposition of a PECVD SiNx capping layer of 100 nm thickness on the Al$_2$O$_3$ layer. Then, a photolithographic process applied to form a line-shaped pattern of openings by using a H$_3$PO$_4$ solution to etch away a part of the SiNx capping layer at 100°C, followed by etching with a HF/HNO$_3$ solution to form line trenches with a depth of ~30 μm and a width of ~50 μm. Note that the center-to-center spacing between two adjacent line trenches was 1200 μm, and therefore, the coverage for the capping layer was ~96%. At this step, most of the SiNx layer remained and was covered with a photoresist. After the photoresist was removed by acetone, a PECVD SiNx ARC layer of 100 nm thickness was deposited on the front side. Then, the aluminum paste was screen printed on the full surface of the rear side, and the silver paste in a grid

pattern with only one busbar at the center was screen printed on the front side. The widths of the busbar and the fingers were 2 mm and 100 μm, respectively, with the finger spacing being 1.9 mm (edge to edge). After cofired through a conveyer belt furnace, the cells were cut into pieces with the dimensions of $2 \times 2\, cm^2$.

To fabricate conventional cells having the aluminum paste screen-printed on the rear side without a passivation layer (denoted by Al-BSF cells), we followed the previous cell fabrication process except that there were no Al_2O_3/SiNx stack and photolithography required. The resultant back surface fields (BSFs) for PERC cells and Al-BSF cells are, respectively, shown in (a) and (b) of Figure 10.

The cell performances for PERC cells and Al-BSF cells are compared in Table 1. Two cells, A1 and A2, were of Al-BSF type, and three cells, B1~B3, were of PERC type. It can be seen that PERC cells had a better cell efficiency than Al-BSF cells, owing to the fact that a larger short-circuit current and a higher open-circuit voltage could be reached for PERC cells although with a lower fill factor (F.F.). The best PERC cell here had a conversion efficiency of 16.92, which was 0.6% (absolute) higher with respect to the best Al-BSF cell. The external and internal quantum efficiencies (EQE and IQE) of the two best cells are shown in Figure 11, where the front-surface reflectivities for both wafers are also shown. It can be seen that both EQE and IQE are higher for the PERC cell than those for the Al-BSF cell, especially at long wavelengths (e.g., longer than 950 nm).

4. Conclusion

We have presented an ozonation method for forming a passivation layer, i.e., an Al_2O_3 layer on the rear side of a crystalline silicon solar cell. In this method, an aluminum metal film was first deposited and then was oxidized into an Al_2O_3 layer by ozone gas. Lifetimes of the single-crystalline silicon wafers with an ozone-treated Al_2O_3 layer showed ~4 times improvement for bare wafers and 7.3 times improvement for commercial blue wafers. The PERC cells fabricated using textured wafers with such passivation layers showed better conversion efficiency than Al-BSF cells. The best PERC cell showed an efficiency improvement by 0.6% absolute with respect to the best Al-BSF cell in this study.

Data Availability

The raw/processed data for these findings cannot be shared at this time as the data also form part of an ongoing study.

Conflicts of Interest

The authors declare that there is no conflict of interest regarding the publication of this paper.

References

[1] G. Sebastian, D. Thorsten, and B. Rolf, "Evaluation of series resistance losses in screen-printed solar cells with local rear contacts," *IEEE Journal of Photovoltaics*, vol. 1, no. 1, pp. 37–42, 2011.

[2] V. Naumann, M. Otto, R. B. Wehrspohn, and C. Hagendorf, "Chemical and structural study of electrically passivating Al2O3/Si interfaces prepared by atomic layer deposition," *Journal of Vacuum Science & Technology A: Vacuum, Surfaces, and Films*, vol. 30, no. 4, article 04D106, 2012.

[3] P. Saint-Cast, M. Hofmann, S. Kühnhold et al., "A Review of PECVD aluminium oxide for surface passivation," in *27th European Photovoltaic Solar Energy Conference and Exhibition*, pp. 1797–1801, Frankfurt, Germany, 2012.

[4] J. A. Töfflinger, A. Laades, C. Leendertz et al., "PECVD-AlOx/-SiNx passivation stacks on silicon: effective charge dynamics and interface defect state spectroscopy," *Energy Procedia*, vol. 55, pp. 845–854, 2014.

[5] D. Pysch, C. Schmitt, B. Latzel et al., "Implementation of an ALD-Al2O3 PERC-technology into a multi- and monocrystalline industrial pilot production," in *Proceedings of the 29th European Photovoltaic Solar Energy Conference*, pp. 612–616, Amsterdam, Netherlands, 2014.

[6] J. Sheng, J.-H. Lee, W.-H. Choi, T. H. Hong, M. J. Kim, and J.-S. Park, "Review Article: Atomic layer deposition for oxide semiconductor thin film transistors: advances in research and development," *Journal of Vacuum Science & Technology A*, vol. 36, no. 6, article 060801, 2018.

[7] K. Kimoto, Y. Matsui, T. Nabatame et al., "Coordination and interface analysis of atomic-layer-deposition Al2O3 on Si (001) using energy-loss near-edge structures," *Applied physics letters*, vol. 83, no. 21, pp. 4306–4308, 2003.

[8] F. Werner and J. Schmidt, "Manipulating the negative fixed charge density at the c-Si/Al2O3interface," *Applied physics letters*, vol. 104, no. 9, article 091604, 2014.

[9] J. Schmidt, F. Werner, B. Veith et al., "Industrially relevant Al2O3 deposition techniques for the surface passivation of Si solar cells," in *5th World Conference on Photovoltaic Energy Conversion*, Valencia, Spain, 2010.

[10] F. Ye, W. Deng, W. Guo et al., "22.13% efficient industrial p-type mono PERC solar cell," in *IEEE 43rd Photovoltaic Specialists Conference (PVSC)*, Portland, USA, 2016.

[11] G. Krugel, W. Wolke, F. Wagner, J. Rentsch, and R. Preu, "Sputtered aluminum oxide for rear side passivation of p-type silicon solar cells," in *27th European PV Solar Energy Conference and Exhibition*, Frankfurt, Germany, 2012.

[12] Y.-S. Lin, J.-Y. Hung, T.-C. Chen et al., "Effect of post deposition annealing of printed AlOx film on PERC solar cells," in *IEEE 40th Photovoltaic Specialists Conference*, Colorado, U.S.A., 2014.

[13] H.-Q. Xiao, C.-L. Zhou, X.-N. Cao et al., "Excellent passivation of p-type Si surface by sol-gel Al_2O_3 films," *Chinese Physics Letters*, vol. 26, no. 8, article 088102, 2009.

[14] T. Hiramatsu, H. Orita, T. Shirahata, T. Kawaharamura, and S. Fujita, *Solar cell manufacturing method*, 2016, US patent, US 2016/0204301 A1.